NATIONAL TECHNICAL UNIVERSITY OF ATHENS
SCHOOL OF NAVAL ARCHITECTURE AND MARINE ENGINEERING
DIVISION OF SHIP AND MARINE HYDRODYNAMICS

Hydro-elastic analysis of flapping foils by a coupled BEM-FEM with application to marine energy extraction devices

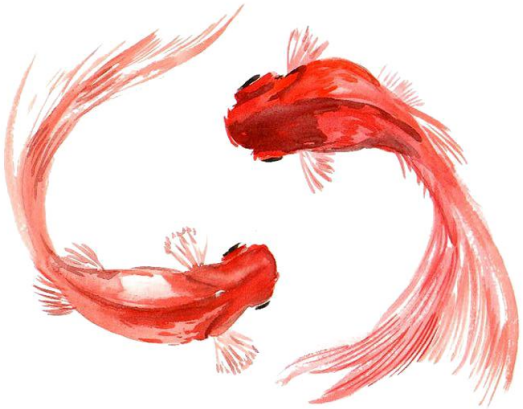

Diploma Thesis

March 2019, Athens

Author: Dimitra Anevlavi
Supervisor: K.A. Belibassakis, Professor, NTUA
Committee: G. K. Politis, Professor, NTUA
G. Triantafyllou, Professor, NTUA

Dedicated to my grandfather

Table of Contents

ACKNOWLEDGEMENTS **7**

ABSTRACT **9**

CHAPTER 1 - INTRODUCTION **11**

1.1 Applications Of Biomimetic Systems 11
1.2 Flexible Flapping Foil Propulsion Systems 14
1.2.1 Experimental Studies 14
1.2.2 Numerical Modelling based on Potential Theory 18
1.2.3 Computational Fluid Dynamics (CFD) Simulations 20
1.3 Flexible Biomimetic Wave and Tidal Energy Extraction Devices 22

CHAPTER 2 - HYDRODYNAMICS OF FLAPPING FOILS WITH PRESCRIBED DEFORMATIONS **23**

2.1 Brief Literature Review on Boundary Element Methods 24
2.2 Definition of the Unsteady Lifting Flow Problem 25
2.2.1 Pressure-type Kutta Condition 29
2.2.2 Representation Theorem - Boundary Integral Equation (BIE) 31
2.3 Discretization Scheme for BEM 33
2.3.1 Solution of the Hydrodynamic Problem 36
2.4 Numerical Results 42
2.4.1 Flapping-Foil Propulsion Parameters 42
2.4.2 Calculation of Pressure and Forces 44
2.4.3 Numerical Study 47
2.4.4 Validation 49

CHAPTER 3 - STRUCTURAL ANALYSIS OF THIN PLATE IN VACUO **51**

3.1 Brief introduction on Finite Element Method 52
3.2 Cylindrical Bending of Thin Elastic Plates 53
3.2.1 Weak Formulation of the Initial-Boundary Value Problem (IBVP) 59
3.3 Discretization Scheme for hp-FEM 61
3.3.1 Addition of Proportional Damping Terms 65
3.3.2 Time Marching 66
3.4 Numerical Results and Validation 68

CHAPTER 4 - COUPLED MODEL FOR THE FLUID-STRUCTURE INTERACTION OF CHORD-WISE FLEXIBLE FOIL THRUSTERS **71**

4.1 Formulation of the fluid-structure interaction problem 71
4.2 Discretization Scheme for the Coupled Problem 76
4.2.1 Discretization Scheme for the Lifting Flow Problem 76
4.2.2 Discretization Scheme for the Structural Problem 78

4.2 Coupled BEM-FEM Numerical Scheme 80
4.3 Numerical Results 84
4.3.1 Flapping-Foil with Prescribed Deformations 84
4.3.2 Validation of the Coupled BEM-FEM Numerical Scheme 89
CHAPTER 5 - CONCLUDING REMARKS AND FUTURE RESEARCH 98
APPENDIX 100
A. Preliminaries from Functional Analysis 100
B. Hermite shape functions 102
C. Gaussian Quadrature 105
REFERENCES 106

Acknowledgements

The present dissertation, created for the fulfilment of my undergraduate studies at NTUA, is the product of a constructive effort to gain a better understanding of using mathematical modelling for engineering applications.

It has proven to be quite an exciting journey that could not have been completed without the support and guidance of my supervisor Professor K. A. Belibassakis. I would like to wholeheartedly thank him for his comments, ideas and immeasurable patience during the preparation of this thesis. I would also like to thank Professor G. Politis for encouraging me to dive into the exciting world of numerical methods and for sharing information and valuable knowledge with me. The course on fluid mechanics offered by Professor G. Triantafyllou happens to be one of my earliest encounters with hydrodynamics as a student.

During the past years I was also lucky to work with E. Filippas whose knowledge of unsteady hydrodynamics and computational tools was a significant help for me. Also, I would like to thank A. Karperaki for her support and valuable comments regarding her expertise in finite element methods and hydro-elasticity. A. Priovolos has also contributed to the fulfilment of the present work with his comments and remarks.

Finally, I want to thank my family and friends who endured my ups and downs during the preparation of this thesis.

Dimitra Anevlavi

Athens, March 2019

Abstract

Out of the numerous applications of biomimetic, aquatic inspired devices based on oscillating hydrofoils are able to achieve high levels of efficiency either for propulsion or for tidal energy extraction in nearshore and coastal regions. The ability to account and properly design for flexibility effects has the potential to further enhance the overall performance of such systems.

In the present work, a hydro-elastic model is proposed for investigating the effects of chord-wise flexibility on the performance of flapping foils with variable flexural rigidity, and whose structural response is actuated by unsteady pressure field caused by the prescribed harmonic motion of the hydro-mechanical system. A fluid-structure interaction numerical method has been developed to simulate the time-dependent structural response of the oscillating hydrofoil. We present a low order boundary element panel method (BEM) for the unsteady hydrodynamics, coupled with a finite element method (FEM) for the cylindrical bending of thin elastic plates, based on the classical Kirchhoff-Love theory.

Numerical results are presented concerning the performance of the system over a range of design and operation parameters, including Strouhal number, heaving and pitching amplitudes and effective angle of attack. To further illustrate the capabilities of the developed BEM-FEM coupled model, we validate the numerical scheme with experimental data, for the case of a chord-wise flexible thin plate under enforced heaving motion excited at the leading edge. The present model could serve as a useful tool in the design, assessment and control of biomimetic systems for renewable energy extraction.

Chapter 1 - Introduction

Biomimetic design and production emulates biological solutions in order to tackle engineering problems while preserving efficiency and environmental sustainability. It is considered to be an active research area that benefits from developments in the fields of mathematical modelling, physics and even experimental biology. The term derives from the ancient Greek words for life (*βίος*) and imitation (*μίμησις*). Living organisms through natural selection have developed structures well-adapted to their environment. A variety of fields such as agriculture, medicine, architecture, transportation, communication and energy have derived innovative solutions from the exploration of biomimicry. As progress in robotics, new materials and actuators gradually springs forward and the interest to reveal the physics behind the efficiency of locomotion in the aquatic environment remains novel biomimetic system ideas emerge. Aquatic animals use a combination of muscle contractions, fin oscillations, hydrodynamic shapes and modulation of body flexural rigidity to achieve high velocities, remarkable manoeuvrability and rapid changes in direction; see the recent work by Shyy et al. (2013).

1.1 Applications Of Biomimetic Systems

Out of the many application of biomimetic systems, flapping-wing thrusters have the potential to revolutionize commercial marine applications, by displaying significant advantages over conventional rotary propellers; see Triantafyllou et al. (2000) as well as Shyy et al. (2010), while for an extensive review refer to Rozhdestvensky & Ryzhov (2003). Flapping-wing thrusters are characterized by:

- ecologically friendly low frequency operation
- high thrust to power ratios
- superior manoeuvrability
- the ability to operate in a variety of motion regimes
- acceptable cavitation characteristic
- relatively low aerodynamic drag in the *switched off* position design versatility for operation in propulsion, stabilizer and controller modes.

However, promising results can also be found for biomimetic propulsion devices based on entirely different concepts, such as the flexible oscillating duct (FOD) inspired by jellyfish motions that was proposed and studied in the work of Politis &

Tsarsitalides (2012). The powering performance of ships equipped these FOD systems displayed superior propulsive coefficients to that of conventional propellers.

Moreover, recent experimental and theoretical work regarding the principle mechanisms for producing propulsive and transient forces in oscillating flexible bodies and fins in water have been used in state-of-the-art engineering prototyping. Such attempts aim to explore the possibility of constructing superior propulsion systems in terms of propulsive efficiency for modern autonomous underwater vehicles (AUVs). Among these projects, was the 1.2 m long laboratory robot **MIT Robotuna** that aimed to experimentally reproduce the locomotion mechanisms of the *Atlantic Bluefin tuna* and thus to reveal the physics behind it.

Another interesting application, was the small human-powered submarine **Aphalina** designed by the Saint-Petersburg State Marine Technical University. This award winning prototype was equipped with a hydro-bionic thruster and showed good speed characteristics.

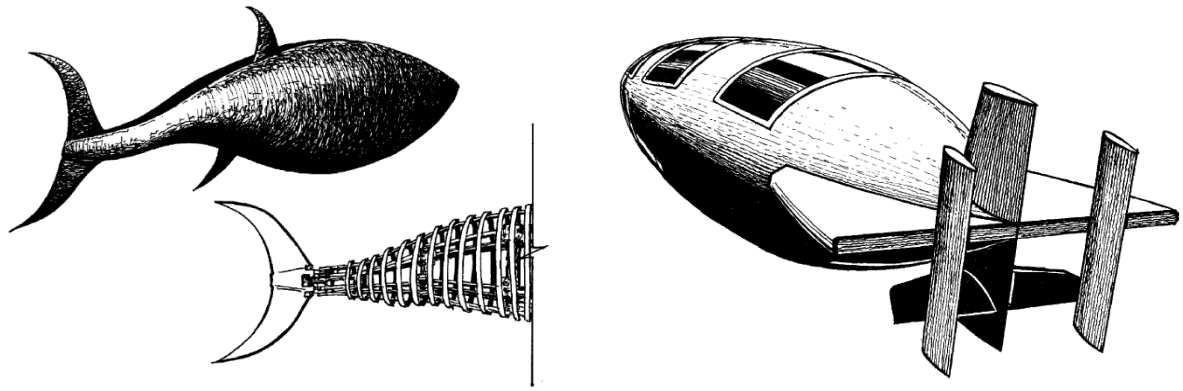

Figure 1.1 The designs of MIT laboratory robot 'Robotuna' (left) and the human-powered submarine 'Aphalina' (right) from Rozhdestvensky & Ryzhov (2003)

Thrust in most fish is generated via lateral caudal fin and body movements, but other species developed a different swimming locomotion using their median and paired fins. In body/caudal fin propulsion, where fraction of the body is displaced laterally the following categories have been identified. However, this mode's insensitivity to changes of scale, as it operates efficiently at an extended range of Reynolds number, is the reason why it is regarded as the principal means of aquatic animal propulsion, see Lighthill's earliest work on that topic (1969).

In the *Anguilliform* group, muscle contraction that produces thrust is achieved through constant-sized flexion waves propagating along the slender bodies of fish such as eels. This primitive mode of undulations concerning the whole body results in increased

drag forces and relatively inefficient locomotion. In *Sub-carangiforms* the wave propagating along the body is of higher amplitude but concerns only the rear half. This effect is concentrated in the very rear of the stiffer body and tail in the *Carangiform* group. The *Thunninform* group is comprised of the high-speed and long-distance swimmers such as tunas, with crescent shaped large tails and extremely developed caudal locomotion. Lateral movements occurring only at the area of the caudal fin account for more than 90% of the total thrust generation.

This diploma thesis is focused on the *thunninform* mode, which is considered to be the most efficient in the aquatic environment. It is found among a varied group of vertebrates such as teleost fish, sharks and marine mammals that evolved under different circumstances, see e.g. Sfakiotakis et al. (1999). In biomimetic propulsion applications, where optimization for high-speed locomotion in calm water is the key, the *thunninform* design is suitable. For slow swimming, rapid accelerations and demanding turning manoeuvring, however, that is not the case. For a more detailed classification of biological and bioinspired aquatic systems, the reader can refer to Salazar et al. (2018).

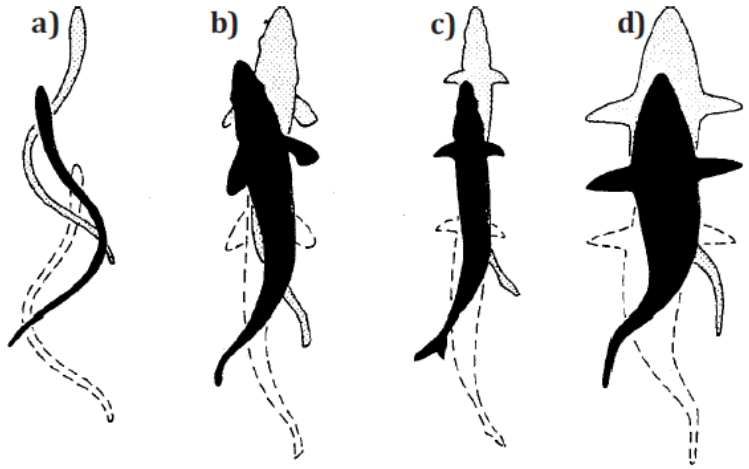

Figure 1.2 Body/caudal fin propulsion swimming modes from primitive to derived, a) anguilliform, b) sub-carangirform, c) carangiform, and d) thunninform, adapted from Prats (2015)

From a different perspective, biomimetic devices are also appropriate for efficient exploitation of wave renewable resources. Oceans have enormous wave energy reservoirs, a continuously renewed by feeding wind action. Ships moving in the seaway receive the wave energy and store it in the form of kinetic energy for heaving, pitching and other ship motions. However, uncontrolled ship motions have a negative impact in ship's operability in severe sea states. Motivated by that, in the work of Politis et al. (2014) a biomimetic wing device equipped with an active pitch control mechanism was proposed to extract this kinetic energy from the ship's motions, transform it to useful propelling power and simultaneously control and stabilize its

motions. The use of unsteady oscillating wing thrusters located beneath the hull, for the enhancement of the overall ship propulsion in the presence of waves has been studied by Belibassakis & Politis (2013) as well as Filippas & Belibassakis (2014), with the latter work also accounting for free surface effects.

Biomimetic devices are also appropriate for efficient energy extraction of wave and tidal renewable resources, especially in coastal areas. The mutual existence of waves with strong following, oblique or opposing currents at various nearshore places, which otherwise is characterized by quite low wave potential, offers a motivation for comprehensive investigation of such resources and the development of hybrid technological devices; see the extensive review by Xiao & Zhu (2014), the recent and ongoing work of Belibassakis & Filippas (2016) as well as Filippas, Gerostathis & Belibassakis (2018).

1.2 Flexible Flapping Foil Propulsion Systems

This section will serve as a short literary review on the journey that started with early observations of aquatic swimmers in nature and is heading today towards the successful engineering applications of flexible oscillating wings operating as main propulsion systems. Recent studies concerning biomimetic propulsion phenomena prominently feature:

- unsteady motions characterized by large-scale vortex structures
- flapping kinematics in 3-D
- flexible wing structures, see Shyy (2013) for more details.

To tackle this complex fluid-structure interaction problem, researchers from various fields combine their knowledge to reveal the underlying physical mechanisms that account for high propulsive efficiencies and overall performance. We start with experimental work and then we present studies of numerical modelling or simulations in this topic.

1.2.1 Experimental Studies

One of the earliest feasibility studies of an oscillating fin propulsion control system as a vehicle actuator was conducted experimentally by Yamamoto et al. (1995), showing promising results for the use on ships. Later on, Prempraneerach, Hover, & Triantafyllou (2003) showed experimentally that a properly tuned chord-wise

flexibility attribute can have a significant effect on the propulsive efficiency of 2-D flapping (heaving and pithing) foils, up to a 36% increase, compared to the efficiency of a rigid foil, with small loss in thrust. Also, a non-dimensional flexibility parameter is developed to provide a scaling law for the effects of flexibility. Another set of comprehensive experimental data, regarding the kinematics and hydrodynamics of flexible foil-like fins based on the bluegill sunfish, were produced by Lauder et al. (2006), (2007) using advanced technologies for visualization and water flow quantification.

The effect of stiffness on thrust generating plunging foils at zero freestream velocity was studied experimentally by Heathcote et al. (2004). Direct force measurements confirmed that at high plunge frequencies the thrust coefficient in intermediate stiffness foils was the greatest. The least stiff foil could generate larger thrust at low frequencies, but the increased flexibility resulted in enhanced thrust/input-power ratios. The results also suggested that there is an optimum foil stiffness for a given plunge frequency and amplitude. Heathcote et al. (2007) performed another series of water tunnel experiments with particle image velocimetry (PIV) flow field measurements for flapping motions at low Reynolds numbers, with results suggesting that the effect of chord-wise flexibility is beneficial for purely heaving foils. Motivated by these results they performed another series of water tunnel experiments, presented in Heathcote et al. (2008), to investigate the effect of span-wise flexibility on the thrust, lift and propulsive efficiency of a rectangular wing in purely heaving motions. They reported that a limited degree of flexibility was greatly beneficial, a thrust benefit of 50% was observed for a wing of intermediate flexibility and for a highly flexible wing, while the tip was observed to move out of phase with the root leading to a diminished thrust coefficient.

In the work of Baranyyk, Buckham, & Oskai (2010) a method was presented for the experimental characterization of the propulsive performance of a family of oscillating plates composed of rigid and flexible segments of various proportions. They reported which Strouhal number, oscillating frequency and heave amplitude triplets provided the highest efficiency in the positive thrust-producing regime for 15%, 50% and 100% rigid plates respectively. On the effects of submergence at different depths, it was observed that an overall increase in the thrust coefficient across the oscillation frequencies was the result of the propulsor proximity to the bottom of the channel. The flow visualization revealed the formation of large dynamic stall vortices that influenced the wake structure, and suggested that their constructive interaction with trailing edge vortices might lead to overall improvement of thrust and efficiency.

Thin foil unidirectional oscillations under fluid forces were modelled both numerically and experimentally by Alben et al. (2012). They reported good agreement

between the previously developed 2-D inviscid model and the experimental results concerning the number of wavelengths in their shape, their swimming speeds and the surrounding flows. The presented model allows for a simple analysis based on sinusoidal solutions that predicts power law scaling for the foil velocities, leading edge curvatures and shed circulation, as well as the distributions of peaks and troughs in these quantities as length and rigidity are varied.

Dewey et al. (2013) presented experimental results on the role of flexibility and aspect ratio in bioinspired aquatic propulsion. This time, the experiments were performed on flexible panels actuated with pitching oscillations at their leading edge, to investigate the scaling of thrust production, with results indicating that the global maximum in propulsive efficiency across a range of panel flexibilities is achieved when

(i) $0.25 < \text{Strouhal} < 0.35$
(ii) the frequency of motion is tuned to the structural resonant frequency of the panel.

The research verified the earlier findings of Triantafyllou et al. (1993).

Another series of experiments, performed on flexible panels actuated with heave oscillations at their leading edge, to investigate the scaling of propulsive performance we also conducted by Quinn et al. (2014). Both the trailing edge amplitude and the mode shapes of the panel were found to scale with dimensionless parameters originating from the Euler–Bernoulli beam equation. They concluded that if the panels were designed to be propulsion devices the Strouhal number in the self-propelled state would be approximately constant, and the swimming economy $u_\infty / \overline{P}$, as the ratio of freestream velocity to mean power input, would be dictated by the swimming speed.

The response of a flexible plate actuated by a harmonic heaving motion about the leading edge in a uniform flow, was also experimentally studied by Paraz, Eloy, & Schouveiler (2014). The plate's response was characterized by resonance peaks, as the forcing frequency gradually increased. The experiments were performed for a range of parameters such as the forcing frequency and amplitude, Reynolds number and rigidity revealing that nonlinearities are essential in proper fluid-structure interaction modelling.

To gain a better understanding of the effect of flexibility and flapping amplitude on thrust generation and swimming efficiency they combined the experiments on the previous model system with a weakly nonlinear analysis, see Paraz et al. (2016). The complementary theoretical model, assumed 2-D fluid flow with transverse resistive drag effects to account for the nonlinearities. A modal decomposition system motion

allowed the prediction of the plate response amplitude and generated thrust, as a function of the forcing amplitude and frequency.

The effect of flexibility on the time-averaged thrust can be beneficial for plunging foils even when the flexible region is confined to a small section near the trailing-edge, as it was reported by the experiment of Cleaver et al. (2014) using short thin plates of various flexibilities attached to foils. Across a range of frequency, amplitude and flap angle as parameters improvements in propulsion performance where estimated.

Experimental gradient-based optimization via direct force measurements and PIV was used by Quinn et al. (2015) to maximize the propulsive efficiency of a flexible plate, under combined heaving and pitching motions. Their method, well-suited for the design of flexible underwater propulsors, reveals conditions for global optimization of efficiency:

- Strouhal number is within an optimal range that varies weakly with amplitude and boundary conditions (0.40-0.53 for purely heaving motions and 0.26-0.33 for flapping motions)
- the panel is actuated at a resonant frequency of the fluid–panel system
- the heaving amplitude is tuned such that trailing-edge amplitude is maximized while the flow along the body remains attached
- the maximum pitch angle and phase lag are chosen so that the effective angle of attack is minimized.

Moreover, Richards & Oskai (2015) presented an experimental study for the investigation of the effects of the foil stiffness, inertia and oscillation kinematics on the thrust generation and efficiency of flexible oscillating-foil propulsion systems. The results revealed a damping behaviour that is affecting the dynamic structural behaviour of the foils tested. Also, the maximum efficiency occurred at the same frequency ratio that resulted in both a beneficial phasing of the deformation with respect to the driven motion and also the maximum overall amplitude of the motion.

The role of chord-wise flexural stiffness in a rectangular foil undergoing pure pitching in a uniform current has been investigated experimentally by Fernandez-Praz (2017), using digital particle image velocimetry (DPIV) and load measurements with a 6-axes balance to study flow field patterns and hydrodynamic forces. The optimum chord-wise flexibility in terms of propulsion efficiency reached 69% for the semi-flexible foil at Reynolds numbers studies. The results also indicated a strong relation between the tip amplitude and the coefficient of thrust, which should be taken into account for efficiency maximization in terms of variable flexibility for propulsion devices undergoing pitching motions.

Other parameters that offer significant improvements in the static thrust produced by oscillating flexible fins, such as variations in the stiffness profile, have been studied experimentally by Riggs et al. (2010). It has been shown that the variations in local chord-wise bending stiffness (EI) of a fin mimicking the stiffness profile of a Pumpkinseed Sunfish (Lepomis gibbosus), performed better in comparison to a fin of NACA 0012 aerofoil profile of similar dimensions.

An experimental setup has been fabricated by Kancharala et al. (2016) to measure the stiffness profiles of real fish caudal fins. Chord-wise varying stiffness robotic fins fabricated using carbon fiber reinforced composites (CFRC) have been tested in the water tunnel to evaluate their superior performance over constant stiffness fins.

1.2.2 Numerical Modelling based on Potential Theory

Applications of potential theory in the field of aquatic locomotion date back to the pioneering work of the applied mathematician M. J. Lighthill, who not only studied the different types of aquatic locomotion but employed modelling techniques to analyse high propulsive efficiency, large-amplitude undulatory motions and was also among the first to explore the so-called slender body theory, see Lighthill (1969), (1971). In the 1960s Lighthill also investigated the inviscid flow around undulatory swimmers with slender bodies of gradually variable cross-section. Slender body theory results concerning thrust production and time rates of energy shedding were obtained, indicating that the mean values of these quantities depend on the movement and body shape at the tail-end vicinity only.

As a generalization Wu (1970) solved the problem of slender fish shape optimization to determine the transverse oscillatory movements that correspond to a prescribed thrust at the expense of minimum required work for maintaining the motion. Recent revisions of Lighthill's slender body theory by Yu & Eloy (2017) also led to a useful correction so that near the trailing edge of a body moving at a high Reynolds number a Kutta condition is satisfied, producing valid results for the fluid forces calculation even at moderate aspect ratios. These studies prove that potential based methods remain very useful up to date.

Later on, Katz & Weihs (1978), (1979) presented a fluid-structure interaction model for the passive deformations of chord-wise flexible foils. A potential based model was used for the hydrodynamics in conjunction with a cantilever model for the elastic behaviour of flexible foils oscillating at large amplitude. Calculations of hydrodynamic forces, revealed that flexibility increased up to 20% compared to rigid structures, with a tolerable loss in thrust. However, very flexible foils have no practical use for engineering applications since thrust deduction is significant.

An attempt to model the entire locomotor system of a fish belonging to the *Carangiform* group was made by Cheng et al. (1998). They presented a continuous dynamic beam model, which integrates contributions from active muscle contraction, passive internal biomaterials, body inertia as well as fluid reaction. In the model a linear viscoelastic assumption is made for the passive behaviour of internal tissues, skin and backbone, while the unsteady fluid force acting on the swimmer is calculated by a 3-D waving plate theory. A review and a summary of studies on large amplitude undulatory swimming coupled to internal mechanics was presented by Pedley & Hill (1999) as one approach to the investigation of how fish achieve their remarkable swimming performance.

More recent studies by Daniel & Combes (2002) revealed to what extent the surface shape of wings and fins is controlled by structural mechanics versus fluid-dynamic loading. To address this matter, they used combinations of computational and analytical methods in order to explore how bending stresses arising from inertial-elastic mechanisms compared to stresses that correspond to fluid pressure forces. The somewhat intractable problem of fluid-solid interaction in animal flight does not need to be addressed, but for the aquatic environment that is not the case. They suggested that the coherent understanding of functional consequences of fin mechanical design, due to the high density of water itself, requires a solution to the fully coupled fluid-structure interaction problem.

From an engineering point of view, resonance and propulsion performance of flexible appendages is very important for applications. Towards that, Alben (2008) presented a 2-D vortex sheet model for the motion of a flexible body immersed in inviscid fluid and pitched periodically at the leading edge in small-amplitude regime. The results indicated that optimal efficiency is achieved as rigidity becomes small and decreases to 30-50%, depending on pitch frequency, as rigidity becomes large.

Following a similar approach, another study by Michelin & Smith (2009) investigated the influence of bending rigidity of a heaving flexible wind in a 2-D imposed parallel flow in the inviscid limit. The trailing-edge flapping amplitude is shown to be maximal for a discrete set of values of the rigidity, at which a resonance occurs between the forcing frequency and a natural frequency of the system. Such resonances induce maximum values for the mean developed thrust and power input, showing that flapping efficiency is greatly enhanced by flexibility.

Fully coupled fluid-structure interaction simulations for the passive deformations of a flapping foil with chord-wise or span-wise flexibility we carried out by Zhu (2007). The hydrodynamics are treated with a 3-D boundary element method and the structural response is approximated using a 2-D nonlinear thin plate model, with results demonstrating that the anisotropic structural flexibility of the body has

significant effects on its capability of thrust generation. This approach was later used to numerically examine the performance of a thin foil reinforced by embedded rays resembling the caudal fins Zhu & Shoele (2008). The simulations show that sensitivity of the fin to kinematic parameters; such as Strouhal number and amplitude of yaw motion, is reduced due to the fluid–structure coupling. More interestingly, even in cases when these parameters are not optimized, the flexible fin is able to function well as a propulsion device.

Priovolos et al. (2018) presented a vortex-based method for the hydro-elastic analysis of a thin hydrofoil in flapping motion, operating as a biomimetic thruster. Thickness effects as higher-order contributions to the hydrodynamics were neglected and the flexible flapping thruster was free to deform under inertia and reactive forces caused by its forced motion and hydrodynamic pressure, respectively. The proposed method was validated through a series of comparisons with other models, as well as experimental results, for the case where the foil is clamped at its leading edge, while its trailing edge acts as a free end. The results illustrated that chord-wise flexibility can significantly improve the propulsive efficiency of such devices, up to 10%, in the realistic propulsion problem concerning an autonomous underwater vehicle (AUV). This work, supported by the Laboratory of Ship and Marine Hydrodynamics at the National Technical University of Athens (NTUA), serves as the main motivation for this diploma thesis.

1.2.3 Computational Fluid Dynamics (CFD) Simulations

The fundamental basis of almost all computational fluid dynamics (CFD) problems is the Navier–Stokes equations, which define many single-phase fluid flows. Numerical simulations with an unstructured, grid-based, Navier-Stokes 3-D solver were performed by Ramamurti (2002) to investigate the fluid dynamics of force production associated with the flapping motions of the bird wrasse. Previously measured fin kinematics where incorporated in steady, quasi-steady and unsteady simulations. Comparisons of the results with experimental data revealed that steady state computation where incapable of describing the phenomenon, whereas quasi-steady state computations with correct incorporation of experimental kinematics where useful in determining trends in thrust production. On the other hand, unsteady computations where found to be in agreement with the experimental data of force magnitudes and time history.

Mittal et al. (2006) examined numerically the hydrodynamic performance of the bluegill's pectoral fin by carrying out a set of simulations using experimentally recorded kinematics. A finite-difference-based immersed boundary methodology was used successfully to model the highly deformable, membranous fin. The results,

provided information (i) vortex dynamics and formation, (ii) surface and hydrodynamic forces.

Navier-Stokes analysis was also employed by Miao & Ho (2005) to compute the unsteady, viscous flow fields associated with low-Reynolds number flows over a single chord-wise flexible foil executing prescribed plunging motions. The results showed that the propulsive efficiency is influenced primarily by the value of the reduced frequency rather than the Reynolds number and that out of the various runs performed the highest propulsive efficiency of reached 30.73%.

Pederzani & Haj-Hariri (2006) presented a numerical method for the analysis of flexible bodies in unsteady viscous flow that models the foil body as an active flexible skin that actually drives the flow. Their fully implicit fluid-structure interaction methodology was validated by reproducing well-established results for vortex shedding from a stationary as well as an oscillating rigid cylinder.

Luo et al. (2010) developed a 3-D, high-fidelity numerical approach to simulate the interaction between a viscous, unsteady flow and deformable thin structures. The flow solver was based on versatile sharp-interface immersed-boundary method in conjunction with a non-linear finite-element methods with capability of large deformations and various element types (frame, membrane, plate and shells) for the structural response. The flow-structure interaction in computed using an iterative and implicit approach.

Sousa & Allen (2011) studied numerically the efficiency of thrust-producing 2-D inextensible membranes with variable bending rigidities undergoing pitching motions in a uniform flow. The dynamic response of the membranes was computed using a fluid/structure interaction method that couples a compact finite difference immersed-boundary method with a thin-membrane structural solver. The simulation results, showed that the thrust coefficient is primarily a function of Strouhal number, increasing monotonically for increasing values of St. Efficiency increases for increasing structural mass coefficient and reaches a minimum for intermediate values of the bending rigidity. The most interesting aspect of these results is the relatively high values for efficiency that can be obtained for such a simple configuration.

Dai et al. (2012) numerically investigated the effects of wing stiffness, mass ratio, phase angle of active pitching, and Reynolds number on the hydrodynamic performance of an elastic wing in hovering motion, clamped to a rigid leading edge. The code couples a viscous incompressible flow solver based on the immersed-boundary method and a nonlinear finite-element solver for thin-walled structures. The dynamic pitching depends not only on the specified kinematics at the wing root and the stiffness of the wing, but also greatly on the mass ratio, which represents the

relative importance of the wing inertia and aerodynamic forces in the wing deformation.

In another work by Dai et al. (2012) the propulsive performance of an elastic plate of aspect ratio 0.54 and mass ratio 0.1 that pitches around its leading edge in a free stream at Reynolds number 640, was numerically investigated. The fluid–structure interaction is achieved by combining a second-order, Cartesian-grid based immersed-boundary flow solver, and a finite-element solver that can handle geometric nonlinearity of a thin-walled structure. It was found that for the rigid plate and the flexible plate with the first-mode deformation, the thrust coefficient nearly collapses onto the same curve when plotted against the Strouhal number defined using the tail excursion. Exceptions were found in overly flexible plates that indicated higher deformation modes. On the other hand, the flexible plate has significantly higher power efficiency than the rigid plate at the same Strouhal number.
Finally Bourlet et al. (2015) presented a numerical study of the self-induced flapping motion of a flexible cantilever foil in a uniform axial flow, by employing a high-order fluid-structure solver based on fully coupled Navier-Stokes and non-linear structural dynamics equations. They investigated the evolution of the unsteady laminar boundary layer and showed that the induced tension within the foil is dominated by pressure effects and only marginally affected by skin friction.

1.3 Flexible Biomimetic Wave and Tidal Energy Extraction Devices

The study of wave and tidal energy extraction systems based on flexible structures is a relatively modern field of research with emphasis on efficiency and sustainability**.** The effects of chord-wise flexibility on the power extraction potential of a kinetically constrained oscillating thin plate that undergoes a heaving and pitching motion have only been studied by Jeanmond & Olivier (2017). In their work they presented a 2-D fully coupled fluid-structure interaction model based on a second-order finite-volume solver using the OpenFOAM library for the fluid flow in conjunction with a finite-element solver for the beam equation with Hermite shape functions. The results presented were very promising, showing that flexible plates can extract up to more than twice the power of the corresponding rigid ones and that the dimensionless flexibility appears to be a key factor involved in the resonance phenomenon that greatly affects the flow field.

Chapter 2 - Hydrodynamics of Flapping Foils with Prescribed Deformations

In the present work a symmetric wing of infinite span is considered to be fully submerged into the surrounding incompressible fluid. Under the assumption that the boundary layer around the streamlined foil is very thin, the negligence of viscous effects can be justified and the resulting flow on the exterior of the boundary layer can be modelled as a 2-D irrotational flow. The unsteady lifting flow problem of a flapping foil with prescribed deformations is treated with a non-linear pressure-type Kutta condition and frozen wake modelling for the trailing vortex sheet. A low order potential (panel) method has been implemented for the numerical approximation of the aforementioned problem. Significant 3-D and viscous effects are neglected under these assumptions, but nevertheless a quantitative understanding of the performance of wings with high aspect ratios is gained. In that sense, the present model could serve as a useful tool for the calculation of chord-wise pressure distribution in the preliminary design phase of biomimetic devices, suitable for propulsion or wave and current energy extraction.

This Chapter begins with a brief literature review of Boundary Element Methods and the mathematical formulation of the unsteady hydrodynamic problem in an unbounded domain for the case of an oscillating foil with prescribed deformations is presented. Then, the numerical treatment of the aforementioned problem is presented using Boundary Element Methods (BEM). Numerical results are presented concerning the thrust coefficient and the efficiency of the flapping foil operating as a thrust producing system over a range of design and operation parameters for the case of rigid flapping foils. Furthermore, results concerning the overall propulsive performance of the system with prescribed deformations are presented to illustrate effects of chord-wise flexibility.

These numerical results were obtained using a BEM-solver that was initially developed by Filippas & Belibassakis (2014), Filippas (2019) and has been extended, within the framework of this diploma thesis, to treat the problem of chord-wise flexible foils.

2.1 Brief Literature Review on Boundary Element Methods

During the past decades, approximate numerical solutions proved to be a vital part of the research conducted both by engineers and physical scientists. Boundary Element Methods (BEM) refer to numerical techniques concerning the solution approximation of boundary integral equations (BIE). The purpose of BEMs is to specify an approximate solution that is an exact solution of the differential equation in the domain but satisfies the boundary conditions at a finite set of points. These methods first became known through the pioneering work of Russian mathematicians such as Mikhlin (1965) whose monograph in the theory of integral equations is considered a masterpiece. These formulations enabled the solution of partial differential equations for diffusion problems, acoustic wave propagation, elastoplasticity, fracture mechanics and among others fluid mechanics Brebbia et al. (1984). However since a more detailed overview of the wide range of BEM engineering applications is not the purpose of this literature review, from now on emphasis will be given to the use of BEM in aerodynamics.

During the 1960s-80s several engineers such as Hess contributed by implementing the method for fluid mechanics and aerodynamics. The earliest works by Hess & Smith (1964) concerned the non-lifting flows around arbitrary 3-D bodies, but as experience gathered modelling 3-D aircraft lifting flows J.L & Friedman (1981) as well as the steady flow around propellers Hess & Valarezo (1985) was achieved. Meanwhile, the lack of comprehensive text for this field was covered by the works of notable scientists such as Moran (1984), Katz & Plotkin (1991). Boundary element methods present some interesting advantages over other popular numerical methods, such as Finite Difference or Finite Element Methods:

- Dimensionality reduction, since the discretization schemes are implemented only on the boundary. Therefore the approximate solution of the 3-D formulation of a problem is equivalent to the determination of the unknowns on the specified 2-D boundary.
- Handling unbounded domain problems with some closed boundaries is as easy as solving interior problems, since the unknown quantities, referring to the closed boundaries contain all the necessary information.
- Reduction of computational cost is significant in various cases where integral terms can be evaluated analytically.
- Especially for lifting flow problems, the boundary values of the solution and the corresponding derivatives contain all the physical information required. These data can be directly derived from the boundary integral equations.

However implementing Boundary Element Methods proves to be challenging due to the following:

- Explicit knowledge of a fundamental solution for the differential equation is essential. Having a fundamental solution implicitly assumes homogeneity in the far-field, which is unrealistic in many problems. In some cases though where the fundamental solution is known but computationally costly other numerical methods could prove to be preferable.
- The most suitable solutions to the differential equations are singularities in the form of sources, dipoles and vortices. This type of singularities though, comes with some challenging properties. Integration of singular kernels in many cases requires special treatment, in particular where analytical formulas are not available.

2.2 Definition of the Unsteady Lifting Flow Problem

Let us consider the fluid flow *domain* or *region* as an open domain $D \subseteq R^2$ with corresponding boundaries $\partial D = \partial D_B \cup \partial D_W$ that are assumed smooth in the sense of Lyapunov (Gunter, 1967), everywhere except from the trailing edge. The first component ∂D_B refers to the surface of the foil and the second ∂D_W to the trailing vortex sheet. The time-dependent boundaries $\partial D_B = \partial D_B(t)$ and $\partial D_W = \partial D_W(t)$ are denoted with respect to an inertial reference frame.

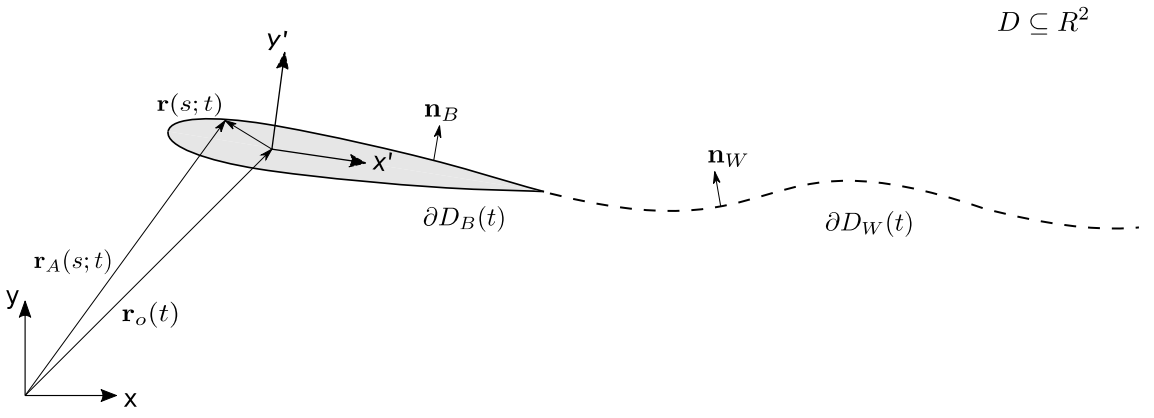

Figure 2.1 Introducing the inertial and body-fixed coordinate systems

The unsteady lifting flow model that is presented in this thesis is in accordance with the notion of a deformable foil surface as well as wake evolution in time. The following coordinate systems are introduced in this work:

- an **earth-fixed coordinate system** at which each point is represented by the $(x(t), y(t))$ or $(x, y; t)$ coordinates
- a **non-inertial body-fixed coordinate system**, fixed at the foil's centre of rotation along chord length with no inclination, in which an arbitrary point is represented by $(x'(t), y'(t))$ or $(x', y'; t)$
- a **body-fixed curvilinear coordinate system** defined on the boundary with each point represented as $r(s(t))$ or $r(s; t)$

The normal and tangent unit vectors, denoted as $\mathbf{n}(s;t)$ and $\boldsymbol{\tau}(s;t)$ respectively, are defined uniquely at each point on the boundary using the body-fixed curvilinear. It is noted, that these unit vectors are time-dependent in order to comply with the modelling of a deformable boundary. However, for rigid hydrodynamics the normal and tangent unit vectors are only dependent on the s parameter, i.e. $\mathbf{n}(s)$ and $\boldsymbol{\tau}(s)$ respectively.

The corresponding potential field $\Phi\left(x, y; t\right)$ with respect to the inertial reference frame is defined as a twice differentiable function in D. The boundary value of the potential $\Phi^*\left(x, y; t\right)$ is also defined on the boundary, following a specific limiting process. Generally the boundary value of Φ on ∂D denoted by the function Φ^*, that can be discontinuous through the boundary at point $A \in \partial D$, is constructed by the following formula

$$\Phi^*(s;t) = \lim_{\delta \to 0} \Phi\left\{\mathbf{r}_A(s;t) + \mathbf{n}_A(s;t)\delta\right\} \tag{2.1}$$

where δ is a small parameter and $\mathbf{n}_A$ a unit vector at point A not tangent to ∂D. More details can be found in the work of Politis (2011).

The body kinematics are defined with respect to the inertial reference frame, however for an arbitrary point $A \in \partial D_B$ we have the following representation,

$$\mathbf{r}_A(s;t) = \mathbf{r}_o(t) + \mathbf{r}(s;t) \tag{2.2}$$

where $\mathbf{r}(s;t)$ is used to describe the geometry of the foil in the body-fixed coordinate system and $\mathbf{r}_O(t)$ contains the motion of the foil's centre of rotation with respect to the inertial reference frame as shown in Figure 2.1.

In this Chapter, the following notation is used:

- $\partial / \partial t$ denotes the time rates in the inertial reference frame
- d / dt denotes the time rates in the body-fixed reference frame

The velocity of an arbitrary point on the body boundary with respect to the inertial reference frame is therefore given as

$$\mathbf{V}_A(s;t) = \partial_t \mathbf{r}_A(s;t) \tag{2.3}$$

Moreover, a velocity potential $\Phi(x,y;t)$ can be defined and $\nabla\Phi(x,y;t)$ denotes the potential gradient at an arbitrary point $(x,y;t)$. The **governing equation** for the potential field known as Laplace equation, can be derived from the law of mass conservation under the assumptions of **irrotationality** of the flow.

$$\nabla^2\Phi(x,y;t) = 0 \tag{2.4}$$

As far as boundary conditions are concerned, on the moving boundary of a moving body, a no-entance boundary condition must be satisfied.

$$\nabla\Phi(x,y;t)\cdot\mathbf{n}_B = \mathbf{V}_B\cdot\mathbf{n}_B \quad (x,y;t)\in\partial\mathrm{D}_B(t) \tag{2.5}$$

where $\mathbf{n}_B$ refers to the unit normal vector on the body boundary pointing in D. The behaviour of the potential field at infinity can be modelled as shown below; ensuring that at infinity the velocity field of the domain is not affected by the perturbations caused by the unsteady motion of the foil.

$$\lim_{\|x\|\to\infty}\Phi = 0, \ \lim_{\|x\|\to\infty}\nabla\Phi = 0 \tag{2.6}$$

Furthermore, on the trailing wake the following kinematic and dynamic conditions must hold. The superscripts $\{u,l\}$ are used to denote wake's upper and lower side respectively in addition to the use of indices $\{B,W\}$ for denoting values of $\Phi(x,y;t)$ on the body surface and the wake of the hydrofoil respectively.

The following kinematic condition ensures the continuity of the normal velocity vector through the wake,

$$\frac{\partial\Phi_W^u(x,y;t)}{\partial n} = \frac{\partial\Phi_W^l(x,y;t)}{\partial n}, \ (x,y;t)\in\partial D_W(t) \tag{2.7}$$

whereas the physical meaning behind the dynamic condition, that is the inability of the wake to support pressure difference

$$p_W^u(x,y;t) = p_W^l(x,y;t), \quad (x,y;t)\in\partial D_W(t) \tag{2.8}$$

To proceed, we recall the approximate form of Bernoulli's theorem, with $d\Phi^* / dt$ denoting the rate of change of the trace of the potential with respect to a body-fixed reference frame

$$\frac{p}{\rho} = -\frac{d\Phi^*}{dt} + \nabla\Phi \cdot \left(\mathbf{V}_B\right) - \frac{1}{2}\left(\nabla\Phi\right)^2 \tag{2.9}$$

Using the kinematic and dynamic conditions in equations (2.7) & (2.8) along with Bernoulli's theorem in (2.9) we derive the following,

$$\frac{D\mu_W\left(x,y;t\right)}{Dt} = 0, \quad (x,y;t) \in \partial D_W(t) \tag{2.10}$$

where $\mu_W = \Phi_W^u - \Phi_W^l$ denotes the potential jump (dipole intensity) on the wake and $D/Dt = \partial/\partial t + \mathbf{V}_m \cdot \nabla$ is the material derivative based on the mean total velocity $\mathbf{V}_m = 0.5\left(\nabla\Phi_T^u + \nabla\Phi_T^l\right)$ on the trailing vortex sheet. The conditions discussed above result in an equation regarding the dipole intensity of the sheet, which determines the time evolution of the wake boundary ∂D_W.

In the present work, time evolution of the trailing vortex sheet comes with prescribed kinematics. In this simplified wake model the vortices emitted from the trailing edge remain were shed. This linearization of the free wake dynamics leads to a significant simplification in the modelling, while providing satisfactory predictions in cases of moderately low unsteadiness. Similar wake models have also been described and used in the work of La Mantia & Dabichki (2009), (2011) and (2013).

Extensions concerning the modelling of the non-linear free-wake dynamics are proposed as future work. The transport of trailing vorticity in the wake with respect to the body-fixed reference frame for the linearized wake model is expressed as

$$\mu_W\left(\mathbf{x};t\right) = \mu_W\left(\mathbf{x} + \mathbf{V}_{TE}\Delta t; t - \Delta t\right), \quad \mathbf{x} \in \partial D_W \tag{2.11}$$

where $\mathbf{V}_{TE}$ denotes an appropriate velocity determined from the derivative of the trailing edge's motion. However, in the present study we have chosen the bisector of the trailing edge for the transport of trailing vorticity in the wake. Closer examination of the effects of changes in the direction towards which the transport of trailing vorticity occurs in the wake is also an interesting aspect that should be investigated in the future.

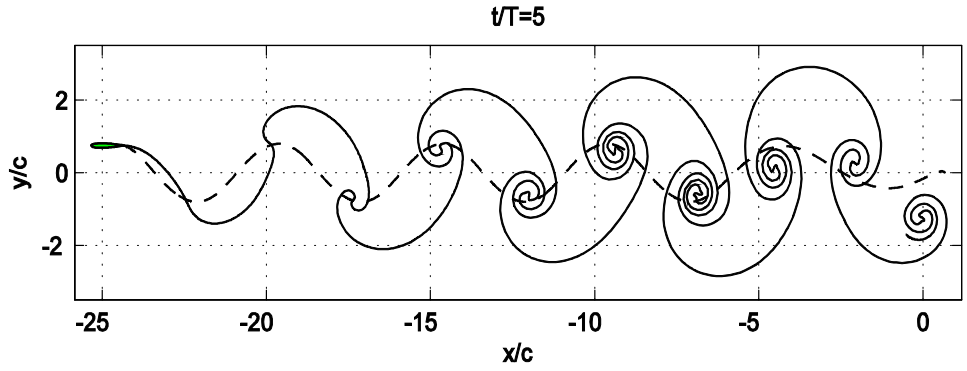

Figure 2.2 Time-evolution of trailing vortex sheet for flapping foil motion Filippas et al. (2014). Free wake mode (solid line) compared with simplified-wake linear mode (dashed line).

2.2.1 Pressure-type Kutta Condition

The existence of the trailing vortex sheet introduces complexity and requires boundary conditions which are different from the ones satisfied on the body boundary. Therefore a Kutta condition needs to be introduced for a unique solution to be obtained and fully close the initial boundary value problem. This ensures that at the trailing edge finite values of velocity occur and that the flow is smooth. In the present method the standard version of the pressure type Kutta condition that is implemented requires the pressure difference at the trailing edge to be zero and contains non-linear terms.

Under the assumption that the pressure field is continuous in $\bar{D}$, at the trailing edge defined as $\partial D_B \cap \partial D_W$ is holds,

$$p_B^u(x_{TE}, y_{TE}; t) = \lim_{(x,y)\to(x_{TE},y_{TE})} p_B^u(x_B, y_B; t) = \lim_{(x,y)\to(x_{TE},y_{TE})} p_W^u(x_W, y_W; t) = p_W^u(x_{TE}, y_{TE}; t) \tag{2.12}$$

$$p_B^l(x_{TE}, y_{TE}; t) = \lim_{(x,y)\to(x_{TE},y_{TE})} p_B^l(x_B, y_B; t) = \lim_{(x,y)\to(x_{TE},y_{TE})} p_W^l(x_W, y_W; t) = p_W^l(x_{TE}, y_{TE}; t) \tag{2.13}$$

where $(x_B, y_B) \in \partial D_B$, $(x_W, y_W) \in \partial D_W$, $(x_{TE}, y_{TE}) \in \partial D_B \cap \partial D_W$.

The classic pressure-type Kutta condition is now obtained from (2.8) and (2.12) & (2.13) as it follows,

$$p_B^u(x, y; t) = p_B^l(x, y; t), \quad (x, y; t) \in \partial D_B(t) \cap \partial D_W(t) \tag{2.14}$$

After Bernoulli's theorem in equation (2.9) is applied to the upper and lower sides of the trailing edge we obtain,

$$\frac{p_{TE}^{u}}{\rho} = -\frac{d\Phi_{TE}^{u\ *}}{dt} - \frac{1}{2}\left(\nabla\Phi_{TE}^{u} - \mathbf{V}_{B}^{u}\right)^{2} + \frac{1}{2}\left(\mathbf{V}_{B}^{u}\right)^{2},\ \ p_{TE}^{u} = p_{B}^{u}(x_{TE}, y_{TE}; t) \tag{2.15}$$

$$\frac{p_{TE}^{l}}{\rho} = -\frac{d\Phi_{TE}^{l\ *}}{dt} - \frac{1}{2}\left(\nabla\Phi_{TE}^{l} - \mathbf{V}_{B}^{l}\right)^{2} + \frac{1}{2}\left(\mathbf{V}_{B}^{l}\right)^{2},\ \ p_{TE}^{l} = p_{B}^{l}(x_{TE}, y_{TE}; t) \tag{2.16}$$

Substituting relations (2.15) & (2.16) into equation (2.14) we obtain

$$\frac{d\left(\Phi_{TE}^{u\ *} - \Phi_{TE}^{l\ *}\right)}{dt} + \frac{1}{2}\left(\nabla\Phi_{TE}^{u} - \mathbf{V}_{B}^{u}\right)^{2} - \frac{1}{2}\left(\nabla\Phi_{TE}^{l} - \mathbf{V}_{B}^{l}\right)^{2} + \frac{1}{2}(\mathbf{V}_{B}^{l})^{2} - \frac{1}{2}(\mathbf{V}_{B}^{u})^{2} = 0 \tag{2.17}$$

The following formula

$$\nabla\Phi_{B} = \nabla\Phi_{\mathrm{B}}^{*} + \underbrace{\left[\left(\mathbf{V}_{B}\right)\mathbf{n}_{B}\right]}_{b}\cdot\mathbf{n}_{B} \tag{2.18}$$

expresses the relation between values of the tangent velocity and the normal velocity on the body-boundary (Politis G. , 2011).

By substituting relation (2.18) in equation (2.17) we can derive the nonlinear pressure-type Kutta condition,

$$\frac{d\left(\Phi_{TE}^{u\ *} - \Phi_{TE}^{l\ *}\right)}{dt} + \frac{1}{2}\left(\nabla\Phi_{TE}^{u\ *} + b^{u}\cdot\mathbf{n}_{B}^{u} - \mathbf{V}_{B}^{u}\right)^{2} - \frac{1}{2}\left(\nabla\Phi_{TE}^{l\ *} + b^{l}\cdot\mathbf{n}_{B}^{l} - \mathbf{V}_{B}^{l}\right)^{2} + \frac{1}{2}(\mathbf{V}_{B}^{l})^{2} - \frac{1}{2}(\mathbf{V}_{B}^{u})^{2} = 0 \tag{2.19}$$

$$\Rightarrow \frac{d\left(\Phi_{TE}^{u\ *} - \Phi_{TE}^{l\ *}\right)}{dt} + \left(\frac{\nabla\Phi_{TE}^{u\ *} + \nabla\Phi_{TE}^{l\ *}}{2} + b\ \cdot\mathbf{n}_{B} - \mathbf{V}_{B}\right)\cdot\left(\nabla\Phi_{TE}^{u\ *} - \nabla\Phi_{TE}^{l\ *}\right) = 0 \tag{2.20}$$

2.2.2 Representation Theorem - Boundary Integral Equation (BIE)

The solution of the lifting flow problem is obtained when Green's theorem is applied and the total potential is expressed as a function of the boundary values of the potential Φ and its derivative $\frac{\partial \Phi}{\partial n}$. Therefore for each $(x_o, y_o) \in D$

$$\begin{aligned}\Phi(x_0,y_0;t) = &\int_{\partial D_B(t)} \frac{\partial \Phi_B(x,y;t)}{\partial n} G(x_0,y_0 \mid x,y) - \Phi_B(x,y;t) \frac{\partial G(x_0,y_0 \mid x,y)}{\partial n} ds(x,y) \\ &+ \int_{\partial D_W^u(t)} \frac{\partial \Phi_W^u(x,y;t)}{\partial n} G(x_0,y_0 \mid x,y) - \Phi_W^u(x,y;t) \frac{\partial G(x_0,y_0 \mid x,y)}{\partial n} ds(x,y) \\ &+ \int_{\partial D_W^l(t)} \frac{\partial \Phi_W^l(x,y;t)}{\partial n} G(x_0,y_0 \mid x,y) - \Phi_W^l(x,y;t) \frac{\partial G(x_0,y_0 \mid x,y)}{\partial n} ds(x,y)\end{aligned} \quad (2.21)$$

where

$$G(x_0,y_0 \mid x,y) = \frac{1}{2\pi} \ln r(x_0,y_0 \mid x,y) \quad (2.22)$$

$$\frac{\partial G(x_0,y_0 \mid x,y)}{\partial n} = -\frac{1}{2\pi} \frac{\mathbf{n} \cdot \mathbf{r}(x_0,y_0 \mid x,y)}{\left[r(x_0,y_0 \mid x,y) \right]^2} \quad (2.23)$$

and

$$\mathbf{r}(x_0,y_0 \mid x,y) = \left\{ (x_0 - x), (y_0 - y) \right\}, r = \left| \mathbf{r} \right| \quad (2.24)$$

where ∂D_W^u , ∂D_W^l denote the upper and the lower sides of the shear layer respectively and the following functions in (2.22) and (2.23) refer to fundamental solution of Laplace equation in two-dimensions known as Green's function and its derivative respectively. More details about the theory of linear integral equations can be found in the work of Kress (1989).

As far as the physical interpretation of (2.21) is concerned the first term on the right hand side is the potential induced at point (x_0, y_0) from sources of $\frac{\partial \Phi_B(x,y;t)}{\partial n}$ intensity distributed at the body boundary. The second term expresses the potential induced from a dipole singularity distribution along body boundary of $\Phi_B(x,y;t)$ intensity. The same holds for the singularity distributions along the upper and lower side of the shear layer.

Green's formula can also be applied for every point (x_0, y_0) on the boundary ∂D

$$\frac{1}{2}\Phi_B(x_0,y_0;t) = \int_{\partial D_B(t)} \frac{\partial \Phi_B(x,y;t)}{\partial n} G(x_0,y_0 \mid x,y) - \Phi_B(x,y;t)\frac{\partial G(x_0,y_0 \mid x,y)}{\partial n} ds(x,y)$$
$$+ \int_{\partial D_W^u(t)} \frac{\partial \Phi_W^u(x,y;t)}{\partial n} G(x_0,y_0 \mid x,y) - \Phi_W^u(x,y;t)\frac{\partial G(x_0,y_0 \mid x,y)}{\partial n} ds(x,y) \quad (2.25)$$
$$+ \int_{\partial D_W^l(t)} \frac{\partial \Phi_W^l(x,y;t)}{\partial n} G(x_0,y_0 \mid x,y) - \Phi_W^l(x,y;t)\frac{\partial G(x_0,y_0 \mid x,y)}{\partial n} ds(x,y)$$

At this point we use (2.7) and (2.10) to derive the following *2nd Fredholm-kind* weakly singular integral equation. For $(x_0, y_0) \in \partial D$

$$\frac{1}{2}\Phi_B(x_0,y_0;t) + \int_{\partial D_B(t)} \Phi_B(x,y;t)\frac{\partial G(x_0,y_0 \mid x,y)}{\partial n} ds(x,y) =$$
$$\int_{\partial D_B(t)} \underbrace{\boldsymbol{V}_B \cdot \boldsymbol{n}_B}_{b\ x,y;t} G(x_0,y_0 \mid x,y) ds(x,y) - \int_{\partial D_W(t)} [\![\Phi_W]\!](x,y;t)\frac{\partial G(x_0,y_0 \mid x,y)}{\partial n} ds(x,y) \quad (2.26)$$

where $\Phi_W = \Phi_W^u - \Phi_W^l = \mu_W$ denotes the potential jump or the dipole intensity on the wake. Since Kelvin's theorem holds, the potential jump at the trailing edge is equal to the value of circulation around the foil at time *t* and in problems of unsteady motion this value changes over time.

$$\Gamma(t) = \oint_{\partial D_B(t)} \nabla\Phi(x,y;t) ds(x,y) = \Phi_{\mathrm{TE}}(t) \quad (2.27)$$

We conclude at this point that under the physical interpretation of (2.10), according to which the trailing wake behaves as a material curve, that $[\![\Phi_W]\!]$ is not constant along the wake boundary ∂D_W since it changes over time representing the history of circulation. Information about the circulation at each time step is stored in values of potential jump μ_W on ∂D_W with the last integral term in the boundary integral equation (BIE) in (2.26), expressing the memory effect of the wake.

The BIE in relation together with Kutta condition in (2.20) provide us with a system of equations for the unknown boundary fields $\Phi_B(x,y;t)$ on the body boundary and the dipole intensity μ_W at the vicinity of the trailing edge. The solution of the aforementioned problem can be achieved using different approaches which are presented and discussed in more detail in Section 2.3.1.

2.3 Discretization Scheme for BEM

In the present study a low-order potential based boundary element (panel) method has been implemented to model numerically the unsteady flapping foil motion in infinite 2-D domains. The discretization scheme begins with an appropriate boundary approximation. In our case the boundary ∂D is decomposed into a finite number of line segments, the so called *boundary elements*. Each element is characterized by its end points and the mid-point; denoted as *nodes* and *collocation points* respectively, see e.g. the discretization on the body boundary of the foil in Figure 2.3. Since the boundaries introduced in the mathematical formulation are time-dependent, the boundary elements on the trailing wake will be increased in number as time evolves, whereas on the deformable foil body changes in the boundary element's length are allowed.

The fundamental solution in (2.22) satisfies the governing equation everywhere on the domain, therefore the next step towards the discretization is to satisfy approximately the boundary conditions on both the body boundary and the trailing wake in their discretized version. We assume that on the boundary we have piecewise-constant intensity distributions of the fundamental solution and its derivative, also known in fluid mechanics terminology as source and dipole respectively.

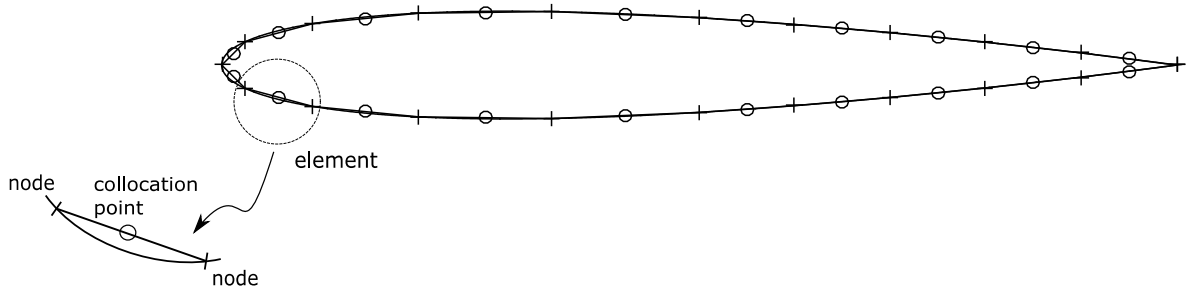

Figure 2.3 Boundary discretization and boundary elements for a NACA 0012 airfoil

On the body boundary we use distributions of both sources and dipoles, whereas on the trailing wake solely dipoles. This is essential in order to comply with the dynamic condition on the wake in equation (2.8), since the trailing wake as a material surface cannot support pressure difference.

Therefore, on the discretized boundary we have piecewise-constant distribution of the potential,

$$\Phi_B(x,y;t) = \Phi_{Bi} \quad \text{i=1,...N}_B \tag{2.28}$$

$$\Phi_W \ (x,y;t) = \ \Phi_{W\ i} = \mu_{Wi} \quad \text{i=1,...N}_W \tag{2.29}$$

Also, for the discretized no-entrance boundary condition we have,

$$\frac{\partial \Phi_B(x,y;t)}{\partial n} = \frac{\partial \Phi_{Bi}}{\partial n} = \left[\vec{V}_B \cdot \vec{n}_B\right]_i = \vec{b}_i \quad \text{i=1,...N}_B \tag{2.30}$$

Finally, we assume that the boundary integral equation (BIE) is satisfied at a finite number of points, known as *collocation points.* In the present study the mid-point of the boundary elements have been chosen to the be collocation points. This also holds for the Pressure-type Kutta condition, presented in equation (2.20).

For (x_i, y_i) , $i = 1,...N_B$

$$\sum_{j=1}^{N_B}\left(\frac{\delta_{ij}}{2} + B_{ij}\right)\Phi_{Bj} = \sum_{j=1}^{N_B}\left(A_{ij}\right)\underbrace{\left[\mathbf{V}_B \cdot \mathbf{n}_B\right]_j}_{b_j} + \sum_{j=2}^{N_F}\left(-B_{ij}\right)\mu_{Wj} + \left(-B_{i1}\right)\mu_{W1} \tag{2.31}$$

where δ_{ij} is the Kronecker delta and A_{ij}, B_{ij} are induction factors.

The term μ_{Wj} approximates the potential jump (dipole intensity) on the trailing wake thus denoting memory effects, while μ_{W1} refers to the potential jump on the wake element that is closest to the trailing edge. This panel element is also denoted as the Kutta-strip**.** At each time step a new element is generated on the wake with unknown dipole intensity μ_{W1}.

The induction factors A_{ij}, B_{ij} represent the induction potential at collocation point-*i* due to a source or dipole distribution located at panel-*j* and are defined as follows

$$A_{ij} = \int_{panel\ j} G_s(x_i, y_i \mid x_j, y_j)\, ds(x_j, y_j) \tag{2.32}$$

$$B_{ij} = \int_{panel\ j} \frac{\partial G_s(x_i, y_i \mid x_j, y_j)}{\partial n}\, ds(x_j, y_j) \tag{2.33}$$

Despite occurring singularities the above integrals (2.32) & (2.33) for low-order panel methods can be evaluated analytically, see e.g. Katz & Plotkin (1991) as well as Moran (1984). This proves to be a significant advantage and gain in computational cost. Otherwise, adaptive integration techniques can be used for the numerical calculation of singular integrals, see e.g. Filippas (2019).

The matrix form of equation (2.31) holds as is,

$$\mathbf{A} \cdot \mathbf{\Phi}_B = \mathbf{S} \cdot \mathbf{b} + \mathbf{W} \cdot \boldsymbol{\mu}_W + \mathbf{W}_K \mu_{W1} \tag{2.34}$$

where

$\mathbf{S} = \left\{A_{ij}\right\}$, $\text{i} \in \{1,...\text{N}_B\}$, $\text{j} \in \{1,...\text{N}_B\}$

$$\mathbf{W}=\left\{-B_{ik}\right\},\ \mathbf{W}_K=\left\{-B_{i1}\right\},\ i\in\left\{1,...,N_B\right\},\quad k\in\left\{2,...,N_W(t)\right\}$$

The Dirchlet-toNeumann operator (DtN) is introduced using the inverse matrix of $\mathbf{A}^{-1}$ in the discretized form of the BIE. This operator sets a mapping between the boundary values of the potential and their normal derivatives, by containing essential information regarding the distribution of sources and dipoles on the body boundary. It is important to note that this operator remains unchanged in rigid body problem, but that is not the case if deformations occur. In that sense, flexible body hydrodynamics are computationally more demanding than the rigid body simulations. We can reformulate (2.34) as,

$$\mathbf{\Phi}_{\mathrm{B}}=\mathbf{D}\cdot\mathbf{b}+\mathbf{P}\cdot\boldsymbol{\mu}_W+\mathbf{Z}\mu_{W1} \tag{2.35}$$

$$\mathbf{P}(\mu_W)=\mathbf{A}^{-1}\left(\mathbf{W}\cdot\boldsymbol{\mu}_W\right) \tag{2.36}$$

where $\mathbf{D}=\mathbf{A}^{-1}\mathbf{S}$ denotes the DtN operator.

The discretised form of the non-linear Pressure-type Kutta condition is presented below with the non-linear and linear terms presented separately for convenience. The interested reader can also refer to Filippas & Belibassakis (2014), Filippas (2019).

$$\frac{d\left(\Phi_{\mathrm{B,N_B}}-\Phi_{\mathrm{B},1}\right)}{dt}=\mathscr{L}+\mathscr{N} \tag{2.37}$$

$$\mathscr{L}=\frac{\left(\mathbf{g}_1-\mathbf{g}_2\right)\boldsymbol{\tau}_1}{2d_1}\left(\Phi_{\mathrm{B},2}-\Phi_{\mathrm{B},1}\right)-\frac{\left(\mathbf{g}_1+\mathbf{g}_2\right)\boldsymbol{\tau}_{N_B}}{2d_{N_B-1}}\left(\Phi_{\mathrm{B,N_B}}-\Phi_{\mathrm{B},N_B-1}\right)-\frac{\mathbf{g}_1\mathbf{g}_2}{2}-g_3 \tag{2.38}$$

$$\mathscr{N}=-\frac{1}{2}\left[\frac{\boldsymbol{\tau}_{N_B}}{d_{N_B-1}}\left(\Phi_{\mathrm{B,N_B}}-\Phi_{\mathrm{B},N_B-1}\right)+\frac{\boldsymbol{\tau}_1}{d_1}\left(\Phi_{\mathrm{B},2}-\Phi_{\mathrm{B},1}\right)\right]\cdot\left[\frac{\boldsymbol{\tau}_{N_B}}{d_{N_B-1}}\left(\Phi_{\mathrm{B,N_B}}-\Phi_{\mathrm{B},N_B-1}\right)-\frac{\boldsymbol{\tau}_1}{d_1}\left(\Phi_{\mathrm{B},2}-\Phi_{\mathrm{B},1}\right)\right] \tag{2.39}$$

$$\mathbf{g}_1=\left(b\cdot\mathbf{n}\right)_{B,N_B}+\left(b\cdot\mathbf{n}\right)_{B,1}-\mathbf{V}_{B,N_B}-\mathbf{V}_{B,1} \tag{2.40}$$

$$\mathbf{g}_2=\left(b\cdot\mathbf{n}\right)_{B,N_B}-\left(b\cdot\mathbf{n}\right)_{B,1}-\mathbf{V}_{B,N_B}+\mathbf{V}_{B,1} \tag{2.41}$$

$$g_3=\frac{1}{2}\left[\left(\mathbf{V}_{B,1}\right)^2-\left(\mathbf{V}_{B,N_B}\right)^2\right] \tag{2.42}$$

where $\boldsymbol{\tau}$ is the unit tangent vector on the body contour defined in the clockwise direction and d_j is the curvilinear distance between the midpoints of the $\left(j,j+1\right)$ panels.

2.3.1 Solution of the Hydrodynamic Problem

As it was previously mentioned, the solution of the hydrodynamics problem can be achieved using various approaches. To begin, we focus on the role that will be assigned to the BIE presented in (2.26). The BIE can be used as:

1. part of a system of equations containing information about the unknown boundary fields $\Phi_B(x,y;t)$ on the body boundary. Using the pressure-type Kutta condition, as presented in Section 2.2.1, or the Morino condition we construct the complete system of equations, with the boundary fields $\Phi_B(x,y;t)$ and μ_{W1} as unknowns.
2. a constraint to the dynamical system evolution equations. The latter is constructed using the pressure-type Kutta condition, while the DtN operator acts as a constraint. This operator is constructed using the discretized BIE. The dynamic variable in this case is μ_{W1} denoting dipole intensity in the vicinity of the trailing wake.

2.3.1.1 First approach - System of equations

Using the BIE along with the Morino condition we can construct a linear system of equations for the unknown boundary fields $\Phi_B(x,y;t)$ and μ_{W1} at the vicinity of the trailing edge, which can be solved at each time step of the simulation, for more details refer to Filippas (2013).

Instead of using Morino condition in this section we present a more accurate approach to the problem solution using pressure-type Kutta. A finite difference method (FDM) is used for the temporal and spatial discretization of the pressure-type Kutta condition in order to form a system of nonlinear equations along with the BIE relation.

The resulting system of equations can be solved numerically after the appropriate discretization at each time step of the simulation.

Particularly, a backward finite difference scheme in time combined with forward and backward differences in space has been used for the discretization of the pressure-type Kutta condition in the set of equations (2.37)-(2.42) as follows,

$$\left(\frac{(\mathbf{g}_1-\mathbf{g}_2)\cdot\mathbf{c}_1}{2d_1}-\frac{3}{2\Delta t}\right)\Phi_{B1}-\frac{(\mathbf{g}_1-\mathbf{g}_2)\cdot\mathbf{c}_1}{2d_1}\Phi_{B2}-\frac{(\mathbf{g}_1+\mathbf{g}_2)\cdot\mathbf{c}_{N_B}}{2d_{N_B}}\Phi_{BN_B-1}+\left(\frac{(\mathbf{g}_1+\mathbf{g}_2)\cdot\mathbf{c}_{N_B}}{2d_{N_B}}+\frac{3}{2\Delta t}\right)\Phi_{BN_B}$$
$$+\frac{1}{2}\left(\frac{\mathbf{c}_{N_B}}{d_{N_B}}\Phi_{BN_B}-\frac{\mathbf{c}_{N_B}}{d_{N_B}}\Phi_{BN_B-1}+\frac{\mathbf{c}_1}{d_1}\Phi_{B2}-\frac{\mathbf{c}_1}{d_1}\Phi_{B1}\right)\left(\frac{\mathbf{c}_{N_B}}{d_{N_B}}\Phi_{BN_B}-\frac{\mathbf{c}_{N_B}}{d_{N_B}}\Phi_{BN_B-1}-\frac{\mathbf{c}_1}{d_1}\Phi_{B2}+\frac{\mathbf{c}_1}{d_1}\Phi_{B1}\right)$$
$$=g_0-\frac{\mathbf{g}_1\mathbf{g}_2}{2}-g_3 \tag{2.43}$$

The linearized form of the above equation is,

$$\left(\frac{(\mathbf{g}_1-\mathbf{g}_2)\cdot\mathbf{c}_1}{2d_1}-\frac{3}{2\Delta t}\right)\Phi_{B1}-\frac{(\mathbf{g}_1-\mathbf{g}_2)\cdot\mathbf{c}_1}{2d_1}\Phi_{B2}-\frac{(\mathbf{g}_1+\mathbf{g}_2)\cdot\mathbf{c}_{N_B}}{2d_{N_B}}\Phi_{BN_B-1}+\left(\frac{(\mathbf{g}_1+\mathbf{g}_2)\cdot\mathbf{c}_{N_B}}{2d_{N_B}}+\frac{3}{2\Delta t}\right)\Phi_{BN_B}$$
$$=g_0-\frac{\mathbf{g}_1\mathbf{g}_2}{2}-g_3 \tag{2.44}$$

where $c_k=\left(\tau_{x,Bk}\mathbf{i}+\tau_{y,Bk}\mathbf{j}\right)\quad k=1,N_B$. In the relations above, $\boldsymbol{\tau}$ in the above relations refers to the unit tangent vector on the body contour defined in the clockwise direction and d_j is the curvilinear distance between the midpoints of the $(j,j+1)$ panels. Also,

$$\mathbf{g}_0=\frac{4(\Phi_{\mathrm{BN_B},t-\Delta t}-\Phi_{\mathrm{B1},t-\Delta t})-(\Phi_{\mathrm{BN_B},t-2\Delta t}-\Phi_{\mathrm{B1},t-2\Delta t})}{2\Delta t} \tag{2.45}$$

$$\mathbf{g}_1=\left(b\cdot\mathbf{n}\right)_{B,N_B}+\left(b\cdot\mathbf{n}\right)_{B,1}-\mathbf{V}_{B,N_B}-\mathbf{V}_{B,1} \tag{2.46}$$

$$\mathbf{g}_2=\left(b\cdot\mathbf{n}\right)_{B,N_B}-\left(b\cdot\mathbf{n}\right)_{B,1}-\mathbf{V}_{B,N_B}+\mathbf{V}_{B,1} \tag{2.47}$$

$$g_3=\frac{1}{2}\left[\left(\mathbf{V}_{B,1}\right)^2-\left(\mathbf{V}_{B,N_B}\right)^2\right] \tag{2.48}$$

Returning now to the discretized form of the boundary integral (2.31), we derive the following expression by re-arranging terms, so that for (x_i,y_i) , $i=1,...,N_B$:

$$\sum_{j=1}^{N_B}\left(\frac{\delta_{ij}}{2}+B_{ij}\right)\Phi_{Bj}+\left(B_{i1}\right)\mu_{W1}=\sum_{j=1}^{N_B}\left(A_{ij}\right)\underbrace{\left[\boldsymbol{V}_B\cdot\boldsymbol{n}_B\right]_j}_{b_j}+\sum_{j=2}^{N_F}\left(-B_{ij}\right)\mu_{Wj} \tag{2.49}$$

In this form all the quantities in the rhs are known from the prescribed kinematics of the foil and the history of circulation of the foil, that has been evaluated at previous time steps.

Equations (2.43)-(2.48) & (2.49) form a set of N_B+1 equations which can be solved for the unknown values of Φ_{Bi} and μ_{w1} at each time step. Moreover, this set of equations can be written in a more compact form,

$$\mathbf{f}\left(\mathbf{x}\right)=0 \tag{2.50}$$

$$f_i\left(\mathbf{x}\right)=\sum_{j=1}^{N_B}\left(\frac{\delta_{ij}}{2}+B_{ij}\right)\Phi_{Bj}+\left(B_{i1}\right)\mu_{W1}-\underbrace{\left\{\sum_{j=1}^{N_B}\left(A_{ij}\right)\underbrace{\left[\boldsymbol{V}_B\cdot\boldsymbol{n}_B\right]_j}_{b_j}+\sum_{j=2}^{N_F}\left(-B_{ij}\right)\mu_{Wj}\right\}}_{G_i} \tag{2.51}$$

$$\mathbf{x}=\left[\Phi_{\mathrm{B1}}\ \ldots\ \Phi_{\mathrm{BN_B}}\ \mu_{w1}\right]^T \tag{2.52}$$

and for the non-linear Pressure-type Kutta condition

$$\begin{aligned}
f_{N_B+1}\left(\mathbf{x}\right)=&\left(\frac{\left(\mathbf{g}_1-\mathbf{g}_2\right)\cdot\mathbf{c}_1}{2d_1}-\frac{3}{2\Delta t}\right)\Phi_{B1}-\frac{\left(\mathbf{g}_1-\mathbf{g}_2\right)\cdot\mathbf{c}_1}{2d_1}\Phi_{B2}\\
&-\frac{\left(\mathbf{g}_1+\mathbf{g}_2\right)\cdot\mathbf{c}_{N_B}}{2d_{N_B}}\Phi_{BN_B-1}+\left(\frac{\left(\mathbf{g}_1+\mathbf{g}_2\right)\cdot\mathbf{c}_{N_B}}{2d_{N_B}}+\frac{3}{2\Delta t}\right)\Phi_{BN_B}\\
&+\frac{1}{2}\left(\frac{\mathbf{c}_{N_B}}{d_{N_B}}\Phi_{BN_B}-\frac{\mathbf{c}_{N_B}}{d_{N_B}}\Phi_{BN_B-1}+\frac{\mathbf{c}_1}{d_1}\Phi_{B2}-\frac{\mathbf{c}_1}{d_1}\Phi_{B1}\right)\left(\frac{\mathbf{c}_{N_B}}{d_{N_B}}\Phi_{BN_B}-\frac{\mathbf{c}_{N_B}}{d_{N_B}}\Phi_{BN_B-1}-\frac{\mathbf{c}_1}{d_1}\Phi_{B2}+\frac{\mathbf{c}_1}{d_1}\Phi_{B1}\right)\\
&\underbrace{-g_0-\frac{\mathbf{g}_1\mathbf{g}_2}{2}-g_3}_{G_{N_B+1}}
\end{aligned} \tag{2.53}$$

or in linearized form

$$\begin{aligned}
f_{N_B+1}\left(\mathbf{x}\right)=&\left(\frac{\left(\mathbf{g}_1-\mathbf{g}_2\right)\cdot\mathbf{c}_1}{2d_1}-\frac{3}{2\Delta t}\right)\Phi_{B1}-\frac{\left(\mathbf{g}_1-\mathbf{g}_2\right)\cdot\mathbf{c}_1}{2d_1}\Phi_{B2}\\
&-\frac{\left(\mathbf{g}_1+\mathbf{g}_2\right)\cdot\mathbf{c}_{N_B}}{2d_{N_B}}\Phi_{BN_B-1}+\left(\frac{\left(\mathbf{g}_1+\mathbf{g}_2\right)\cdot\mathbf{c}_{N_B}}{2d_{N_B}}+\frac{3}{2\Delta t}\right)\Phi_{BN_B}-\underbrace{g_0-\frac{\mathbf{g}_1\mathbf{g}_2}{2}-g_3}_{G_{N_B+1}}
\end{aligned} \tag{2.54}$$

Equations (2.50)-(2.52) and (2.54) consist of a linear system of equations that can be solved explicitly for the unknown values of $\mathbf{x}$. That could be, however, a first step for the solution of the nonlinear system of equations (2.45)-(2.47) and (2.53) using a General Iterative Method.

In this work, for the present multivariate problem a Newton Raphson method is implemented at each time step as follows

$$\mathbf{x}_{n+1}=\mathbf{x}_n-\mathbf{J}(\mathbf{x}_n)^{-1}\mathbf{f}(\mathbf{x}_n) \tag{2.55}$$

where $\mathbf{J}(\mathbf{x}_n)^{-1}$ denotes the inverse of the system's Jacobian, which can be analytically calculated for the present formulation. To summarize the Jacobian is

$$\mathbf{J}(\mathbf{x})=\begin{bmatrix} \frac{\partial f_1(\mathbf{x})}{\partial \Phi_{\mathrm{B}1}} & \cdots & \frac{\partial f_1(\mathbf{x})}{\partial \Phi_{\mathrm{B}N_B}} & \frac{\partial f_1(\mathbf{x})}{\partial \mu_{w1}} \\ \vdots & \ddots & \vdots & \vdots \\ \frac{\partial f_{N_B}(\mathbf{x})}{\partial \Phi_{\mathrm{B}1}} & \cdots & \frac{\partial f_{N_B}(\mathbf{x})}{\partial \Phi_{\mathrm{B}N_B}} & \frac{\partial f_{N_B}(\mathbf{x})}{\partial \mu_{w1}} \\ \frac{\partial f_{N_B+1}(\mathbf{x})}{\partial \Phi_{\mathrm{B}1}} & \cdots & \frac{\partial f_{N_B+1}(\mathbf{x})}{\partial \Phi_{\mathrm{B}N_B}} & \frac{\partial f_{N_B+1}(\mathbf{x})}{\partial \mu_{w1}} \end{bmatrix} \tag{2.56}$$

$$\frac{\partial f_i(\mathbf{x})}{\partial \Phi_{\mathrm{B}k}}=\frac{\delta_{ik}}{2}+B_{ik}\ ,\ i=1,...,N_B\ ,\ k=1,...,N_B \tag{2.57}$$

$$\frac{\partial f_i(\mathbf{x})}{\partial \mu_{W1}}=B_{i1}\ ,\ i=1,...,N_B \tag{2.58}$$

$$\begin{aligned}\frac{\partial f_{N_B+1}(\mathbf{x})}{\partial \Phi_{\mathrm{B}k}}&=\mathrm{sgn}_{1,k}\frac{|\mathbf{c}_k|^2}{(d_k)^2}\Phi_{Bk}\\ &+\mathrm{sgn}_{2,k}\frac{(\mathbf{g}_1+\mathrm{sgn}_{1,k}\cdot\mathbf{g}_2)\cdot\mathbf{c}_k+\mathbf{a}_{Bk}(\{\Phi_l\},l\neq k)\cdot\mathbf{c}_k+\mathrm{sgn}_{1,k}\cdot\mathbf{b}_{Bk}(\{\Phi_l\},l\neq k)\cdot\mathbf{c}_k}{2d_k}\\ &+q_{Bk}(\Delta t),\ k=1,2,N_B-1,N_B\end{aligned} \tag{2.59}$$

with the following functions,

$$d_k=\begin{cases} d_1 & k=1,2 \\ d_{N_B} & k=N_B-1,N_B \end{cases} \tag{2.60}$$

$$\mathbf{c}_k=\begin{cases} \mathbf{c}_1 & k=1,2 \\ \mathbf{c}_{N_B} & k=N_B-1,N_B \end{cases} \tag{2.61}$$

$$\mathrm{sgn}_{1,k}=\begin{cases} -1 & k=1,2 \\ +1 & k=N_B-1,N_B \end{cases} \tag{2.62}$$

$$\mathrm{sgn}_{2,k}=\begin{cases} +1 & k=1,N_B \\ -1 & k=2,N_B-1 \end{cases} \tag{2.63}$$

$$q_{Bk}=\begin{cases} -\frac{3}{2\Delta t} & k=1 \\ +\frac{3}{2\Delta t} & k=N_B \\ 0 & k=2,N_B-1 \end{cases} \tag{2.64}$$

$$\frac{\partial f_{N_B+1}(\mathbf{x})}{\partial \Phi_{Bk}} = 0 \ , \ k = 3,..., N_B - 2 \tag{2.65}$$

$$\frac{\partial f_{N_B+1}(\mathbf{x})}{\partial \mu_{W1}} = 0 \tag{2.66}$$

Finally, for the evaluation of Φ in the domain D at every time step for each $(x_i, y_i) \in D$ the following expression can be used

$$\Phi_i = \sum_{j=1}^{N_B}\left(A_{ij}\right) b_j + \sum_{j=1}^{N_B}\left(-B_{ij}\right)\Phi_{Bj} + \sum_{j=1}^{N_F}\left(-B_{ij}\right)\mu_{Wj} \tag{2.67}$$

2.3.1.2 Second approach - First Order Initial Value Problem (IVP)

The pressure-type Kutta condition in equation (2.20) contains a partial time derivative of the unknown potential. Therefore, it can be used after discretization as the dynamical system evolution equation with the DtN operator acting as a constraint and μ_{W1} as the dynamic variable.

Particularly, we use the Leibniz rule for equation (2.37)-(2.42) and the DtN operator, see equation (2.35), in order to express the values of the potential in the vicinity of the trailing edge that appear in the discretized form of the pressure-type Kutta condition, in terms of the dynamic variable μ_{W1}. In this way we obtain the following nonlinear first order differential equation,

$$\frac{d\mu_{W1}}{dt} = \left[\mathscr{N}(\mu_{W1}) + \mathscr{L}(\mu_{W1}) - \frac{d(\ Z\ )}{dt}\mu_{W1} - \frac{d}{dt}(\ \mathbf{D}\cdot\mathbf{b} + \ P\ )\right]\cdot(\ Z\ )^{-1} \tag{2.68}$$

where $\mathbf{D} = \left[\!\left[\{D\}_{ij}\right]\!\right]_{i=1}^{i=N_B}$ denotes a vector $P = P_i{}_{i=1}^{i=N_B}$, $Z = Z_i{}_{i=1}^{i=N_B}$ scalar quantities. Notice that that Ψ symbolizes the difference of a function Ψ at the trailing edge. For more details see Filippas & Belibassakis (2014) and Filippas (2019).

Under the assumption of prescribed kinematics, $\mathbf{b}$ is known at each time step from the no-entrance boundary condition in equation (2.5). Also, $\mathbf{P}(\mu_W)$ in equation (2.36) or P in equation (2.68) contains information regarding the distribution of dipoles on the wake, known from the time history.

Especially for rigid body hydrodynamics the DtN operator needs to be evaluated only once, saving computational cost and thus time. However, in formulations where the

body boundary is deformable, this operator needs to be re-evaluated at each time step, making simulations of chord-wise flexible foils more computationally demanding.

Matrix $\mathbf{Z}$ contains at each time step information concerning the induction factors for a dipole singularity of unit strength at the panel element known as Kutta-strip. Also, since this differential equation contains both linear and non-linear terms, an appropriate numerical scheme for the time integration need to be implemented.

To accomplish that, the initial value problem (IVP) with respect to the dynamic variable $\mathbf{U} = \mu_{W1}$ is presented below in a more compact notation

$$\frac{d\mathbf{U}}{dt} = \mathbf{f}(\mathbf{U}),\ \mathbf{U}(t_o) = \mathbf{U}_o \tag{2.69}$$

$$\mathbf{f}(\mathbf{U}) = [\frac{-1}{Z}\frac{d(\ Z\ )}{dt}]\cdot\mathbf{U} + [\frac{-1}{Z}\frac{d(\ \mathbf{D}\cdot\mathbf{b} + P\ )}{dt}] + [\frac{\mathscr{N}(\mathbf{U}) + \mathscr{L}(\mathbf{U})}{Z}] \tag{2.70}$$

where $\mathbf{f}(\mathbf{U})$ denotes a vector function.

As far as numerical solutions for first-order IVPs are concerned, we could use either explicit or implicit methods from the two main categories (i) Linear multistep methods and (ii) Runge-Kutta methods.

In the present study a higher-order Adams-Bashford-Moulton (A.B.M.) scheme is implemented. This forth order method falls into the linear multistep category, requires two evaluations of the vector function $\mathbf{f}$ at each time step and has error estimate of order (Δt^5) providing the required accuracy stability and efficiency, see Longuet-Higgins & Cokelet (1975) as well as Filippas & Belibassakis (2014).

The time derivative terms $d(\ Z\ )/dt$, $d(\ \mathbf{D}\cdot\mathbf{b} + P\ )/dt$ in equation (2.68) can be approximated numerically with a finite difference scheme. To proceed, with $\mathbf{U}(t)$ known at time step t, the corrector step is the following,

$$\mathbf{U}(t+\Delta t) = \mathbf{U}(t) + \frac{\Delta t}{24}[9\mathbf{f}_{pre}(t+\Delta t) + 19\mathbf{f}(t) - 5\mathbf{f}(t-\Delta t) + \mathbf{f}(t-2\Delta t)] \tag{2.71}$$

with predictor step

$$\mathbf{f}_{pre}(t+\Delta t) = \mathbf{f}_{t+\Delta t}\left(\mathbf{U}_{pre}(t+\Delta t)\right) \tag{2.72}$$

$$\mathbf{U}_{pre}(t+\Delta t) = \mathbf{U}(t) + \frac{\Delta t}{24}[55\mathbf{f}(t) - 59\mathbf{f}(t-\Delta t) + 37\mathbf{f}(t-2\Delta t) - 9\mathbf{f}(t-3\Delta t)] \tag{2.73}$$

After the solution has been obtained, at each time step, the DtN can then be used for the calculation of the potential on the body-boundary. Subsequently information concerning the potential or the velocity field on the domain can be obtained from the

boundary data. Finally, for the evaluation of Φ in the domain D at every time step for each $(x_i, y_i) \in D$ the following expression can be used,

$$\Phi_i = \sum_{j=1}^{N_B} \left(A_{ij} \right) b_j + \sum_{j=1}^{N_B} \left(-B_{ij} \right) \Phi_{Bj} + \sum_{j=1}^{N_F} \left(-B_{ij} \right) \mu_{Wj} \tag{2.74}$$

2.4 Numerical Results

The BEM-solver that was initially developed by Filippas & Belibassakis (2014), Filippas (2019) has been extended, within the framework of this diploma thesis, to treat the unsteady lifting flow problem of flapping foils with prescribed deformations. The initial 2-D version of the code was written in Matlab, a multi-paradigm numerical computing environment. In order to improve performance we

- used vectorization techniques, offered in the recent versions of Matlab, in functions responsible for the construction of the DtN operator
- added object-oriented features and data structures to make coding less error-prone and user friendly

2.4.1 Flapping-Foil Propulsion Parameters

In the present study the unsteady flapping motion of the foil is described by three degrees of freedom (i) the forward motion $s(t)$, (ii) the heaving $h(t)$ and (iii) pitching motion $\theta(t)$ with respect to the inertial reference frame, see Figure 2.4. For simplicity, the oscillatory motions heaving and pitching motions are assumed to be harmonic. These motions are enforced on the pivot point located along chord length c, smooth transition between initial resting state and unsteady motion is accomplished with a time filter function $F(t) = 1 - \exp(-f_o t^2)$ where $f_o \in \Re^+$.Therefore we have,

$$s(t) = -F(t)Ut \tag{2.75}$$

$$h(t) = F(t)[h_a \cos(2\pi ft)] \tag{2.76}$$

$$\alpha(t) = F(t)[\alpha_o + \alpha_\alpha \cos(2\pi ft + \varphi)] \tag{2.77}$$

where U is the forward velocity, h_a the heaving amplitude, α_α the pitching amplitude, f the flapping frequency, φ the phase difference between the motions and α_o the initial pitching angle.

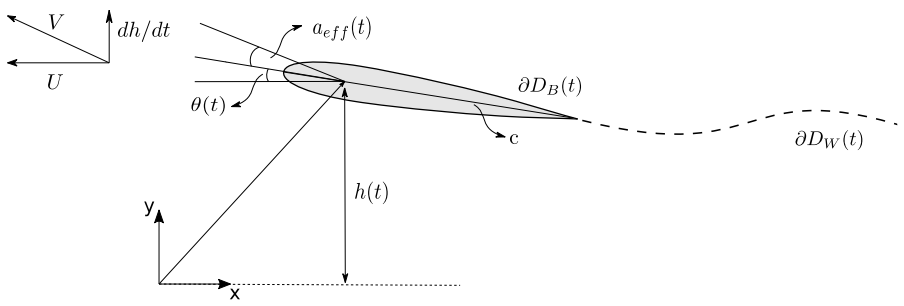

Figure 2.4 Flapping-foil propulsion parameters and kinematic characteristics

The maximum angle of attack $a_{\max}$ is another very important motion parameter, since it is connected with the initiation of the leading edge separation and the dynamic stall effects. The instantaneous angle of attack (effective angle of attack) for a stationary fluid in an un-bounded domain can be evaluated

$$a(t) = \tan^{-1}\left(\frac{dh/dt}{ds/dt}\right) - \theta(t) \tag{2.78}$$

This angle of attack is defined by the total velocity that an observer fixed at the pivot point along the foil's chord length experiences, as a result of the forward motion and the heaving velocity. For the special case of (2.75)-(2.77) equation (2.78) is,

$$a(t) = \tan^{-1}\left(\frac{\omega h_o \sin(\omega t)}{U}\right) + \theta(t)\cos(\omega t + \varphi) \tag{2.79}$$

The main non-dimensional parameters for modelling the flapping motion, as discussed in Shyy (2013), are the following:

- Reynolds number is defined as the ratio between inertial and viscous forces. For a flapping motion typically reference length L_{ref} refers to an averaged chord length in span-wise direction, velocity U_{ref} is the free-stream velocity in forward movement and v the kinematic viscosity of the fluid.

$$\mathrm{Re} = \frac{U_{ref} L_{ref}}{v} = \frac{U c_m}{v} \tag{2.80}$$

- Strouhal number characterizes the behaviour of oscillating flow mechanisms, vortex dynamics and shredding behaviours. Particularly for natural flyers and swimmers at cruising conditions higher values of propulsive efficiency where encountered in a narrow region of $0.2 < \mathrm{St} < 0.4$, see Taylor et al. (2003). If

$$St = \frac{f \cdot L_{ref}}{U_{ref}} = \frac{2h_o f}{U_{ref}} \tag{2.81}$$

where $2h_o$ is the characteristic trailing edge amplitude.

- Reduced frequency is also a parameters that characterises the unsteadiness of the flapping motion.

$$k = \frac{2\pi f \cdot L_{ref}}{2U_{ref}} = \frac{c_m}{2h_a} \tag{2.82}$$

- Advance ratio which can be defined as a function of Strouhal number is introduced in 2D forward flight as it is shown below.

$$J = \frac{U_{ref}}{2\pi f \cdot h_a} = \frac{1}{\pi St} \tag{2.83}$$

2.4.2 Calculation of Pressure and Forces

It was previously mentioned that the present model could serve as a useful tool for the calculation pressure distribution along chord-length for hydrofoils of various forms. In this section we derive the formulas used in the calculation of pressure distribution and other integrated quantities that are important when the overall performance of flapping foil inspired propulsion is assessed.

The pressure difference coefficient[1] on the thin hydrofoil for a velocity, that is characteristic for the foil motion (e.g. the forward velocity of flapping foil thruster) is defined as

$$\Delta C_P = \frac{p_l - p_u}{\frac{1}{2}\rho U^2} \tag{2.84}$$

In order for the forces acting on the hydrofoil to be calculated the evaluation of the pressure on the body boundary is essential. In the present study an unsteady version of Bernoulli's equation derived from Euler's equation was employed, see e.g. Filippas (2013),

$$\frac{p}{\rho} = -\frac{\partial \Phi}{\partial t} - \frac{1}{2}\left(\nabla \Phi\right)^2 \tag{2.85}$$

[1] In Chapter 4, were the fluid-structure interaction problem of chord-wise flexible foils is presented, the pressure distribution coefficient serves as the loading term in the RHS of the thin plate equation for the structural response of the deformable foil.

where ϱ is the fluid density, $p(x,y;t)$ the perturbation pressure at point $(x,y;t)$ and $\frac{\partial \Phi}{\partial t}$ denotes the total velocity time rate with respect to a fixed observer at the inertial reference frame.

The formulation of the BIE in equation (2.26) refers to quantities of the trace Φ^* on the boundary but the corresponding rate of change denoted by $\frac{d\Phi^*}{dt}$ with respect to the body-fixed reference frame $Ox'y'$ can also be calculated (Section 2.2). A special treatment that results into the expression of the approximate Bernoulli's theorem based on boundary data is found in Politis (2011). The final form of the approximate Bernoulli's theorem as required for the calculation of perturbation pressure distribution on the body boundary is the following

$$\frac{p_{\mathrm{B}}}{\rho} = -\frac{d\Phi_{\mathrm{B}}^*}{dt} + \nabla\Phi_{\mathrm{B}}^* \cdot \left(\mathbf{V}_B\right) - \frac{1}{2}\left(\nabla\Phi_{\mathrm{B}}^*\right)^2 + \frac{1}{2}\underbrace{\left[\mathbf{n}_{\mathrm{B}} \cdot \mathbf{V}_B\right]}_{b}^2 \tag{2.86}$$

Finally for the non-dimensional pressure coefficient $C_p = p / 0.5\rho U^2$ in conjunction with (2.9) the following is obtained,

$$C_P = \frac{2}{U^2}\left\{-\frac{d\Phi_{\mathrm{B}}^*}{dt} + \nabla\Phi_{\mathrm{B}}^* \cdot \left(\mathbf{V}_B\right) - \frac{1}{2}\left(\nabla\Phi_{\mathrm{B}}^*\right)^2 + \frac{1}{2}b^2\right\} \tag{2.87}$$

The instantaneous lift coefficient

$$C_L = \frac{L(t)}{\frac{1}{2}\rho U^2 c} = \frac{1}{c}\int_{\partial D_B} (C_P \cdot n_y) ds \tag{2.88}$$

The instantaneous thrust coefficient

$$C_T = \frac{T(t)}{\frac{1}{2}\rho U^2 c} = -\frac{1}{c}\int_{\partial D_B} (C_P \cdot n_x) ds \tag{2.89}$$

The instantaneous moment coefficient

$$C_M = \frac{M(t)}{\frac{1}{2}\rho U^2 c^2} = \frac{1}{c^2}\int_{\partial D_B} (C_P \cdot \mathbf{n}) \cdot \mathbf{r}(s \mid t) ds \tag{2.90}$$

where $\mathbf{r}(s;t)$ is the reference vector pointing from pivot point to surface point.

The moment coefficient is calculated with the formula presented above with respect to the centre of rotation and the negative values correspond to drag. Since the foil is passively submitted to flapping motions, consisting of heaving h and pitching θ, we

can define the instantaneous propulsive efficiency, as the ratio of the cycle-averaged power to the incoming energy flux,

$$\eta = \frac{P_{out}}{P_{in}} = \frac{\mathrm{T}(t)\cdot U}{P_{in}} \tag{2.91}$$

where $P_{in}(t) = L(t)\dot{h} + M(t)\dot{\theta}$ denotes the power input to the foil. The cycle-averaged input power coefficient can also be defined as,

$$C_{op} = \frac{P_{in}}{\frac{1}{2}\rho U^3 c} \tag{2.92}$$

For the case of periodic oscillatory motions, we are interested in calculating the the mean values of the thrust and input power coefficient per cycle, as well as the amplitudes of the lift and moment coefficient. For the mean thrust and input power coefficient we have respectively,

$$\overline{C_T} = \frac{1}{T}\int_0^T C_T(t)dt \tag{2.93}$$

$$\overline{C_{op}} = \frac{1}{T}\int_0^T C_{op}(t)dt \tag{2.94}$$

whereas for the amplitudes of the lift and moment coefficients the following formulas will be used

$$\overset{o}{C}_L = \frac{2}{T}\int_0^T C_L(t)\cos(\frac{2\pi}{T}t)dt \tag{2.95}$$

$$\overset{o}{C}_M = \frac{2}{T}\int_0^T C_M(t)\cos(\frac{2\pi}{T}t)dt \tag{2.96}$$

The pressure distribution along the body-boundary can be evaluated from the approximate Bernoulli's theorem in equation (2.86). Assuming that pressure remains constant at each panel the following non-dimensional instantaneous coefficients can be calculated as follows

$$C_L(t) = \sum_{j=1}^{N} C_P(x_i, y_i; t)\Delta y_i \tag{2.97}$$

$$C_T(t) = -\sum_{j=1}^{N} C_P(x_i, y_i; t)\Delta x_i \tag{2.98}$$

$$C_M(t) = \sum_{j=1}^{N} C_P(x_i, y_i; t)\left[\Delta x_i\left(x_i - x_{ref}\right) + \Delta y_i\left(y_i - y_{ref}\right)\right] \tag{2.99}$$

where $\Delta x_i = x_{i,2} - x_{i,1}$, $\Delta y_i = y_{i,2} - y_{i,1}$, are respectively the x and y-axis projections of the panel-i on the body-fixed reference frame, while $\left(x_{ref}, y_{ref}\right)$ refers to the center of rotation located along chord-length.

2.4.3 Numerical Study

This section begins with a discussion about the stability and convergence of the numerical schemes introduced in Section 2.3.1. In both approaches, where the pressure-type Kutta condition is enforced at the vicinity of the trailing edge we expect the pressure difference at the trailing edge to be closer to zero as time discretization becomes more refined. Therefore, the pressure difference at the trailing edge is monitored during simulations as a measure of numerical instability. More particularly, if (1) the pressure difference at the trailing edge starts to gradually increase at some point during the simulation or (2) the pressure difference changes signs between consequent time steps, numerical instabilities have occurred. In most cases, with a proper selection of space and time discretization parameters this can be avoided.

Extensive numerical investigation of both approaches has been performed for cases of flapping motion. It has been found that the convergence is characterized by an optimum relation between the size of the panels neighboring to the trailing edge of the body Δs_B and those that represent the nearby wake Δs_W.

Systematic studies concerning the first approach (see Section 2.3.1.1) have shown that for a range of parameters consisting of $0.2 < Str < 0.4$ and $10 < \theta_o < 50$, the optimal ratio varies in the interval $2 < \Delta s_W / \Delta s_B < 3.25$ with greater values corresponding to lower Strouhal numbers, see also Filippas & Belibassakis (2014).

We present as an example in Figure 2.5 a color plot of the error $\left|(C_T - C_T^{ref}) / C_T^{ref}\right|$ associated with the thrust coefficient $C_T = -F_X / \rho U^2 h_o$, as a function of the number of panels on the body N_b and the time-step expressed as a portion of the period $\Delta t / T(\%)$, in the case of flapping NACA 0012 hydrofoil in an unbounded domain. In this case, the Strouhal number is $Str = \omega h_o / \pi U = 0.4$, the vertical (heaving) amplitude $h_o / c = 1$ and the rotational (pitching) amplitude $\theta_o = 45^o$. The thrust coefficient error is calculated with respect to the value C_T^{ref} as obtained by the present method, based on the finest discretization in both space and time ($\mathrm{N_B} = 500$, $\mathrm{dt} = 0.00125\mathrm{T}$). In the same figure the curves corresponding to different values of $\Delta s_W / \Delta s_B$ are shown using

solid lines. We clearly observe that an optimal ratio exists, which in the examined case is $\Delta s_W / \Delta s_B = 2.4$.

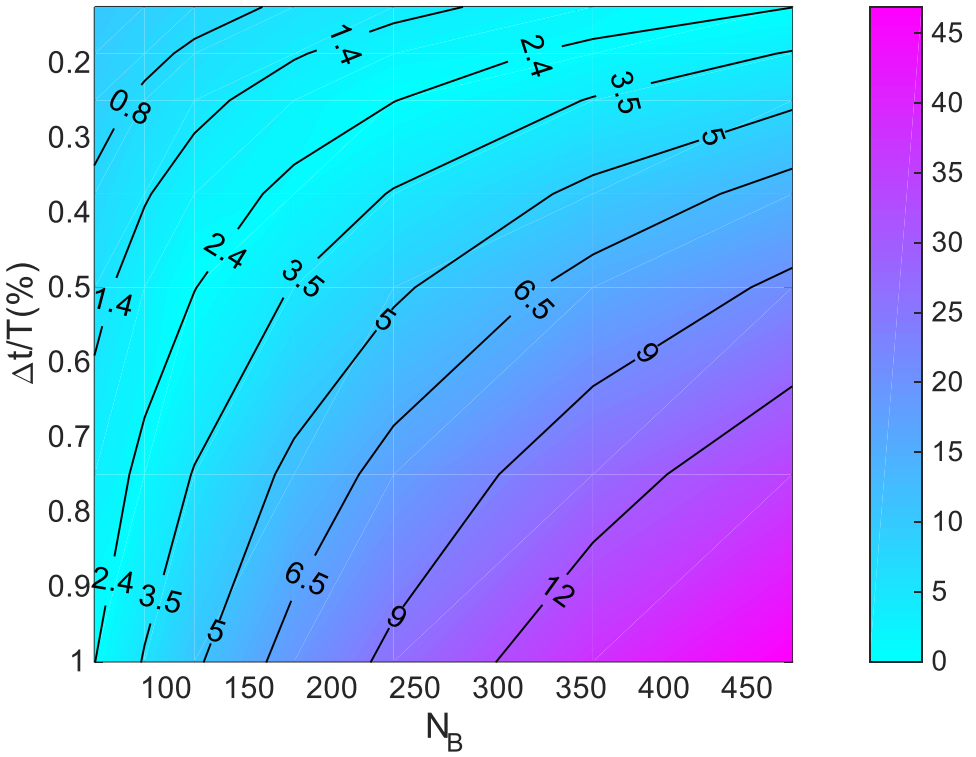

Figure 2.5 Convergence of thrust coefficient C_T (Section 2.3.1.1) as a function of the number of body panels N_B and the time-step $\Delta t / T(\%)$, for NACA0012 hydrofoil in flapping motion. The error of thrust coefficient (%) is shown by using color scale. Contour lines indicate the ratio $\Delta s_W / \Delta s_B$ of the length of panels in the vicinity of the trailing edge, from Filippas & Belibassakis (2014).

Regarding the second approach (see Section 2.3.1.2) results show that for the same range of parameters consisting of $0.2 < Str < 0.4$ and $10 < \theta_o < 50$, the optimal ratio varies in the interval $0.8 < \Delta s_W / \Delta s_B < 2$ with greater values corresponding to lower Strouhal numbers. We present in Figure 8 the color plot of the error $\left|(C_T - C_T^{ref}) / C_T^{ref}\right|$ associated with the thrust coefficient $C_T = -F_X / \rho U^2 h_o$, as a function of the number of panels on the body N_b and the time-step expressed as a portion of the period $\Delta t / T(\%)$, for the study case discussed above.

Since this approach is based on a higher-order Adams-Bashford-Moulton (A.B.M.) scheme that falls into the linear multistep category, simulations with a coarse discretization in time and a fine mesh is space ($N_B = 500$, $dt = 0.01T$) leads to numerical instabilities. The pressure-type Kutta condition is satisfied with increased precision only for fine discretization. Therefore, the results presented in Figure 8

correspond to a subset of the tested combinations of space and time discretization parameters, as presented in Figure 2.6.

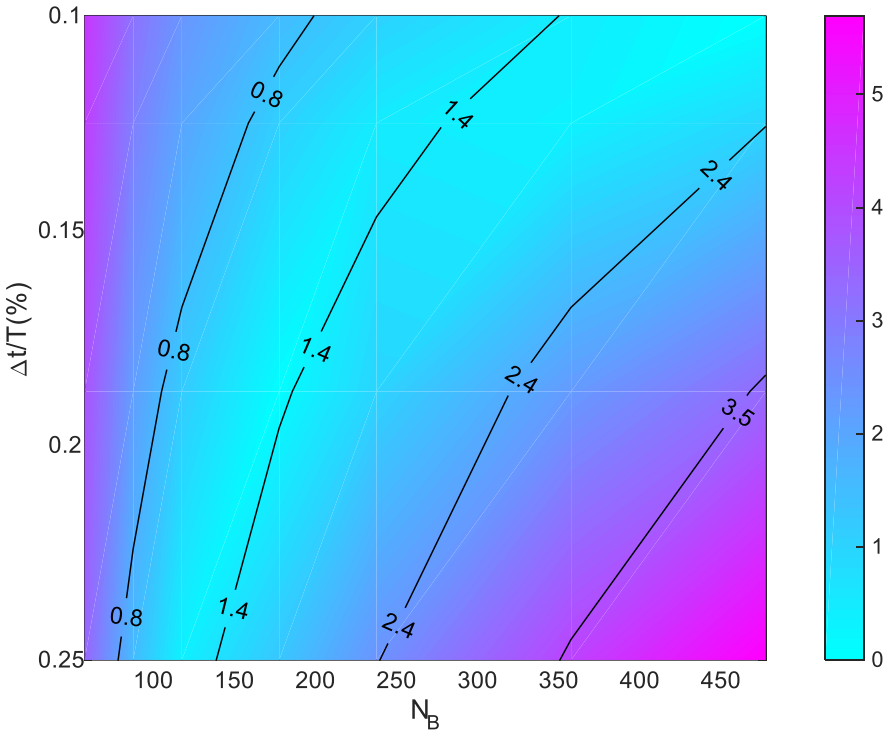

Figure 2.6 Convergence of thrust coefficient C_T (Section 2.3.1.2) as a function of the number of body panels N_B and the time-step $\Delta t/T(\%)$, for NACA0012 hydrofoil in flapping motion. The error of thrust coefficient (%) is shown by using color scale. Contour lines indicate the ratio $\Delta s_W / \Delta s_B$ of the length of panels in the vicinity of the trailing edge.

2.4.4 Validation

Regarding the presented BEM for the hydrodynamic analysis of rigid flapping foils, extensive validation against experimental data as well as numerical calculations concerning the solver's performance over a range of motion parameters, can be found in the work of Filippas & Belibassakis (2014). However, for completeness in this section we compare the present method with the experimental data found in Schouveiler et al. (2005). It is noted here, that the numerical schemes presented in Sections 2.3.1.1 & 2.3.1.2 are in agreement for fine discretization. The experiment consisted of generating the propulsive force with a foil undergoing a harmonic flapping which is a combination of a heave translation and a pitch rotation, to study an aquatic propulsion system inspired from the *thunniform* swimming mode.

Systematic measurements of the fluid loading showed a remarkable peak of efficiency of more than 70% for optimal combinations of the parameters.

Simulations were performed for a NACA 0012 foil with the center of rotation positioned at $1/3c$ for motions characterized by $Str = 0.3,\ h_o / c = 0.75,\ \theta_o = 23.3^o$ and phase lag $\varphi = -90^o$.Results obtained for the instantaneous thrust and lift coefficients are compared against experimental data in Figure 2.7. Satisfactory agreement is observed with the experimental data regarding the amplitude and the phase lag of the integrated force coefficients. The small differences concerning the peak values of the thrust coefficient could be due to non-linear vortex-wake dynamics that are not modeled in the present work.

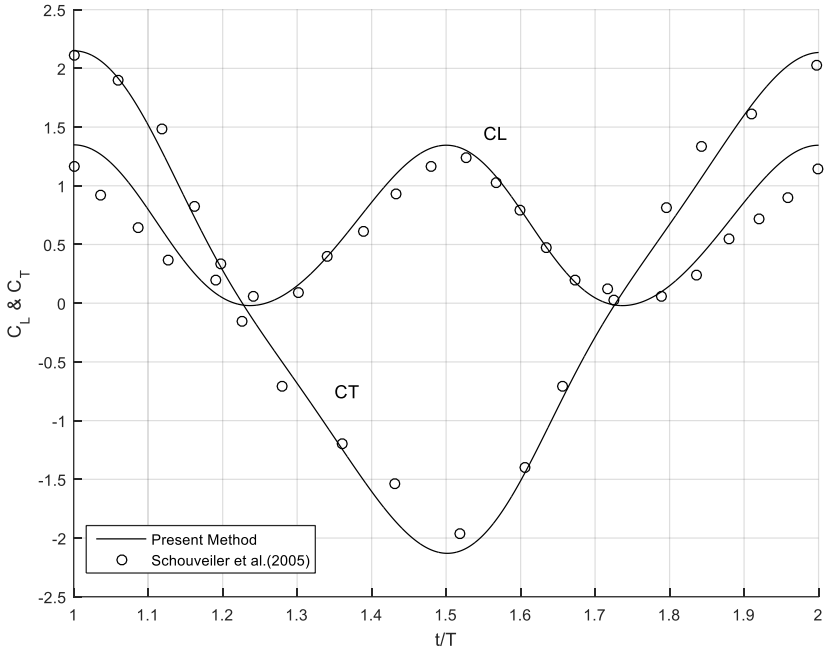

Figure 2.7 Thrust and Lift coefficients time history comparison between the present method with Schouveiler et al. (2005)

Chapter 3 - Structural Analysis of Thin Plate in Vacuo

In this Chapter we present a model for the dynamic structural analysis of the foil using the Classical Plate Theory (CPT) based on the Kirchhoff-Love hypothesis. Structurally , the foil, is modelled as a thin plate featuring flexural rigidity variation. The plate is subjected to cylindrical bending under the plane strain assumption. The studied structure is assumed to be perfectly elastic, homogeneous and isotropic. In this formulation, dimensionality reductions allows us to treat an 1-D problem. For the numerical solution of the partial differential equations modelling the transverse displacement of the plate, we follow an hp-FEM approach based on Hermite polynomials of 3^{rd} and 5^{th} order. Finite element formalism provides a very systematic manner of handling various boundary, allows the study of the convergence properties for the numerical scheme and can be implemented algorithmically with ease. The damped structural response of the foil is treated with the addition of proportional damping terms.

This Chapter begins with a brief introduction on Finite Element Methods and the characteristics of commercially available software. Then, the problem of cylindrical bending of thin elastic plates is introduced and appropriate boundary conditions are discussed. The equivalent weak formulation of the initial boundary value problem (IBVP) is derived by means of a Galerkin approximation method. Later, we present the discretization scheme with emphasis on the introduction of the employed Hermite finite elements, the deduction of the system of algebraic equations, the addition of appropriate proportional damping terms and the employed time integration scheme. In the last section of Chapter 3, the proposed numerical scheme is validated against analytical solutions, available in the literature, concerning (i) the free vibration analysis of a linearly double-tapered cantilever beam, (ii) the static solution of a non-prismatic cantilever beam under tip load forcing, and (iii) the dynamic analysis of a cantilever beam of constant thickness, under transverse dynamic tip loading. Furthermore, the capabilities of the developed FEM solver are illustrated through the investigation of a test case of particular interest to the present work and the coupling with the hydrodynamic field in particular, i.e. a structural response of a plate with flexural rigidity profile variation under dynamic distributed load resembling the time history of hydrodynamic pressure enforced on a rigid flapping foil with prescribed kinematics.

3.1 Brief introduction on Finite Element Method

The finite element method (FEM) is one of the most important developments in numerical analysis, a powerful and versatile tool for the solution of linear as well as nonlinear complex problems. This method was popularised in structural analysis in the 1950's with the pioneering work of J. Argyris, who systematically analysed complex structures with a large number of finite components. Over the years, the existence of a unified treatment of such discretised problems, led to the definition of the finite element process as a method of approximation to continuum problems with applications that spread in all fields of engineering, science and medicine, see Fung & Tong (2001) as well as Zienkiewicz et al. (2005) for a more details on the origin and fundamentals of the method.

The finite element method demands the division of the problem domain in sub-resgions, called *elements*, establishes approximate solutions in terms of unknown parameters in sub-regions and then deduces an approximate solution for the whole domain. In structural analysis, this procedure involves expressing the relations between the displacements and internal forces at the selected nodal points of individual structural components to form of a system of algebraic equations. The system of equations is then written most conveniently in matrix form, and the solution of these equations is obtained efficiently by high-speed computation. In truth, the concept of finite element method dates back to 1943 when Courant used a triangular mesh to solve a two-dimensional Laplace equation, or earlier when mathematicians formulated differential calculus with piece-wise smooth functions. However, the method did not found widespread applicability before the availability of high speed computers able to solve the produced large systems of algebraic equations and to handle the tedious input and the voluminous output.

Numerous finite-element computer programs are commercially available today for specific or general applications. To list a few, the most notable ones include NASTRAN, originally developed for NASA in the late 1960s under the United States government funding for the aerospace industry, ANSYS and ABAQUS. Equally important, if not more, in the finite element method is its *implementation.* The success of commercially available software lies largely in the development of efficient pre- and post-processors, and algorithms for solving large systems of equations.

The **pre-processor** enables users to describe efficiently, and in a relatively error-free manner, a complex problem in terms of its geometry, configuration, material properties, loading conditions, etc., through the input. Whereas, the **post-processor** handles the voluminous output making it easily understandable through interactive graphic, tables, charts, and summaries. The pre- and post-processors also enable users

to examine at ease any specific location of the domain or aspect of the solution prior to, during, or after the analysis. The need for **efficient solution algorithms for large systems** goes without saying, mainly because for professional applications finite element analysis (FEA) results often in systems with hundreds of thousands, even millions, degrees of freedom. Even with the advent of computers today, efficient algorithms make it possible to obtain the solutions, especially for nonlinear problems, at a reasonable cost and in a reasonable time.

3.2 Cylindrical Bending of Thin Elastic Plates

Generally, *plates* as structural elements have planform dimensions that are large compared to their thickness and are subjected to loads that cause bending deformations in addition to stretching. The plate theory presented in this section is valid for thin plates; with length-to-thickness ratio greater than 30 or slenderness ratios h/L smaller than 0.0333.

Let as consider a body-fixed reference frame and a Cartesian coordinate system (x, y, z) such that the xy-plane coincides with the geometric mid-plane of the plate and the remaining z-coordinate is taken positive upwards; i.e. right-hand rule. The dimensions of the rectangular plate under study are denoted as l_x, l_y, h along x, y and $z-$axis respectively with $l_y \gg l_x, h.$

The plate is symmetric in fabrication about the mid-surface with thickness variation described by a real function $h = h(x)$ and dimension l_x coincides with the chord length of the hydrofoil L. If the un-deformed mid-plane of the plate is denoted as a connected open Lipschitz subset Ω_o of $\mathbb{R}^2$ then the plate domain Ω is the following tensor product $\Omega = \Omega_o \times (-h(x)/2,\ h(x)/2)$.

The total displacements of a point along the (x, y, z) coordinates are denoted as (u, v, w) so that a material occupying position (x, y, z) in an un-deformed state shall moves to position $(x+u, y+v, z+w)$ after deformations have occurred. The displacement of a point on the mid-plane in the un-deformed state will be defined as (u_o, v_o, w_o). The displacement field is time dependent with $t \in (0, T),\ \ \mathrm{T} \in \mathbb{R}^+$ and therefore the domain in space/time for the dynamic problem is the product $\Omega \times (0, T).$

In classical plate theory (CPT) the Kirchhoff-Love hypothesis for the displacement field involves of the following three assumptions, see e.g. Reddy (2007). These assumptions are presented schematically in Figure 3.1.

- The **straightness assumption**; implying that straight lines that are perpendicular to the mid-surface remain straight after deformation.
- The **inextensibility condition**; under which the transverse normal does not experience elongation, the plate thickness does not change during deformations.
- The **normality assumption**; under which the transverse normal rotates but remains perpendicular to the mid-surface after deformation.

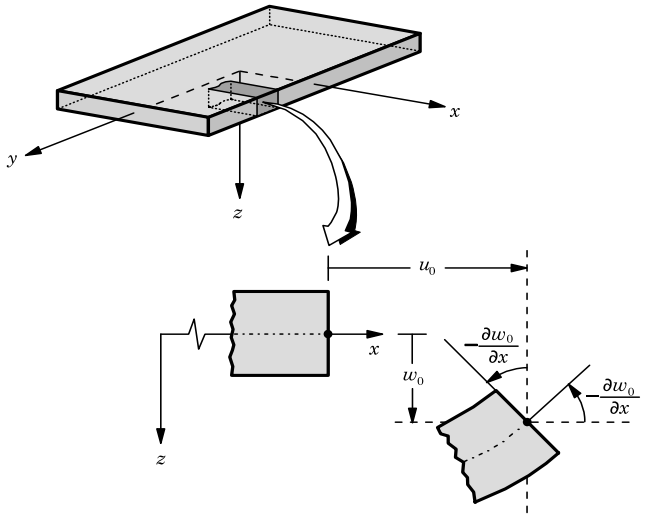

Figure 3.1 The deformed and un-deformed geometries of an edge of a plate under the Kirchhoff assumptions (Reddy, 2007)

These conditions imply that for the time-dependent displacement field holds:

$$u(x,y,z;t) = u_o(x,y;t) - z\frac{\partial w_o}{\partial x} \tag{2.100}$$

$$v(x,y,z;t) = v_o(x,y;t) - z\frac{\partial w_o}{\partial y} \tag{2.101}$$

$$w(x,y,z;t) = w_o(x,y;t) \tag{2.102}$$

along with the inextensibility assumption $\frac{\partial w}{\partial z} = 0$ .In the present study, the strains associated with the displacement field are computed under the infinitesimal strain assumption.

$$\varepsilon_{xx} = \frac{\partial u}{\partial x}, \varepsilon_{yy} = \frac{\partial v}{\partial y}, \varepsilon_{zz} = \frac{\partial w}{\partial z} \tag{2.103}$$

$$\varepsilon_{xy} = \frac{1}{2}(\frac{\partial u}{\partial y} + \frac{\partial v}{\partial x}), \varepsilon_{yz} = \frac{1}{2}(\frac{\partial v}{\partial z} + \frac{\partial w}{\partial y}), \varepsilon_{xz} = \frac{1}{2}(\frac{\partial u}{\partial z} + \frac{\partial w}{\partial x}) \tag{2.104}$$

Consequently from (3.1)-(3.5) we have,

$$\begin{Bmatrix} \varepsilon_{xx} \\ \varepsilon_{yy} \\ \varepsilon_{xy} \end{Bmatrix} = \begin{Bmatrix} \varepsilon^0{}_{xx} \\ \varepsilon^0{}_{yy} \\ \varepsilon^0{}_{xy} \end{Bmatrix} + z \begin{Bmatrix} \varepsilon^1{}_{xx} \\ \varepsilon^1{}_{yy} \\ \varepsilon^1{}_{xy} \end{Bmatrix} \tag{2.105}$$

where $(\varepsilon^0{}_{xx}, \varepsilon^0{}_{yy}, \varepsilon^0{}_{xy})$ are the membrane strains and $(\varepsilon^1{}_{xx}, \varepsilon^1{}_{yy}, \varepsilon^1{}_{xy})$ the flexural bending strains or curvatures. Moreover,

$$\begin{Bmatrix} \varepsilon_{xx} \\ \varepsilon_{yy} \\ \varepsilon_{xy} \end{Bmatrix} = \begin{Bmatrix} \frac{\partial u_o}{\partial x} \\ \frac{\partial v_o}{\partial y} \\ \frac{1}{2}(\frac{\partial u_o}{\partial y} + \frac{\partial v_o}{\partial x}) \end{Bmatrix} + z \begin{Bmatrix} -\frac{\partial^2 w_o}{\partial x^2} \\ -\frac{\partial^2 w_o}{\partial y^2} \\ -2\frac{\partial^2 w_o}{\partial x \partial y} \end{Bmatrix} \tag{2.106}$$

Since the plate domain Ω is thin along the z-direction there can be little variation of the stress components σ_{zz}, τ_{xz}, τ_{yz} through the thickness, and thus they will be approximately zero throughout it every moment in time. This is equivalent with the plane stress assumption. Therefore the constitutive **stress-strain relations for isotropic materials** (Hooke's law) are reduced to the following

$$\begin{bmatrix} \sigma_{xx} \\ \sigma_{yy} \\ \tau_{xy} \end{bmatrix} = \frac{E}{1-v^2} \begin{bmatrix} 1 & v & 0 \\ v & 1 & 0 \\ 0 & 0 & \frac{1-v}{2} \end{bmatrix} \begin{bmatrix} \varepsilon_{xx} \\ \varepsilon_{yy} \\ \varepsilon_{xy} \end{bmatrix} \tag{2.107}$$

The equations of motion of the CPT can be derived using the dynamic version of the principle of virtual displacements, the reader is motivated to refer to the work of Gelfand & Fomin (1963) as well as Reddy (2007) **.**

Rotary inertia terms, which are known to contribute to higher frequencies of vibration are neglected. Then the Euler-Lagrange equations of motion can be derived by expressing the thickness-integrated forces and moments in terms of the displacements.

In our case of linear analysis the coupling between the in-plane displacements (u_o, v_o) with the transverse displacement on the mid-plane w_o and the rotation of the normal to the mid-plane about y-axis, $\partial w_o / \partial x$ disappears.

The structure is subjected to a time-dependent transverse load distribution $q(x;t)$ uniform at any section parallel to the x-axis. This assumption combined with the geometric characteristics of the plate i.e. $l_y \gg l_x, h$, introduces the special case of *cylindrical bending*. In this formulation, the displacements along the y-axis and all derivatives with respect to y are set to zero, leading to a reduced form for the displacement field $u = u(x,z;t),\ v = 0,\ w = w(x,z;t)$, equivalent to the plane strain conditions.

Consequently the governing equations in the domain $(0,L)\times(0,\mathrm{T})$ are the following

$$\frac{E}{1-v^2}\left(\frac{\partial^2 u_o(x;t)}{\partial x^2}\right) = I_o \frac{\partial^2 u_o(x;t)}{\partial t^2} \tag{2.108}$$

$$-\nabla^2[D(x)\nabla^2 w_o(x;t)] + q(x;t) = I_o \frac{\partial^2 w_o(x;t)}{\partial t^2} \tag{2.109}$$

with $I_o = \int_{-h(x)/2}^{h(x)/2} \rho dz = \rho h(x),\ D = \frac{Eh(x)^3}{12(1-v^2)}$, where I_o denotes the mass moment of inertia, ρ is the density of the material, E denotes Young's modulus, v is Poisson's ratio and D is the bending stiffness or flexural rigidity for isotropic materials.

In the present work variations in the flexural rigidity profile are incorporated in the thickness function $h(x)$ whereas all other quantities denote constants, unless stated otherwise.

Expanding the first term in the LHS of (3.10) yields the following expression,

$$\nabla^2[D(x)\nabla^2 w_o(x;t)] = \nabla^2 D(x)\cdot\nabla^2 w_o(x;t) + D(x)\cdot\nabla^4 w_o(x;t) \tag{2.110}$$

This expression contains the biharmonic operator $\nabla^4(.)$, which in 3-D takes the form

$$\nabla^4(.) = \sum_{i=1}^{3}\sum_{j=1}^{3}\partial_i\partial_i\partial_j\partial_j = \frac{\partial^4}{\partial x^4} + \frac{\partial^4}{\partial y^4} + \frac{\partial^4}{\partial z^4} + 2\left(\frac{\partial^4}{\partial x^2\partial y^2} + \frac{\partial^4}{\partial y^2\partial z^2} + \frac{\partial^4}{\partial x^2\partial z^2}\right) \tag{2.111}$$

Generally, the local specification of the primary variables constitutes the geometric boundary or essential conditions, whereas specification of the secondary variables constitutes the natural boundary conditions. The essential boundary conditions alone are sufficient for solving the differential equation. The natural boundary conditions are boundary conditions that involve higher order derivative terms and are not sufficient for solving the differential equation, requiring at least one essential boundary condition.

The modelling of thin plates in cylindrical bending with the CPT yields u_o, w_o, $\partial_x w_o$ as primary variables and N_{xx}, M_{xx} as secondary variables.

$$N_{xx} = \int_{-h/2}^{h/2} \sigma_{xx} dz \tag{2.112}$$

$$M_{xx} = \int_{-h/2}^{h/2} \sigma_{xx} z dz \tag{2.113}$$

Additionally, for the calculation of the dynamic response of the plate, the initial displacement and velocity fields need to be specified throughout the domain of the plate. The above entails specifying the values of the displacements and their first derivatives with respect to time at $t = 0$ for all points in Ω. **The vibrational response of the foil, modelled as a plate,** requires the prediction of all primary variables, and hence the consideration of both in plane and transverse deformations. However, in the context of CPT the deduced equations of motion (3.10)[2] are uncoupled and can be tackled separately. In the present work, where the transverse flexural response of the plate is of importance, equation (3.10) alone will be considered. For all the studied cases, we assume that at $t = 0$ the xy-plane of the chosen coordinate system coincides with the geometric mid-plane of the plate; in other words the plate is considered originally un-deformed. The initial conditions are

$$w_o(x;t)\big|_{t=0} = \partial_t w_o(x;t)\big|_{t=0} = 0 \tag{2.114}$$

Within the framework of this work, the following cases will be presented in terms of boundary conditions:

Case 1: Cantilever plate

The foil is assumed to be clamped at the leading edge at $x_{LE} = 0$ whereas the trailing edge at $x_{TE} = L$ remains unconstrained. To account for these boundary conditions, at the leading edge we have zero deflection and slope. Additionally at the free moving trailing edge, conditions of vanishing moment and shear force are applied.

$$w_o(x;t)\big|_{x=0} = \partial_x w_o(x;t)\big|_{x=0} = 0 \tag{2.115}$$

$$M_{xx} = D(x)\partial_x^2 w_o(x;t)\big|_{x=L} = 0, \quad \mathrm{N}_{xx} = \partial_x [D(x)\partial_x^2 w_o(x;t)]\big|_{x=L} = 0 \tag{2.116}$$

[2] The effects of chord-wise flexibility are predicted, as it will be shown on Chapter 4, with information regarding only the transverse displacement on the mid-plane w_o and the rotation of the normal to the mid-plane about y-axis $\partial_x w_o$.

Case 2: Clamped at centre of rotation with LE and TE as free edges

For this special case where constraints need to be also enforced inside the domain, we need to introduce two structural members in the modelling. In this case the foil of chord length $c = L$ is clamped at the center of rotation, which is positioned $x = x_R$. The origin is positioned at $x_{LE} = 0$ and the member are connected at $x = x_R$.

A more compact formulation with just one structural member is not plausible, since essential conditions are to be enforced only at the boundary in IBVPs.

For that we introduce two plate members, which are modelled using the boundary conditions discussed in Case 1 and share the clamped edge. Therefore, the boundary conditions for the member of the left, with respect to the pivot point are

$$M_{xx} = D(x)\,\partial_x^2 w_o^l(x;t)\Big|_{x=0} = 0, \quad \mathrm{N}_{xx} = \partial_x[D(x)\partial_x^2 w_o^l(x;t)]\Big|_{x=0} = 0 \tag{2.117}$$

$$w_o^l(x;t)\Big|_{x=x_R} = \partial_x w_o^l(x;t)\Big|_{x=x_R} = 0 \tag{2.118}$$

Similarly, for the structural member on the right we have

$$w_o^r(x;t)\Big|_{x=x_R} = \partial_x w_o^r(x;t)\Big|_{x=x_R} = 0 \tag{2.119}$$

$$M_{xx} = D(x)\partial_x^2 w_o^r(x;t)\Big|_{x=L} = 0, \quad \mathrm{N}_{xx} = \partial_x[D(x)\partial_x^2 w_o^r(x;t)]\Big|_{x=L} = 0 \tag{2.120}$$

3.2.1 Weak Formulation of the Initial-Boundary Value Problem (IBVP)

This section is dedicated to the derivation of the weak formulation of the IBVP, which is suitable for the numerical approximation with the use of finite element methods, see e.g. Brenner & Scott (2008), Hughes (1987). Preliminaries and notation for the vector spaces can be found in Appendix A.

Let us be given the classical Sobolev spaces $W^{k,2}(\Omega),\ k \in \mathbb{N}$ and the Banach spaces equipped with the Lebesgue-norm $L^p(\Omega;[0,T])$ for $1 \le p \le \infty$. These spaces $W^{k,2}(\Omega),\ k \in \mathbb{N}$ when equipped with the following *inner product mapping* $L^2[a,b] = \langle x, y \rangle = \int_a^b x(\tau) y(\tau) d\tau$ can be denoted as Hilbert spaces, so that $W^{k,2}(\Omega) = \mathrm{H}^k(\Omega),\ k \in \mathbb{N}$. This mapping also yields an expression similar to the Lebesgue-norm $\|x\| = \left(\int_a^b |x(\tau)|^2 \, d\tau \right)^{1/2}$. Let us now introduce the following subset of $\mathrm{H}^2(\Omega)$ with time as a parameter

$$V := \{ \upsilon(x;t) \in \mathrm{H}^2(\Omega) \ : \ \upsilon\big|_{x=0} = 0,\ \partial_x \upsilon\big|_{x=0} = 0 \} \tag{2.121}$$

The variational formulation of the problem is determined by multiplying the governing equation with a test function $\upsilon \in V$, integrating over Ω and then performing integration by parts. Assuming that every term expresses a Lebesgue integral,

$$\int_0^L \upsilon \partial_{xx} [D(x) \partial_{xx} w_o] dx + \int_0^L \upsilon m(x) \partial_{tt} w_o dx = \int_0^L \upsilon q(x;t) dx \tag{2.122}$$

Integration by parts on the first term in the lhs of (3.15), imposing the natural boundary conditions for the primary variables (defined in Section 3.2) and the fact that the f the test functions satisfy the homogeneous essential conditions yields,

$$\int_0^L \upsilon \partial_{xx} [D(x) \partial_{xx} w_o] dx = \int_0^L D(x) \partial_{xx} w_o \partial_{xx} \upsilon dx. \tag{2.123}$$

Therefore from eq. (3.23) and (3.24) we have,

$$\int_0^L D(x) \partial_{xx} w_o \partial_{xx} \upsilon dx + \int_0^L m(x) \upsilon \partial_{tt} w_o dx = \int_0^L \upsilon q(x;t) dx \tag{2.124}$$

By introducing the bilinear functional $\alpha : V \times V \to \mathbb{R}$

$$a(w_o, \upsilon) = \int_0^L D(x) \partial_{xx} w_o \partial_{xx} \upsilon dx \tag{2.125}$$

in conjunction with (3.25) we can present the variational formulation of the problem in a more compact notation.

Find $w_o \in V$ such that for every test function $\upsilon \in V$ the following holds

$$a(w_o, \upsilon) + \int_0^L m(x)\upsilon \partial_{tt} w_o dx = \langle q, \upsilon \rangle\big|_{L^2(\Omega)} \qquad (2.126)$$

with initial conditions $\langle w_o(x,0), \upsilon \rangle\big|_{L^2(\Omega)} = \langle \partial_t w_o(x,0), \upsilon \rangle\big|_{L^2(\Omega)} = 0$.

Proving the solution existence and uniqueness of aforementioned variational problem is not trivial and therefore is left for future work.

3.2.1.1. Semi-discretization using Galerkin approximation methods

In numerical analysis, Galerkin projection methods refer to a class of techniques used for the construction of a semi-discrete approximation to the solution of variational problems with respect to the spatial variable, see e.g. Zaglmayr (2006). In that sense, we introduce the finite-dimensional subspace $V^h \subset V$, with super-script h referring to a discretization parameter. We also assume that under reasonable assumptions the discrete solution $u^h \in V^h$ converges to the solution $w_o \in V$ as $h \to 0$.

The mathematical proof of this statement is not the subject of this study, but nevertheless an interesting topic for future research and analysis. The projected formulation of the variational problem in (3.27) is the following:

Find a solution $u^h \in V^h$ so that $\forall \upsilon^h \in V^h$ the Galerkin equation holds

$$a(u^h, \upsilon^h) + \int_0^L m(x)\upsilon^h \partial_{tt} u^h dx = \langle q, \upsilon^h \rangle\big|_{L^2(\Omega)} \qquad (2.127)$$

with initial conditions $\langle u^h(x,0), \upsilon^h \rangle\big|_{L^2(\Omega)} = \langle \partial_t u^h(x,0), \upsilon^h \rangle\big|_{L^2(\Omega)} = 0$

To ensure that the approximated solution has the desirable smoothness, i.e. $u^h \in C^1(\Omega)$ we chose the set of Hermite polynomials as basis functions for the discrete subspace $V^h \subset V$. The construction of H^2 conforming elements is necessary in this case, since second order derivatives appear in the semi-discrete variational problem,

see equation (3.28). The solution expansion in the chosen finite-dimensional space V^h is given by a mapping expressed by

$$u^h = \sum_i^n u_i^h(t) H_i(x) \tag{2.128}$$

where $u_i^h(t)$ denote the time-dependent nodal unknowns and n the number of employed shape functions as will be thoroughly discussed in the next section. If we expand the solution u^h in terms of a basis $(H_i)_{1\le i\le n}$ in V^h and allow the test functions υ^h to coincide with the chosen basis (Bubnov-Galerkin method) we can derive a linear system of equations with respect to the unknown nodal variables.

The nodal unknowns for each representation are uniquely defined as an N -tuple and therefore, a solution approximation to the dynamic structural problem is accomplished when all the nodal unknowns are defined for every moment in time.

By substituting (3.29) in (3.28) we can derive for $\forall H_j$, j=1…n

$$\begin{aligned} &\int_\Omega D(x)\partial_{xx}\left(\sum_i^n u_i^h(t)H_i(x)\right)\partial_{xx}H_j(x)dx + \int_\Omega m(x)H_j\partial_{tt}\left(\sum_i^n u_i^h(t)H_i(x)\right)dx \\ &= \int_\Omega H_j(x)q(x,t)dx \end{aligned} \tag{2.129}$$

with initial conditions

$$\left\langle \sum_i^n u_i^h(0)H_i(x), H_j \right\rangle\Big|_{L^2(\Omega)} = \left\langle \sum_i^n \partial_t u_i^h(0)H_i(x), H_j \right\rangle\Big|_{L^2(\Omega)} = 0 \tag{2.130}$$

3.3 Discretization Scheme for hp-FEM

During the 1970s the use of low-order polynomials over successively finer meshes was the predominant philosophy for finite element analysis for solution refinement and increase in accuracy. However, the pioneering work of Babuška and Szabo during the following years led to the development of the so-called hp-FEM. The main idea behind this approach is that solution refinement can be achieved with proper mesh selection, i.e. *h* version, combined with increase of the polynomial degree of the finite elements used in modelling, i.e. *p* version see Babuska et al. (1981).

Motivated by the trade-off between the required mesh size and interpolation complexity for the same degree of accuracy we approximate the solution of the aforementioned problem with an hp-FEM.

We begin with the definition of Hermite finite elements by (Ciarlet, 1978),

Definition. Let

(i) $\Omega^h \subseteq \Omega$ be a bounded closed set with nonempty interior and piecewise smooth boundary (the element domain)

(ii) $P \equiv V^h$ be a finite-dimensional space of function on K (the space of shape functions)

(iii) $N = \{N_1, \ldots, N_n\}$ be a basis for P' (the set of nodal variables).

Then (Ω^h, P, N) is called a finite element. The basis function set of Hermite polynomials, of degree $p = 2k+1, k \geq 1$, denoted $\{H_1, H_2, \ldots H_n\}$ of P dual to N (i.e. $N_i(H_j) = \delta_{ij}$) is called the nodal basis of P. It is noted that index n, i.e. the number of employed shape functions in the set, is related to the polynomials degree of the shape functions as $n = p+1$.

The total number of finite elements is denoted as N_{elem} and the subintervals in the discretized domain as $I_e = [x_{k-1}, x_k]$ where $k = 1, \ldots, N_{elem}$. In the present work the simpler piecewise Hermite polynomials of order $p = 3,5$ for $k = 1,2$ are used, for which $n = 4$ and $n = 6$ respectively.

The reader can refer to Appendix B for the derivation of these special functions We define the global Hermite polynomials with local support on an arbitrary finite element subinterval (Fig 3.2). For $e = 1, \ldots, N_{elem}$ and $i = 1, \ldots, n$

$$H_i^e(x) = \begin{cases} H_i(x) & \mathrm{x} \in \mathrm{I}_e \\ 0 & \mathrm{x} \in \{\Omega^h - \mathrm{I}_e\} \end{cases} \tag{2.131}$$

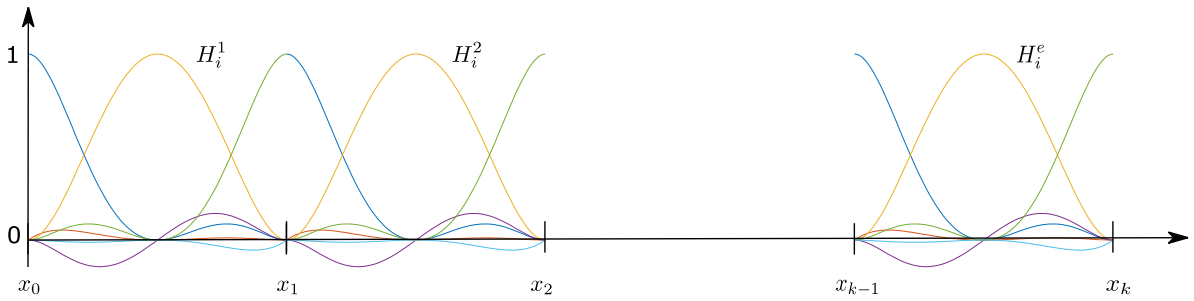

Figure 3.2 Global Hermite Shape Functions of 5th order with local support.

As it was previously discussed, the aim of Galerkin's method is to derive a linear system of equations that can be easily used to compute the solution by a computer. If we denote by $u_i^e(t)$ the nodal unknowns for an arbitrary element in the proposed discretization, and H_j^e are the Hermite basis functions equation (3.29) on the local support of a finite element $e(\Omega^h)$ is reduced to,

$$\begin{aligned}&\int_{e(\Omega^h)} D(x)\partial_{xx}\left(\sum_i^n u_i^e(t)H_i^e(x)\right)\partial_{xx}H_j^e(x)dx + \int_{e(\Omega^h)} m(x)H_j^e\partial_{tt}\left(\sum_i^n u_i^e(t)H_i^e(x)\right)dx \\ &= \int_{e(\Omega^h)} H_j^e(x)q(x,t)dx, \quad \forall H_j^e(x) \quad j=1,\dots n\end{aligned} \tag{2.132}$$

For each term in the above equation we use identities regarding the summation operator and the integrals, for example for the first integral in the lhs it holds

$$\int_{e(\Omega^h)} D(x)\partial_{xx}\left(\sum_i^n u_i^e(t)H_i^e(x)\right)\partial_{xx}H_j^e(x)dx = \sum_i^n u_i^e(t)\left(\int_{e(\Omega^h)} D(x)\partial_{xx}H_i^e(x)\partial_{xx}H_j^e(x)dx\right) \tag{2.133}$$

Similarly for the second integral

$$\int_{e(\Omega^h)} m(x)H_j^e\partial_{tt}\left(\sum_i^n u_i^e(t)H_i^e(x)\right)dx = \sum_i^n \partial_{tt}u_i^e(t)\left(\int_{e(\Omega^h)} m(x)H_i^e(x)H_j^e(x)dx\right) \tag{2.134}$$

Consequently (3.33) along with (3.34) and (3.35) becomes,

$$\begin{aligned}&\sum_i^n \partial_{tt}u_i^e(t)\left(\int_{e(\Omega)} m(x)H_i^e(x)H_j^e(x)dx\right) + \sum_i^n u_i^e(t)\left(\int_{e(\Omega^h)} D(x)\partial_{xx}H_i^e(x)\partial_{xx}H_j^e(x)dx\right) \\ &= \int_{e(\Omega^h)} H_j^e(x)q(x,t)dx, \quad \forall H_j^e(x) \quad j=1,\dots n\end{aligned} \tag{2.135}$$

The initial conditions become $\forall H_j^e(x) \quad j=1,\dots n$,

$$\int_{e(\Omega^h)}\left(\sum_i^N u_i^h(0)H_i^e(x)\right)H_j^e dx = \int_{e(\Omega^h)}\left(\sum_i^N \partial_t u_i^h(0)H_i^e(x)\right)H_j^e dx = 0 \tag{2.136}$$

This expression can be interpreted as an approximation to the solution restricted to the local support of an arbitrary finite element $e(\Omega^h)$. However, a more compact notation can be introduced using (3.32).

$$\mathbf{M}_{loc} = \left(a(H_i^e, H_j^e)\right)_{1\le i,j\le n} = \int_{\Omega^h} m(x)H_i^e(x)H_j^e(x)dx = \int_{e(\Omega^h)} m(x)H_i(x)H_j(x)dx \tag{2.137}$$

$$\mathbf{K}_{loc} = \left(b(H_i^e, H_j^e) \right)_{1\le i,j\le n} = \int_{\Omega^h} D(x)\partial_{xx}H_i^e(x)\partial_{xx}H_j^e(x)dx = \int_{e(\Omega^h)} D(x)\partial_{xx}H_i(x)\partial_{xx}H_j(x)dx \tag{2.138}$$

$$\mathbf{f}_{loc} = \left(f(H_j^e) \right)_{1\le j\le n} = \int_{\Omega^h} H_j^e(x)q(x,t)dx = \int_{e(\Omega^h)} H_j(x)q(x,t)dx \tag{2.139}$$

$$U\big|_e = \left(u_i^e \right)_{1\le i\le n} \tag{2.140}$$

By substituting (3.38)-(3.41) into (3.36) we have

$$\mathbf{M}_{loc}\ddot{U}\big|_e + \mathbf{K}_{loc}U\big|_e = \mathbf{f}_{loc} \tag{2.141}$$

where $\mathbf{M_{loc}} \in \mathbb{R}^{n\times n}$, $\mathbf{K_{loc}} \in \mathbb{R}^{n\times n}$ stand for the local element mass and stiffness matrices respectively, $\mathbf{f}_{loc} \in \mathbb{R}^n$ for the local load vector and $U\big|_e \in \mathbb{R}^n$ for the vector containing the nodal unknowns for interval I_e. Numerically the integrals are approximated using Gaussian quadrature, see Appendix C for more details.

The next important step in this process is the *assembly* of the inner product terms, as introduced in the set of (3.38)-(3.42), by summing the constituent parts over each *element.* These quantities are used to construct the *global matrices* and are independent from each other from a computational point of view.

The numbering scheme utilized is called *the global-to-local* index. This index $k(e,l)$ relates the local node number l, on a particular element e, to its position in the global data structure. Technical details regarding the implementation in an algorithmic level are not presented here, however the interested reader can refer to Hughes (1987)

The total number of nodal variable unknowns, that defines the dimensions of the global matrices, is equal to the number of finite elements N_{elem} times the number of DOFs per element, i.e. $N_T = n \cdot N_{elem}$. Using (3.30) and (3.31) along with the compact notation in the set of equations (3.38)-(3.42) we can derive the global matrix equation

$$\mathbf{M}_{glob}\ddot{U} + \mathbf{K}_{glob}U = \mathbf{F} \tag{3.28}$$

where $\mathbf{M}_{glob} \in \mathbb{R}^{N_T\times N_T}$, $\mathbf{K}_{glob} \in \mathbb{R}^{N_T\times N_T}$ stand for the global mass and stiffness matrices respectively, $\mathbf{F}_{glob} \in \mathbb{R}^{N_T}$ is the global load vector and $U \in \mathbb{R}^{N_T}$ is the vector containing the nodal unknowns for the partitioned domain Ω^h.

3.3.1 Addition of Proportional Damping Terms

In *proportional* or *classical damping*, an idealized damping method as introduced by Rayleigh, the damping matrix is assumed to be a linear combination of the mass and stiffness matrices. That is for $\alpha_1, \alpha_2 \in \mathbb{R}$

$$\mathbf{C} = \alpha_1 \mathbf{M}_{glob} + \alpha_2 \mathbf{K}_{glob} \tag{2.142}$$

Addition of the proportional damping terms yields an extended global equation

$$\mathbf{M}_{glob}\ddot{U} + \mathbf{C}\dot{U} + \mathbf{K}_{glob}U = \mathbf{F} \tag{2.143}$$

owever, for systems with many degrees of freedom is its quite difficult to guess meaningful values for the Rayleigh damping coefficients at the beginning of each analysis. In this work we follow a procedure presented by Dasgupta et al. (2003) that ensures a rational estimate for $\alpha_1, \alpha_2 \in \mathbb{R}$ and takes into account that modal mass participation decreases with increase in modes.

- The procedure begins with modal analysis and identification of the significant modes (=m), i.e. the natural frequencies ω_i.
- Then we select the damping ratio ζ_1 for the first mode of the system, as well as the damping ratio ζ_m of the mth significant mode.
- For intermediate modes i, where $1 < i < m$ we obtain ζ_i using the following formula, based on linear interpolation

  $$\zeta_i = \frac{\zeta_m - \zeta_1}{\omega_m - \omega_1}(\omega_i - \omega_1) + \zeta_1 \tag{2.144}$$

  whereas for modes greater than m the values are extrapolated based on the following formula

  $$\zeta_i = \frac{\zeta_m - \zeta_1}{\omega_m - \omega_1}(\omega_{m+i} - \omega_m) + \zeta_1 \tag{2.145}$$

  where $m < i < 2.5m$
- Based on the above set of data we can obtain $\alpha_2 \in \mathbb{R}$ as,

  $$a_2 = \frac{2\zeta_1\omega_1 - 2\zeta_m\omega_m}{\omega_1^2 - \omega_m^2} \tag{2.146}$$

- Then by substituting this value into the following expression we obtain $\alpha_1 \in \mathbb{R}$

  $$2\zeta_1\omega_1 = a_1 + a_2\omega_1^2 \tag{2.147}$$

- If we repeat this process for the first and 2.5mth mode we will obtain another set of data for the Rayleigh coefficients. In the present work the average values were used as a better approximation.

The behaviour of the attributed damping ratio values as a function of the natural frequency values of the system under study is presented in Figure 3.3. The first portion of the curve shows nonlinearity and beyond that the curve is linear.

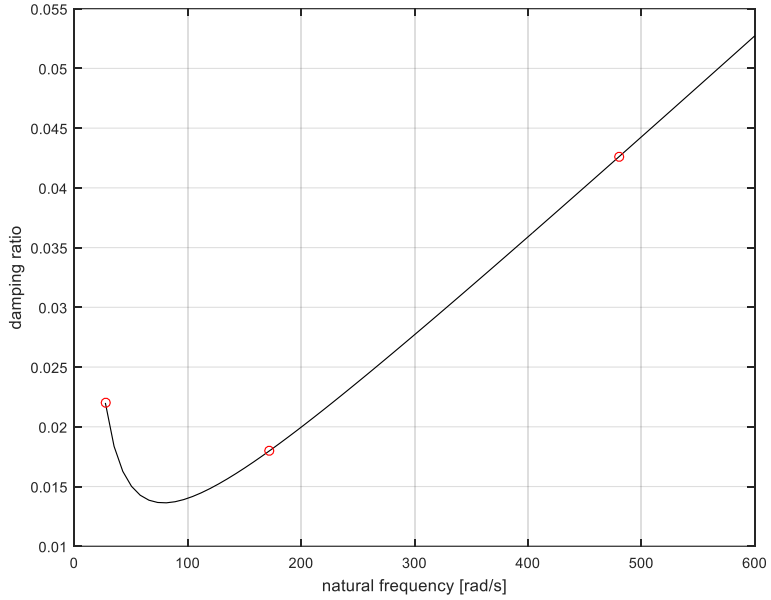

Figure 3.3 Damping ratio-natural frequency data set for a thin plate of $D = 0.072\ Nm$ with $m = 2$, $\zeta_1, \zeta_m = 0.022$ based on Dasgupta et al. (2003). The first three natural frequencies are added as points to the graph. The proportional damping coefficients are $a_1 = 1.0755$ and $a_2 = 1.7274e-4$.

3.3.2 Time Marching

The extended global equation (3.44) is in fact a system of second order differential equations with initial conditions. For the solution of system as such, i.e. approximation of the nodal variable unknowns, we perform order reduction by assuming that $x = U,\ \mathrm{y} = \dot{U}$. The following system of first order differential equations is derived,

$$\begin{cases} \mathbf{M}_{glob}\dot{y} + \mathbf{C}y + \mathbf{K}_{glob}x = \mathbf{F}_{glob} \\ \dot{x} - y = \mathbf{0} \end{cases} \tag{2.148}$$

By introducing matrix notation it holds,

$$\begin{bmatrix} \mathbf{0} & \mathbf{M}_{glob} \\ \mathbf{I} & \mathbf{0} \end{bmatrix} \begin{bmatrix} \dot{x} \\ \dot{y} \end{bmatrix} + \begin{bmatrix} \mathbf{K}_{glob} & \mathbf{C}_{glob} \\ \mathbf{0} & \mathbf{-I} \end{bmatrix} \begin{bmatrix} x \\ y \end{bmatrix} = \begin{bmatrix} \mathbf{F}_{glob} \\ \mathbf{0} \end{bmatrix} \tag{2.149}$$

or in a more compact form

$$\mathbf{A}\dot{Q} = \mathbf{B}Q + \mathbf{F},\ Q = \begin{bmatrix} U & \dot{U} \end{bmatrix}^T \tag{2.150}$$

where $\mathbf{A}=\begin{bmatrix}\mathbf{0} & \mathbf{M}_{glob}\\ \mathbf{I} & \mathbf{0}\end{bmatrix}$, $\mathbf{B}=-\begin{bmatrix}\mathbf{K}_{glob} & \mathbf{C}\\ \mathbf{0} & -\mathbf{I}\end{bmatrix}$, $\mathbf{F}=\begin{bmatrix}\mathbf{F}_{glob}\\ \mathbf{0}\end{bmatrix}$, and $\mathbf{I}$ is the identity matrix known from linear algebra.

For the numerical solution of the above system we present the simple Implicit Euler method and the Crank-Nicolson scheme for time-integration, see e.g. Stoer & Burlish (1991). The implicit Euler method can be derived through integration of (3.37) from t_n to $t_{n+1}=t_n+dt$ and the use of the right-hand rectangle method (with one rectangle) for the integral approximation. This yields,

$$\int_{t_n}^{t_{n+1}}\mathbf{A}\dot{Q}dt=\int_{t_n}^{t_{n+1}}\mathbf{B}Qdt+\int_{t_n}^{t_{n+1}}\mathbf{F}dt \quad \Rightarrow$$

$$\mathbf{A}\left(Q(t_{n+1})-Q(t_n)\right)=\mathbf{B}Q(t_{n+1})dt+\mathbf{F}(t_{n+1})dt \quad \Rightarrow$$

$$Q(t_{n+1})=[\mathbf{A}-\mathbf{B}dt]^{-1}\left(\mathbf{A}Q(t_n)+\mathbf{F}(t_{n+1})dt\right) \qquad (2.151)$$

This method is very simple, it has 1st order accuracy and is also L-stable. The Crank-Nicolson scheme, that has 2nd order accuracy and is A-stable, can be derived through integration from t_n to $t_{n+1}=t_n+dt$ and the use of the trapezoidal rule for the integral approximation.

$$Q(t_{n+1})=[\mathbf{A}-\mathbf{B}\,dt/2]^{-1}\left([\mathbf{A}+\mathbf{B}\,dt/2]Q(t_n)+[\mathbf{F}(t_n)+\mathbf{F}(t_{n+1})]\,dt/2\right) \qquad (2.152)$$

This approach yields as a numerical output at each time step of the simulation the nodal unknowns of the transverse displacement on the mid-plane w_o^h, the rotation of the normal to the mid-plane about y-axis $\partial_x w_o^h$ as well as their time derivatives $\partial_t w_o^h$ and $\partial_t(\partial_x w_o^h)$.Finally, the obtained values of the nodal unknowns can be used to approximate the transverse displacement in $\Omega\times(0,T)$ with $u^h(x;t)=\sum_i^n u_i^h(t)H_i(x)$.

3.4 Numerical Results and Validation

In order to validate the developed FEM solver, we performed various comparisons between analytic solutions, found in the literature and the proposed numerical scheme. Free vibration analysis of a linearly double-tapered cantilever beam (Fig. 3.4) with the same taper ratio in both axis, i.e. in terms of horizontal and vertical dimensions, is presented in the work of Mabie & Rogers (1974). The relative error found for the first five fundamental frequencies, calculated by the present FEM for a mesh of $N_{elem} = 15,$ is compared against the analytic solution as shown in Table I. The results were found in good agreement, which can be further enhanced with refined discretization.

The static behaviour of a non-prismatic cantilever beam under tip load forcing is studied by Beltempo et al. (2015). In Figures 3.4 & 3.5 we compare the transversal displacement distributions taken from the literature with the obtained numerical results, confirming once again that they are in good agreement.

The first graph refers to CASE1 where the thickness profile varies linearly with parameter $H = 0.25\,\text{m}$ for a beam of $L = 10\,\text{m}$ length. The material properties are $E = 10^8\ \text{kN/m}^2,\ \text{v} = 0.3$ and the tip load is equal to $P = -100\ kN$. Whereas in CASE2 that is depicted in Figure 3.6 the thickness varies nonlinearly with the same parameter $H = 0.25\,\text{m}$.

Finally, the FEM solver was validated against a dynamic test case of a cantilever beam of a constant thickness profile, under transverse dynamic tip loading. The beam's response in terms of free tip transverse displacement profile is compared in Figure 3.5 against the analytic solution found in Warburton (1976).

TABLE I
MODAL ANALYSIS FOR DOUBLE TAPERED CANTILEVER BEAMS

	Mabie et al.(1974)		Relative error with FEM (% x1e-3)	
Taper ratio	a = 5.0	a = 10.0	a = 5.0	a = 10.0
Ω_1	30.9820	72.0487	0.1451	0.0231
Ω_2	91.9273	186.802	0.0410	0.2007
Ω_3	199.1682	371.238	0.0197	0.1413
Ω_4	356.2088	635.049	0.0198	0.1609
Ω_5	564.1394	981.657	0.0835	0.5628

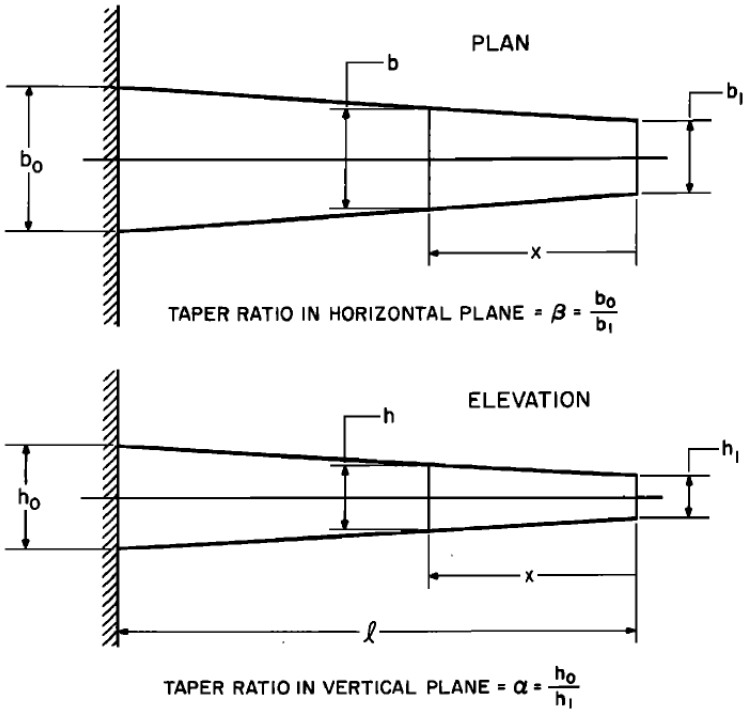

Figure 3.4 Cantilever beam linearly tapered in horizontal and vertical planes simultaneously, see Mabie & Rogers (1974)

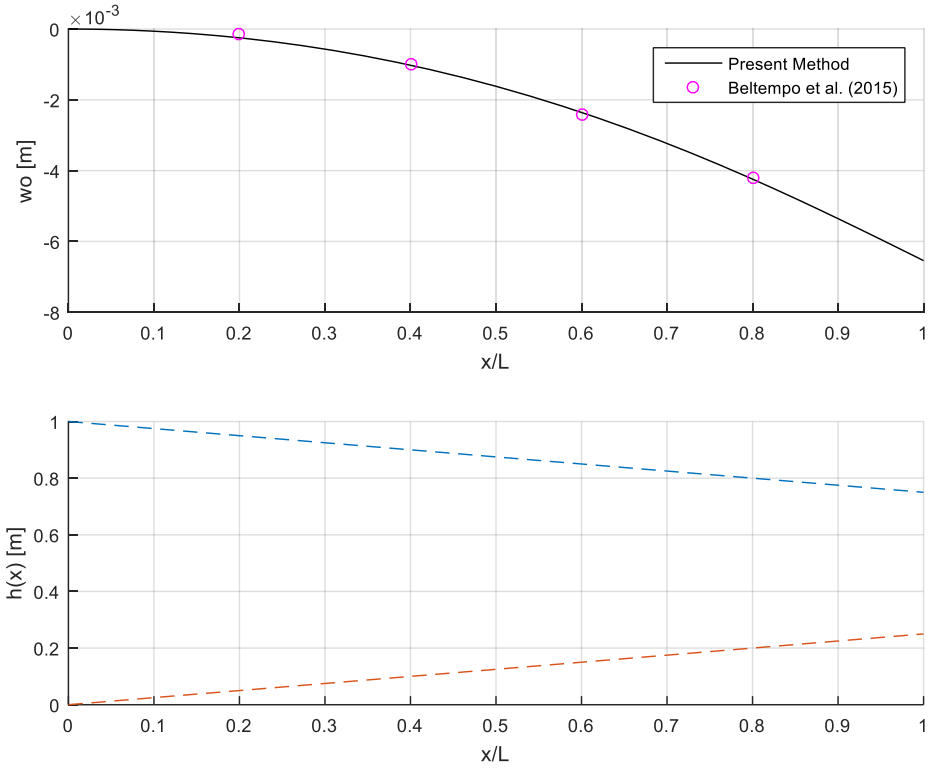

Figure 3.5 Static response for non-prismatic beams and comparison with CASE1 in Beltempo et al. (2015). The transverse displacement comparison and the thickness profile are displayed in the upper and lower graph respectively.

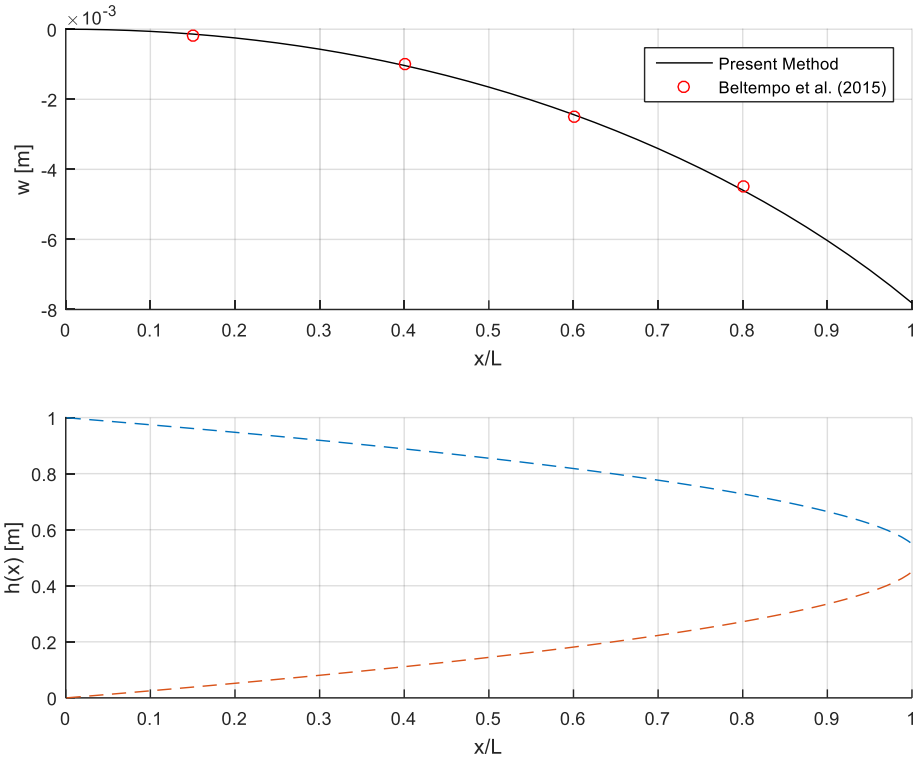

Figure 3.6 Static response for non-prismatic beams and comparison with CASE 2 Beltempo et al. (2015). The transverse displacement comparison and the thickness profile are displayed in the upper and lower graph respectively.

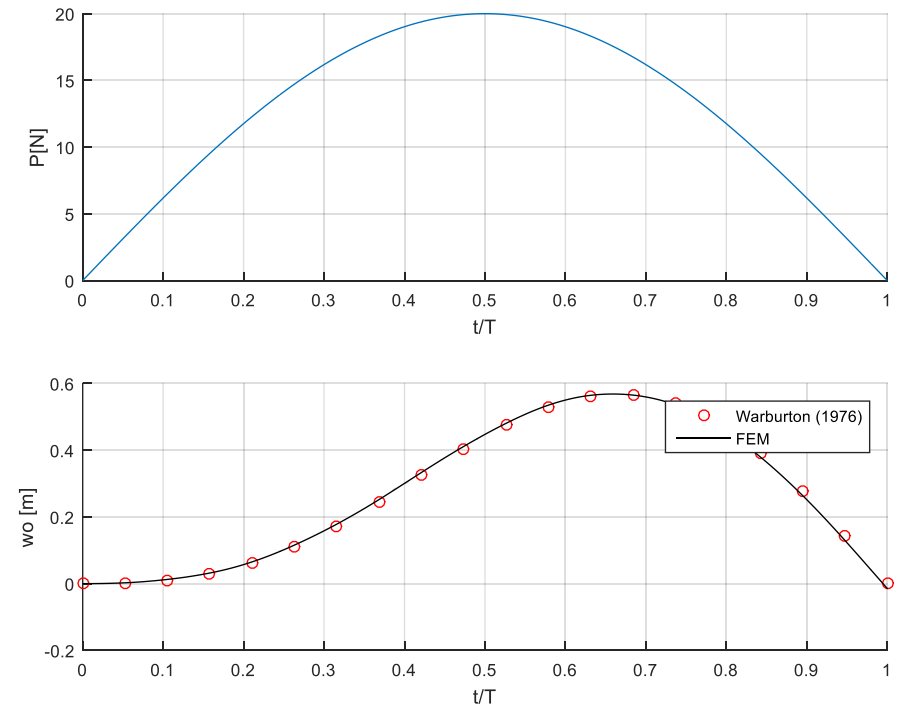

Figure 3.7 Dynamic response of the tip of a cantilever beam under point load. Comparison against the data published in Warburton (1976).

Chapter 4 - Coupled model for the fluid-structure interaction of chord-wise flexible foil thrusters

In this final chapter the hydro-elastic analysis of chord-wise flexible hydrofoils with flexural rigidity profile variation in unsteady motion is discussed and a fully coupled BEM-FEM numerical scheme is established for the solution of this complex fluid-structure interaction problem. The chord-wise pressure distribution is predicted with a boundary element formulation (BEM) for unsteady lifting flows around hydrofoils, whereas the structural response of the foil is approximated using a finite element method (FEM) based on Kirchhoff's thin plate theory.

The coupled numerical scheme presented in this work is an extension to methodology developed in the Laboratory of Ship and Marine Hydrodynamics at the National Technical University of Athens (NTUA) by Filippas et al. (2018), that treated the hydro-elastic problem of a semi-activated rigid biomimetic energy device in waves and currents nearshore with one degree of freedom and Priovolos et al. (2018), that studied the structural response of chord-wise flexible flapping foils operating as biomimetic thrusters as a system with multiple degrees of freedom.

4.1 Formulation of the fluid-structure interaction problem

The fluid flow domain is assumed to be the open domain $D \subseteq R^2$ with time-dependent boundaries $\partial D(t) = \partial D_B(t) \cup \partial D_W(t)$ corresponding to the foil's exterior surface and the trailing vortex sheet respectively. These boundaries are defined with respect to an earth-fixed coordinate system $0xy$. Additionally we introduce a non-inertial body-fixed coordinate system $0x'y'$, fixed at the foil's center of rotation along chord length with no-inclination as well as a body-fixed curvilinear coordinate system defined on the body boundary (Figure 4.1). Each point in the curvilinear system is represented by $\mathbf{r}(s;t)$, whereas $\mathbf{n}(s;t), \boldsymbol{\tau}(s;t)$ denote the unit normal and tangent vectors.

From now on, the superscripts $\{u,l\}$ will be used to denote wake's upper and lower side respectively while the indices $\{B,W\}$ denote values on the body surface and the wake of the hydrofoil respectively. In this sections we introduce briefly the mathematical formulation for the unsteady lifting flow problem but the interested reader can refer to Chapter 2 for more details.

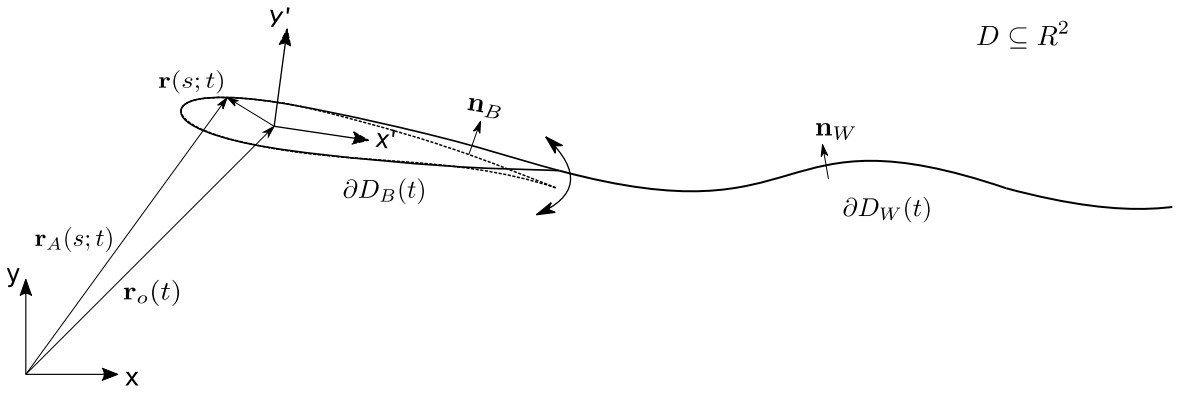

Figure 4.1 The moving inertial and body-fixed frames of the chord-wise flexible flapping foil. The rigid foil geometry is denoted as a solid line, whereas the deformed state with a dashed curve.

The governing equation for the potential field under the assumptions of irrotationality is

$$\nabla^2\Phi(x,y;t)=0 \tag{4.1}$$

where $\nabla\Phi(x,y;t)$ denotes the gradient of the potential component at a $(x,y;t)$ point. The no-entrance boundary condition that must be satisfied is

$$\nabla\Phi(x,y;t)\cdot\mathbf{n}_B=\mathbf{V}_B\cdot\mathbf{n}_B \quad (x,y)\in\partial D_B(t) \tag{4.2}$$

where $\mathbf{n}_B=\mathbf{n}_B(x,y;t)$ refers to the unit normal vector and $\mathbf{V}_B$ on the total velocity on the body boundary. The behaviour of the potential field at infinity can be modelled as

$$\lim_{\|x\|\to\infty}\Phi=0,\ \lim_{\|x\|\to\infty}\nabla\Phi=0 \tag{4.3}$$

The following kinematic condition ensures the continuity of the normal velocity vector through the wake,

$$\frac{\partial\Phi_W^u(x,y;t)}{\partial n}=\frac{\partial\Phi_W^l(x,y;t)}{\partial n},\ (x,y)\in\partial D_W \tag{4.4}$$

whereas the physical meaning behind the dynamic condition; that is the inability of the wake to support pressure difference

$$p_W^u(x,y;t)=p_W^l(x,y;t),\quad (x,y)\in\partial D_W \tag{4.5}$$

A nonlinear pressure type Kutta condition that requires the pressure difference at the trailing edge to be zero is also implemented along frozen wake modelling for the trailing vortex sheet. If we assume that $b=\mathbf{V}_B\cdot\mathbf{n}_B$ then the pressure-type Kutta condition holds as,

$$\frac{d\left(\Phi_{TE}^{u\ *}-\Phi_{TE}^{l\ *}\right)}{dt}+\left(\frac{\nabla\Phi_{TE}^{u\ *}+\nabla\Phi_{TE}^{l\ *}}{2}+b\ \cdot\mathbf{n}_B-\mathbf{V}_B\right)\cdot\left(\nabla\Phi_{TE}^{u\ *}-\nabla\Phi_{TE}^{l\ *}\right)=0 \tag{4.6}$$

However, the solution of the lifting flow problem is obtained when Green's theorem is applied in conjunction with equation (4.3) for the unbounded domain treatment, so that the total potential is expressed as a function of the boundary values of the potential Φ and its derivative $\partial\Phi/\partial n$. For each point $(x_0,y_0)\in\partial D(t)$

$$\begin{aligned}&\frac{1}{2}\Phi_B(x_0,y_0;t)+\int_{\partial D_B(t)}\Phi_B(x,y;t)\frac{\partial G(x_0,y_0\,|\,x,y)}{\partial n}ds(x,y)=\\&\int_{\partial D_B(t)}\underbrace{\boldsymbol{V}_B\cdot\boldsymbol{n}_B}_{b\ x,y;t}G(x_0,y_0\,|\,x,y)ds(x,y)-\int_{\partial D_W(t)}[\![\Phi_W]\!](x,y;t)\frac{\partial G(x_0,y_0\,|\,x,y)}{\partial n}ds(x,y)\end{aligned} \tag{4.7}$$

where $[\![\Phi_W]\!]=\Phi_W^u-\Phi_W^l=\mu_W$ denotes the potential jump or the dipole intensity on the wake. Moreover, an unsteady version of Bernoulli's equation derived from Euler's equation was employed, see e.g. Filippas (2013),

$$\frac{p}{\rho}=-\frac{\partial\Phi}{\partial t}-\frac{1}{2}\left(\nabla\Phi\right)^2 \tag{4.8}$$

in order to calculate the pressure difference coefficient on the thin hydrofoil for a velocity, that is characteristic for the foil motion (e.g. the forward velocity of flapping foil thruster) as

$$\Delta C_P=\frac{p_l-p_u}{\frac{1}{2}\rho U^2} \tag{4.9}$$

In the present study, the unsteady flapping motion of the foil is described by three degrees of freedom (i) the forward motion $s(t)$, (ii) the heaving $h(t)$ and (iii) pitching motion $\theta(t)$ with respect to the inertial reference frame, see Section 2.4.1.

From a structural point of view, the foil is modelled as a thin elastic plate of chord length c, clamped at the centre of rotation at $x=x_R$ with free trailing and leading edges. The foil deforms under the effects of hydrodynamic pressure and non-inertial forces. To model the structural response of the foil's camber line we introduce another non-inertial body-fixed coordinate system fixed at the leading edge with no inclination, to comply with the problem formulation presented in Chapter 3. It is noted that, this coordinate system is different from the ones introduced in the hydrodynamic modelling.

The structural response of the foil's camber line is given as the solution of the following initial boundary value problem (IBVP). The governing equation in terms of the transverse displacement $w_o(x;t)$ in domain $[0,c]\times(0,T)$ holds as

$$m(x)\frac{\partial^2 w_o(x;t)}{\partial t^2}+\nabla^2[D(x)\nabla^2 w_o(x;t)]=q_{Hydro}(x;t)+q_{Ficticious}(x;t) \tag{4.10}$$

with $m(x)=\rho h(x)$ denoting the mass distribution, $D(x)=\frac{Eh(x)^3}{12(1-v^2)}$ the flexural rigidity for isotropic materials, $q_{Hydro}(x;t)$ the hydrodynamic pressure forcing term and $q_{Fictitious}(x;t)$ the distributed loads due to non-inertial forces. For completeness $h(x)$ denotes the thickness profile of the foil, c the chord length, ρ the material density, E Young's modulus and v Poisson's ratio.

Particularly, we assume that the structure experiences hydrodynamic effects, see equation (4.9), in terms of chord-wise pressure difference distribution given by the following expression,

$$q_{Hydro}(x;t)=\frac{1}{2}\rho U_\infty^2\Delta C_p \tag{4.11}$$

The structure also experiences fictitious forces due to the non-inertial motions enforced to the pivot point, so that

$$q_{Fictitious}(x;t)=-m(x)\left(w_o(x;t)\cdot\dot{\theta}^2(t)+x'\cdot\ddot{\theta}(t)+\ddot{h}(t)\cos\theta(t)\right) \tag{4.12}$$

where $\theta(t), h(t)$ denote the pitching and heaving motions respectively. For more details about the derivation of the resulting fictitious forces the interested reader can refer to the work by Priovolos et al. (2018).

Regarding the initial conditions we assume that

$$w_o(x;t)\Big|_{t=0}=\partial_t w_o(x;t)\Big|_{t=0}=0 \tag{4.13}$$

whereas for the boundary conditions it holds,

$$M_{xx}=D(x)\partial_x^2 w_o(x;t)\Big|_{x=0,c}=0,\quad \mathrm{N}_{xx}=\partial_x[D(x)\partial_x^2 w_o(x;t)]\Big|_{x=0,c}=0 \tag{4.14}$$

$$w_o(x;t)\Big|_{x=x_R}=\partial_x w_o(x;t)\Big|_{x=x_R}=0 \tag{4.15}$$

Rendering the analytical solution of the problem formulated above is at this point unachievable, as the structural and the hydrodynamic problem are coupled in an implicit manner with encapsulated forms of non-linearity. To begin with, the forcing term in equation (4.2) cannot be explicitly written in terms of the unknown transverse

displacement field $w_o(x;t)$, since it is dependent on the mid-plane deformation which coincides with the foil's camber line, and vice versa. Thus the pressure forcing term should be formally written as $q_{Hydro}(x,t;w_o(x;t))$.

The underlying coupling mechanism between the hydrodynamic and the structural problem is introduced through adjustments in the no-entrance boundary condition. The no-entrance boundary condition, introduced in equation (4.2), needs to be modified to include the deformation velocity. In that sense, the total velocity on the body boundary is

$$\mathbf{V}_B = \mathbf{V}_{Rigid} + \partial_t w_o \cdot \mathbf{n}_{rigid} \tag{4.16}$$

$$\mathbf{n}_{rigid} = [-\sin\theta(t), \cos\theta(t)]^T \tag{4.17}$$

where $\mathbf{V}_{Rigid}$ denotes the velocity of the body boundary due to rigid motions, $\mathbf{n}_{rigid}$ the unit vector normal to the camber line in its un-deformed state and $\partial_t w_o \cdot \mathbf{n}_{rigid}$ the deformation velocity projected in the direction of $y'-$ axis, which also corresponds to the camber line in its un-deformed state.

4.2 Discretization Scheme for the Coupled Problem

4.2.1 Discretization Scheme for the Lifting Flow Problem

The unsteady lifting flow problem presented in equations (4.1)-(4.7) is numerically studied using low-order potential boundary element (panel) methods. Briefly, the discretization scheme begins with an appropriate boundary approximation. The next step is to satisfy approximately the boundary conditions on both the body boundary and the trailing wake in their discretized version. On the body boundary, distributions of both sources and dipoles are used, whereas on the trailing wake we only use dipoles. This results in piecewise-constant distribution of the potential on the discretized boundary,

$$\Phi_B(x,y;t) = \Phi_{Bi} \quad \text{i=1,...N}_B \tag{4.18}$$

$$\Phi_W\ (x,y;t) = \ \Phi_{W\ i} = \mu_{Wi} \quad \text{i=1,...N}_W \tag{4.19}$$

Also, for the discretized no-entrance boundary condition we have,

$$\frac{\partial \Phi_B(x,y;t)}{\partial n} = \frac{\partial \Phi_{Bi}}{\partial n} = \left[\vec{V}_B \cdot \vec{n}_B\right]_i = \vec{b}_i \quad \text{i=1,...N}_B \tag{4.20}$$

Finally we assume that the boundary integral equation (BIE) in equation (4.7) is satisfied at the collocation points. For $(x_i, y_i), i = 1,...N_B$ it holds

$$\sum_{j=1}^{N_B}\left(\frac{\delta_{ij}}{2} + B_{ij}\right)\Phi_{Bj} = \sum_{j=1}^{N_B}\left(A_{ij}\right)\underbrace{\left[\mathbf{V}_B \cdot \mathbf{n}_B\right]_j}_{b_j} + \sum_{j=2}^{N_F}\left(-B_{ij}\right)\mu_{Wj} + \left(-B_{i1}\right)\mu_{W1} \tag{4.21}$$

where δ_{ij} is the Kronecker delta and A_{ij}, B_{ij} are induction factors. The term μ_{Wj} approximates the potential jump (dipole intensity) on the trailing wake thus denoting memory effects, while μ_{W1} refers to the potential jump on the wake element that is closest to the trailing edge. In matrix form the above discretized equation can be reformulated as

$$\mathbf{\Phi}_{\mathrm{B}} = \mathbf{D}\cdot\mathbf{b} + \mathbf{P}\cdot\boldsymbol{\mu}_W + \mathbf{Z}\mu_{W1} \tag{4.22}$$

$$\mathbf{P}(\mu_W) = \mathbf{A}^{-1}\left(\mathbf{W}\cdot\boldsymbol{\mu}_W\right), \mathbf{Z} = \mathbf{A}^{-1}\mathbf{W}_K \tag{4.23}$$

where $\mathbf{D} = \mathbf{A}^{-1}\mathbf{S}$ denotes the DtN operator and

$$\mathbf{A} = \left\{\frac{\delta_{ij}}{2} + B_{ij}\right\},\ \mathbf{S} = \left\{A_{ij}\right\},\quad \mathrm{i} \in \{1,...\mathrm{N}_B\},\quad \mathrm{j} \in \{1,...\mathrm{N}_B\}$$

$$\mathbf{W}=\left\{-B_{ik}\right\},\ \mathbf{W}_K=\left\{-B_{i1}\right\},\ i\in\left\{1,...,N_B\right\},\quad k\in\left\{2,...,N_W(t)\right\}$$

The collocation discretization scheme also holds for the non-linear Pressure-type Kutta condition, see also Filippas & Belibassakis (2014), Filippas (2019).

$$\frac{d\left(\Phi_{\mathrm{B,N_B}}-\Phi_{\mathrm{B},1}\right)}{dt}=\mathscr{L}+\mathscr{N} \tag{4.24}$$

$$\mathscr{L}=\frac{\left(\mathbf{g}_1-\mathbf{g}_2\right)\boldsymbol{\tau}_1}{2d_1}\left(\Phi_{\mathrm{B},2}-\Phi_{\mathrm{B},1}\right)-\frac{\left(\mathbf{g}_1+\mathbf{g}_2\right)\boldsymbol{\tau}_{N_B}}{2d_{N_B-1}}\left(\Phi_{\mathrm{B,N_B}}-\Phi_{\mathrm{B},N_B-1}\right)-\frac{\mathbf{g}_1\mathbf{g}_2}{2}-g_3 \tag{4.25}$$

$$\mathscr{N}=-\frac{1}{2}\left[\frac{\boldsymbol{\tau}_{N_B}}{d_{N_B-1}}\left(\Phi_{\mathrm{B,N_B}}-\Phi_{\mathrm{B},N_B-1}\right)+\frac{\boldsymbol{\tau}_1}{d_1}\left(\Phi_{\mathrm{B},2}-\Phi_{\mathrm{B},1}\right)\right]\cdot\left[\frac{\boldsymbol{\tau}_{N_B}}{d_{N_B-1}}\left(\Phi_{\mathrm{B,N_B}}-\Phi_{\mathrm{B},N_B-1}\right)-\frac{\boldsymbol{\tau}_1}{d_1}\left(\Phi_{\mathrm{B},2}-\Phi_{\mathrm{B},1}\right)\right] \tag{4.26}$$

$$\mathbf{g}_1=\left(b\cdot\mathbf{n}\right)_{B,N_B}+\left(b\cdot\mathbf{n}\right)_{B,1}-\mathbf{V}_{B,N_B}-\mathbf{V}_{B,1} \tag{4.27}$$

$$\mathbf{g}_2=\left(b\cdot\mathbf{n}\right)_{B,N_B}-\left(b\cdot\mathbf{n}\right)_{B,1}-\mathbf{V}_{B,N_B}+\mathbf{V}_{B,1} \tag{4.28}$$

$$g_3=\frac{1}{2}\left[\left(\mathbf{V}_{B,1}\right)^2-\left(\mathbf{V}_{B,N_B}\right)^2\right] \tag{4.29}$$

where $\boldsymbol{\tau}$ is the unit tangent vector on the body contour defined in the clockwise direction and d_j is the curvilinear distance between the midpoints of the $\left(j,j+1\right)$ panels.

After the discretization has been performed the solution of the aforementioned lifting flow problem can be obtained using two approaches. At this point, the reader is encouraged to refer to Section 2.3.1 for more details.

The first approach (Section 2.3.1.1) consists of using the BIE as part of a system of equations about the unknown boundary fields $\Phi_B(x,y;t)$ on the body boundary. Using the nonlinear pressure-type Kutta condition (Section 2.2.1) we can construct the complete nonlinear system of equations, with the boundary fields $\Phi_B(x,y;t)$ and μ_{W1} as unknowns. Generally it holds,

$$\mathbf{f}\left(\mathbf{x}\right)=0 \tag{4.30}$$

where $\mathbf{x} = \left[\Phi_{\mathrm{B1}} \ \ldots \ \Phi_{\mathrm{BN_B}} \ \ \mu_{w1}\right]^T$ is the vector containing the unknowns. The solution of this system at each time step of the simulation is approximated using a Newton Raphson method

$$\mathbf{x}_{n+1} = \mathbf{x}_n - \mathbf{J}(\mathbf{x}_n)^{-1}\mathbf{f}(\mathbf{x}_n) \tag{4.31}$$

where $\mathbf{J}(\mathbf{x}_n)^{-1}$ denotes the inverse of the system's Jacobian, which can be analytically calculated for the present formulation.

The second approach (Section 2.3.1.2) uses the DtN operator, derived from the discretized version of the BIE, as a constraint to the dynamical system evolution equations. The latter was constructed using the pressure-type Kutta condition, whereas the dipole intensity μ_{W1} in the vicinity of the trailing wake acts as the dynamic variable. Particularly, the initial value problem (IVP) with respect to the dynamic variable $\mathbf{U} = \mu_{W1}$ is presented below in a more compact notation

$$\frac{d\mathbf{U}}{dt} = \mathbf{f}(\mathbf{U}),\ \mathbf{U}(t_o) = \mathbf{U}_o \tag{4.32}$$

$$\mathbf{f}(\mathbf{U}) = [\frac{-1}{\mathrm{Z}}\frac{d\left(\ Z\ \right)}{dt}]\cdot\mathbf{U} + [\frac{-1}{\mathrm{Z}}\frac{d\left(\ \mathbf{D}\ \cdot\mathbf{b} + \ P\ \right)}{dt}] + [\frac{\mathscr{N}(\mathbf{U}) + \mathscr{L}(\mathbf{U})}{\mathrm{Z}}] \tag{4.33}$$

where $\mathbf{f}(\mathbf{U})$ denotes a vector function.

In the present study, the numerical solution of (4.32)-(4.33) is obtained using a higher-order Adams-Bashford-Moulton (A.B.M.) scheme, see Longuet-Higgins & Cokelet (1975) as well as Filippas & Belibassakis (2014). The time derivative terms $d\left(\ Z\ \right)/dt$, $d\left(\ \mathbf{D}\ \cdot\mathbf{b} + \ P\ \right)/dt$ in equation (4.33) can be approximated numerically with a finite difference scheme. Furthermore, with $\mathbf{U}(t)$ known at time step t, the corrector step is the following,

$$\mathbf{U}(t+\Delta t) = \mathbf{U}(t) + \frac{\Delta t}{24}[9\mathbf{f}_{pre}(t+\Delta t) + 19\mathbf{f}(t) - 5\mathbf{f}(t-\Delta t) + \mathbf{f}(t-2\Delta t)] \tag{4.34}$$

with predictor step

$$\mathbf{f}_{pre}(t+\Delta t) = \mathbf{f}_{t+\Delta t}\left(\mathbf{U}_{pre}(t+\Delta t)\right) \tag{4.35}$$

$$\mathbf{U}_{pre}(t+\Delta t) = \mathbf{U}(t) + \frac{\Delta t}{24}[55\mathbf{f}(t) - 59\mathbf{f}(t-\Delta t) + 37\mathbf{f}(t-2\Delta t) - 9\mathbf{f}(t-3\Delta t)] \tag{4.36}$$

4.2.2 Discretization Scheme for the Structural Problem

Re-arranging the terms in equation (4.10) yields

$$m(x)\partial_t^2 w_o(x;t) + \partial_x^2[D(x)\partial_x^2 w_o(x;t)] + m(x)w_o(x;t)\cdot\dot{\theta}^2(t) = q_{Total}(x;t) \tag{4.37}$$

$$q_{Total}(x;t) = q_{Hydro}(x;t) - m(x)\left(x\cdot\ddot{\theta}(t) + \ddot{h}(t)\cos\theta(t)\right) \tag{4.38}$$

Next, the equivalent weak formulation of the IBVP is derived for the implementation of the FEM. After the semi-discretization of the system of equation using Galerkin approximation methods, the **hp-FEM discretization** is performed. More details about this methodology are presented in Chapter 3.

Especially for the coupled problem, the local matrices are given by the following expressions,

$$\mathbf{M}_{loc} = \left(a(H_i^e, H_j^e)\right)_{1\le i,j\le n} = \int_{\Omega^h} m(x)H_i^e(x)H_j^e(x)dx = \int_{e(\Omega^h)} m(x)H_i(x)H_j(x)dx \tag{4.39}$$

$$\begin{aligned}\mathbf{K}_{loc} &= \left(b(H_i^e, H_j^e)\right)_{1\le i,j\le n} = \\ &\int_{\Omega^h} D(x)\partial_{xx}H_i^e(x)\partial_{xx}H_j^e(x)dx + \int_{\Omega^h} m(x)H_i^e(x)H_j^e(x)\dot{\theta}^2(t)dx = \\ &= \int_{e(\Omega^h)} D(x)\partial_{xx}H_i(x)\partial_{xx}H_j(x)dx + \int_{e(\Omega^h)} m(x)H_i(x)H_j(x)\dot{\theta}^2(t)dx\end{aligned} \tag{4.40}$$

$$\begin{aligned}\mathbf{f}_{loc} &= \left(f(H_j^e)\right)_{1\le j\le n} = \int_{\Omega^h} H_j^e(x)q_{Total}(x,t)dx = \int_{e(\Omega^h)} H_j(x)q_{Total}(x,t)dx \\ &= \int_{e(\Omega^h)} H_j(x)q_{Hydro}(x;t)dx + \int_{e(\Omega^h)} H_j(x)\left[-m(x)\left(x\cdot\ddot{\theta}(t) + \ddot{h}(t)\cos\theta(t)\right)\right]dx\end{aligned} \tag{4.41}$$

$$U\big|_e = \left(u_i^e\right)_{1\le i\le n} \tag{4.42}$$

where $\mathbf{M_{loc}} \in \mathbb{R}^{n\times n}$ and, $\mathbf{K_{loc}} \in \mathbb{R}^{n\times n}$ stand for the local element mass and stiffness matrices respectively, $\mathbf{f}_{loc} \in \mathbb{R}^n$ for the local load vector and $U\big|_e \in \mathbb{R}^n$ for the vector containing the nodal unknowns for interval I_e.

In this formulation, the foil undergoes prescribed heaving $h(t)$ and pitching $\theta(t)$ motions and thus the term $\int_{e(\Omega^h)} m(x)H_i(x)H_j(x)\dot{\theta}^2(t)dx$ appearing (4.39) as well as the term containing the influence of non-inertial phenomena in the forcing vector in (4.41) $\int_{e(\Omega^h)} H_j(x)\left[-m(x)\left(x\cdot\ddot{\theta}(t) + \ddot{h}(t)\cos\theta(t)\right)\right]dx$ can be calculated at each time step of the simulation. The first integral in the loading vector however, contains the hydrodynamic pressure forces which are dependent on the structural response of the foil and vice versa.

The next important step in this process is the *assembly* of the inner product terms, to construct the *global matrices.* The addition of proportional damping terms $a_1, a_2 \in \mathbb{R}$ yields the extended global equation, which is in fact a system of second order differential equations with initial conditions. By performing order reduction and introducing matrix notation we derive the following system of first order nonlinear differential equations,

$$\mathbf{A}\cdot\dot{\mathbf{w}} = \mathbf{B}\cdot\mathbf{w} + \mathbf{Q},\ \mathbf{w} = \left[\mathbf{w}_o \quad \dot{\mathbf{w}}_o\right]^T \tag{4.43}$$

where $\mathbf{A} = \begin{bmatrix} \mathbf{0} & \mathbf{M}_{glob} \\ \mathbf{I} & \mathbf{0} \end{bmatrix}$, $\mathbf{B} = -\begin{bmatrix} \mathbf{K}_{glob} & \mathbf{C} \\ \mathbf{0} & -\mathbf{I} \end{bmatrix}$, $\mathbf{Q} = \begin{bmatrix} \mathbf{F}_{glob} \\ \mathbf{0} \end{bmatrix}$, $\mathbf{C} = a_1\mathbf{K}_{glob} + a_2\mathbf{M}_{glob}$ the damping matrix and $\mathbf{I}$ is the identity matrix known from linear algebra. It is noted, that the stiffness and force matrices are time-dependent in this formulation due to the time-dependence of the pressure field and the non-inertial effects.

4.2 Coupled BEM-FEM Numerical Scheme

Having presented the formulation of a flapping foil possessing chord-wise flexibility, we devise a method to solve the coupled equations of the foil's dynamic response as a flexible thin plate. The Crank-Nicolson time-marching scheme is implemented for the integration of the structural equation (4.37). Therefore,

$$\mathbf{A}\cdot\left(\frac{\mathbf{w}_n - \mathbf{w}_{n-1}}{\Delta t}\right) = \frac{1}{2}\left(\mathbf{B}\cdot\mathbf{w}_n + \mathbf{Q}_n\right) + \frac{1}{2}\left(\mathbf{B}\cdot\mathbf{w}_{n-1} + \mathbf{Q}_{n-1}\right) \Rightarrow$$

$$\left(\mathbf{A} - \frac{1}{2}\Delta t\cdot\mathbf{B}\right)\cdot\mathbf{w}_n = \left(\mathbf{A} + \frac{1}{2}\Delta t\cdot\mathbf{B}\right)\mathbf{w}_{n-1} + \frac{1}{2}\Delta t\cdot\left(\mathbf{Q}_{n-1} + \mathbf{Q}_n\right) \tag{4.44}$$

where $\mathbf{w}_{n-1} = \left[\boldsymbol{\eta}_{n-1}, \mathbf{u}_{n-1}\right]$ denotes the solution vector at time step $n-1$, comprised of the nodal deflection and slope, while $\mathbf{Q}_{n-1}, \mathbf{Q}_n$ are the loading vectors.

The above has been discussed previously in Chapter 3, however in this section emphasis will be given to the loading vectors. If the loading vectors were known at each time step, the system of the above equations could be considered linear. Matrix $[\mathbf{A} - 1/2\Delta t\mathbf{B}]$ is non-singular and the solution could therefore be given from equation (4.44). However a hidden difficulty lies in the fact that the loading term in the current time step $\mathbf{Q}_n$ is not explicitly known and is also influenced by the deflection and slope response of the thin elastic plate. This implicit non-linearity is treated with an iterative scheme that considers the system of equations above to be in fact non-linear. We aim to solve the following

$$\left(\mathbf{A}-\frac{1}{2}\Delta t\cdot\mathbf{B}\right)\cdot\mathbf{w}_n-\left(\mathbf{A}+\frac{1}{2}\Delta t\cdot\mathbf{B}\right)\mathbf{w}_{n-1}-\frac{1}{2}\Delta t\cdot\left(\mathbf{Q}_{n-1}+\mathbf{Q}_n\right)=0 \tag{4.45}$$

or, in a more compact form

$$\mathbf{G}\left(\mathbf{w}_n\right)=\left(\mathbf{A}-\frac{1}{2}\Delta t\cdot\mathbf{B}\right)\cdot\mathbf{w}_n-\left(\mathbf{A}+\frac{1}{2}\Delta t\cdot\mathbf{B}\right)\mathbf{w}_{n-1}-\frac{1}{2}\Delta t\cdot\left(\mathbf{Q}_{n-1}+\mathbf{Q}_n\right) \tag{4.46}$$

while setting the residual expression to vanish, as in

$$\mathbf{G}\left(\mathbf{w}_n\right)=0 \tag{4.47}$$

For the solution of equation (4.47) we use the Newton-Raphson method. Upon choice of an initial guess $\mathbf{w}_n^0$ we successively approximate the unknown vector with the formula below

$$\mathbf{w}_n^q=\mathbf{w}_n^{q-1}-\mathbf{J}^{-1}\left(\mathbf{w}_n^{q-1}\right)\cdot\mathbf{G}\left(\mathbf{w}_n^{q-1}\right)\qquad q=1,2,... \tag{4.48}$$

The matrix $\mathbf{J}$ is the Jacobian of the function $\mathbf{G}:\mathbb{R}^{2N}\to\mathbb{R}^{2N}$ defined as

$$\mathbf{J}\left(\mathbf{w}\right)=\begin{bmatrix}\frac{\partial G_1}{\partial w_1} & \frac{\partial G_1}{\partial w_2} & \cdots & \frac{\partial G_1}{\partial w_{2N}}\\ \frac{\partial G_2}{\partial w_1} & \frac{\partial G_2}{\partial w_2} & \cdots & \frac{\partial G_2}{\partial w_{2N}}\\ \vdots & \ddots & & \\ \frac{\partial G_{2N}}{\partial w_1} & \frac{\partial G_{2N}}{\partial w_2} & \cdots & \frac{\partial G_{2N}}{\partial w_{2N}}\end{bmatrix} \tag{4.49}$$

where $\mathbf{G}\left(\mathbf{w}\right)=\left[G_1\left(\mathbf{w}\right),G_2\left(\mathbf{w}\right),...,G_{2N}\left(\mathbf{w}\right)\right]^T$.

The calculation of the Jacobian matrix requires knowledge of the partial derivatives of the scalar components $G_i\left(\mathbf{w}\right), i=1,...,2N_B$ of the function $\mathbf{G}\left(\mathbf{w}\right)$. This is not possible, however, since we do not have knowledge of the explicit dependence of $\mathbf{G}\left(\mathbf{w}\right)$ on the vector $\mathbf{w}$. Thus we resort to numerical approximation of the partial derivatives. Using the central differences scheme, we calculate

$$\frac{\partial G_i}{\partial w_j}\approx\frac{G_i\left(w_j+h_j\right)-G_i\left(w_j-h_j\right)}{2h_j} \tag{4.50}$$

where h_j is sufficiently small. In practice h_j is selected as a small percentage of $|w_j|$. Therefore, by defining a perturbation vector $\mathbf{h}_n^q = \left[h_1^q , h_2^q ,..., h_{2N}^q \right]^T$ we have

$$\mathbf{J}\left(\mathbf{w}_n^q\right) \approx \frac{\mathbf{G}\left(\mathbf{w}_n^q + \mathbf{h}_n^q\right) - \mathbf{G}\left(\mathbf{w}_n^q - \mathbf{h}_n^q\right)}{2\mathbf{h}_n^q} \tag{4.51}$$

The proposed BEM-FEM coupled scheme is described below and presented schematically in Figure 4.2.

- When the hydro-elastic coupling method proceeds to a new time step, the BEM solver is called using information from the previous step $\mathbf{w}_n^0 = \mathbf{w}_{n-1}$. In that sense, data flows from one solver to another (1) to approximate the deformed state of the camber line, based on which the body boundary geometry is generated and (2) to modify the no-entrance boundary condition.
- The solution of the hydrodynamic problem gives a first approximation for the loading vector at the current time step $\mathbf{Q}_n^0$.
- We proceed by applying an implicit time integration scheme (e.g. implicit Euler method) to approximate the solution vector for the structural problem, thus $\mathbf{w}_n^1$ is obtained as our initial guess.
- Starting with this initial guess we perform the iterative procedure based on the above Crank–Nicolson time integration scheme using the Newton-Raphson method. A criterion is established in order to examine the convergence of the iterative procedure. During intermediate iterations, the BEM solver is called to re-evaluate the loading vector based on new approximations concerning the deformations.
- When the iterative procedure has converged to the solution, we obtain the vector containing the nodal deflection and slope response.

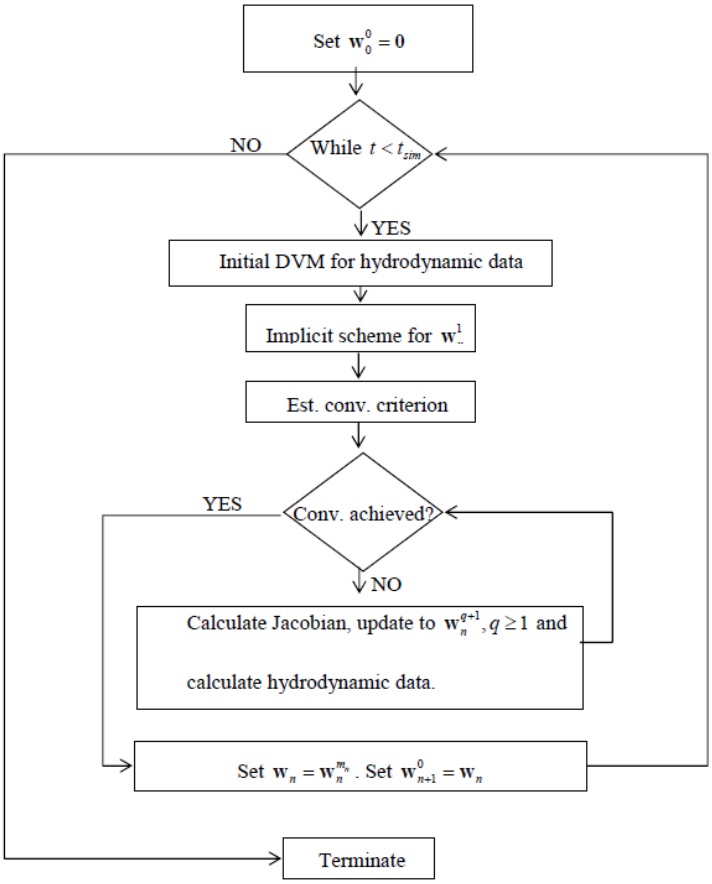

Figure 4.2 Flowchart of the BEM-FEM coupling algorithm, derived from Priovolos et al. (2018)

Various criterions can be established to monitor the convergence of the iterative procedure to the approximate solution at each time step. In the present work, we introduce the following matrix containing the terms found in equation (4.46), as

$$\mathbf{T} = \left[\left(\mathbf{A} - \frac{1}{2}\Delta t \cdot \mathbf{B} \right) \cdot \mathbf{w}_n,\ -\left(\mathbf{A} + \frac{1}{2}\Delta t \cdot \mathbf{B} \right) \cdot \mathbf{w}_{n-1},\ -\frac{1}{2}\Delta t \cdot \mathbf{Q}_{n-1},\ -\frac{1}{2}\Delta t \cdot \mathbf{Q}_n \right] \tag{4.52}$$

with $\mathbf{w}_n$ and $\mathbf{Q}_n$ re-evaluated at intermediate iterations. Then we introduce,

$$crit = \lambda \cdot 4 \max|\mathbf{T}|, \qquad \lambda > 0 \tag{4.53}$$

with $\lambda = 10^{-3}$ as an example. Finally, we presented the expression that is used to terminate each intermediate iteration loop as,

$$\max\left|\mathbf{G}\left(\mathbf{w}_n\right)\right| < crit \tag{4.54}$$

4.3 Numerical Results

4.3.1 Flapping-Foil with Prescribed Deformations

To illustrate the capabilities of the extended BEM numerical scheme to treat flapping-foils with prescribed deformations as well as the results that can be obtained with the developed hp-FEM we examine the structural response of a NACA0012 foil with flexural rigidity profile variation under distributed load.

The time history of forcing is derived from the results of a case study for rigid flapping foils in propulsion mode, using the BEM solver presented in Chapter 2. The structural response of the foil is predicted here using the FEM solver with the time history of the distributed load is known a priori, as it has been obtained from simulation with the BEM solver. To what extent such simple simulations are able to reproduce results that resemble the fluid-structure interaction of biomimetic systems is an interesting topic for research. However, realistic solution approximations for a range of various design parameters, can only be obtained using fully coupled numerical models.

For the hydrodynamics we consider a NACA0012 shaped foil with the centre of rotation located at the $1/3c$ of the chord length $c = 0.1\,\text{m}$ that undergoes a combined heaving and pitching flapping motion. The non-dimensional heaving amplitude is $ho/c = 0.75$, the pitching amplitude is $\theta o = 10^o$, the phase difference is $\varphi = -90^o$, Strouhal number is $Str = 0.3$ and the forward velocity $U = 0.2\,m/s$. The fluid density is assumed to be $\rho = 1000\ \text{kg/m}^3$. The discretization in space and time employed $N_B = 120$ panels and $TSR = 0.05$ respectively. The structural member has a material density $1200\ \text{kg/m}^3$, Young's modulus $E = 2\times10^5\ \text{N/m}^2$ and Poisson's ratio $v = 0.5$. The mesh consisted of $N_{elem} = 100$ elements with $N_{nodes} = 3$.

The time history of the non-dimensional pressure coefficient C_p on the body boundary and the corresponding pressure difference chord-wise $\Delta C_p \times (1/2\rho U^2 c)$ for the two periods after the solution has converged are presented in Figures 4.3 and 4.4 respectively. These results were obtained using the BEM solver from Chapter 2, aiming for the latter to be used as the forcing term for the structural problem Note that, at the trailing edge the pressure difference is almost equal to zero, which is a results of the enforcement of the pressure-type Kutta condition.

The FEM solution yields approximations for the the nodal unknowns of the transverse displacement on the mid-plane w_o^h, the rotation of the normal to the mid-plane about y-axis $\partial_x w_o^h$ as well as their time derivatives $\partial_t w_o^h$ and $\partial_t(\partial_x w_o^h)$. The time histories of

these quantities are presented in Figures 4.5 – 4.8. These results are in accordance with the boundary conditions of Case 2 from Section 3.2, in which the pivot point of the foil remains clamped.

Finally, the results obtained from the structural problem, and more specifically the transverse displacement and slope time histories, account for the prescribed deformations in this study case. The effects of flexibility on the instantaneous force and moment coefficients are shown in Figure 4.9.

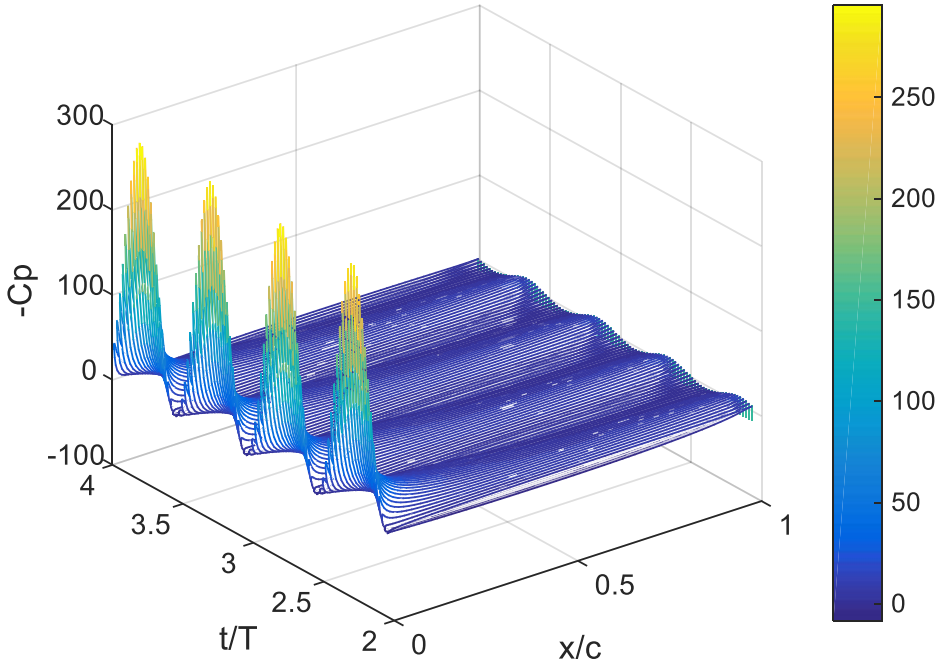

Figure 4.3 Time history of the pressure coefficient C_p, concerning the flapping motion of a foil with $ho/c = 0.75$, $\theta o = 10^o$, $\varphi = -90^o$, $Str = 0.3$ and $U = 0.2\ m/s$ for a mesh of $N_B = 120$ panels and $TSR = 0.05$

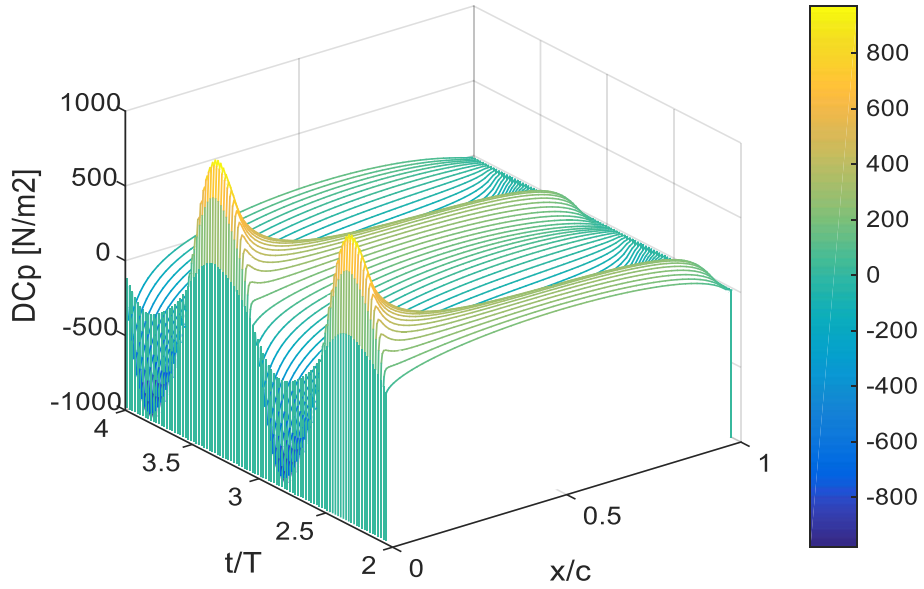

Figure 4.4 Time history of the pressure difference $\Delta C_p \times (1/2\rho U^2 c)$, concerning the flapping motion of a foil with $ho/c = 0.75$, $\theta o = 10^o$, $\varphi = -90^o$, $Str = 0.3$ and $U = 0.2\ m/s$ for a mesh of $N_B = 120$ panels and $TSR = 0.05$.

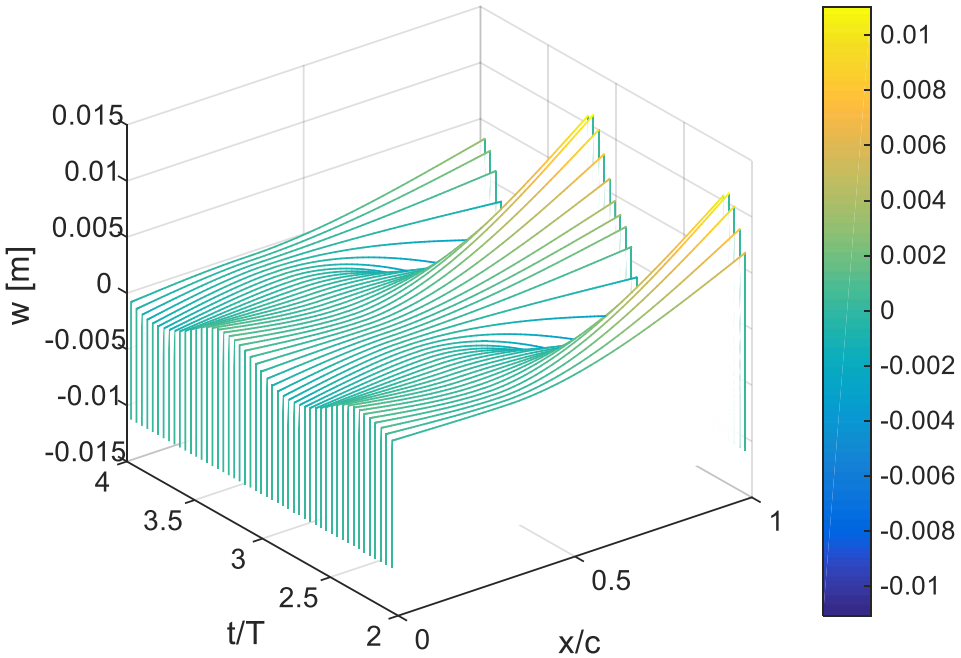

Figure 4.5 Time history of w_o^h for a material density $1200\ \mathrm{kg/m^3}$, Young's modulus $E = 2\times10^5\ \mathrm{N/m^2}$ and Poisson's ratio $v = 0.5$.

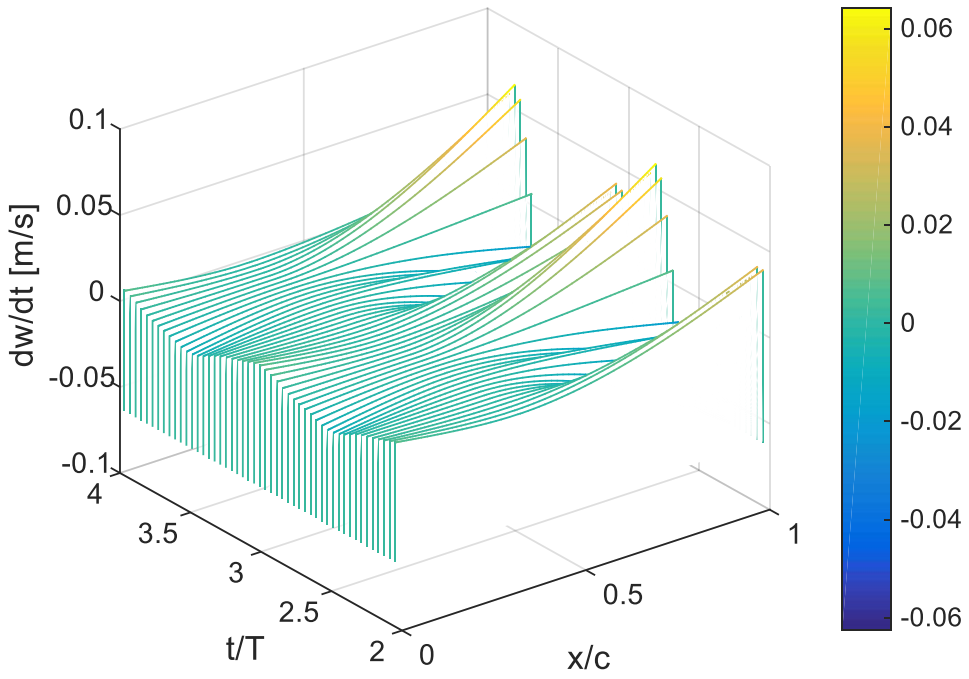

Figure 4.6 Time history of $\partial_t w_o^h$ for a material density $1200\ \mathrm{kg/m^3}$, Young's modulus $E = 2\times10^5\ \mathrm{N/m^2}$ and Poisson's ratio $v = 0.5$.

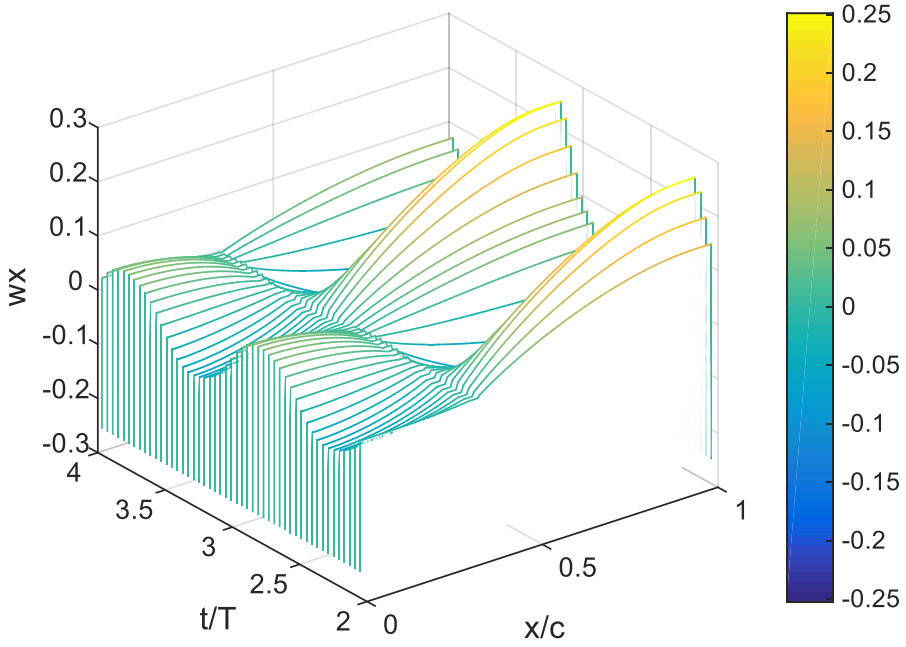

Figure 4.7 Time history of $\partial_x w_o^h$ for a material density $1200\ \mathrm{kg/m^3}$, Young's modulus $E = 2\times10^5\ \mathrm{N/m^2}$ and Poisson's ratio $v = 0.5$.

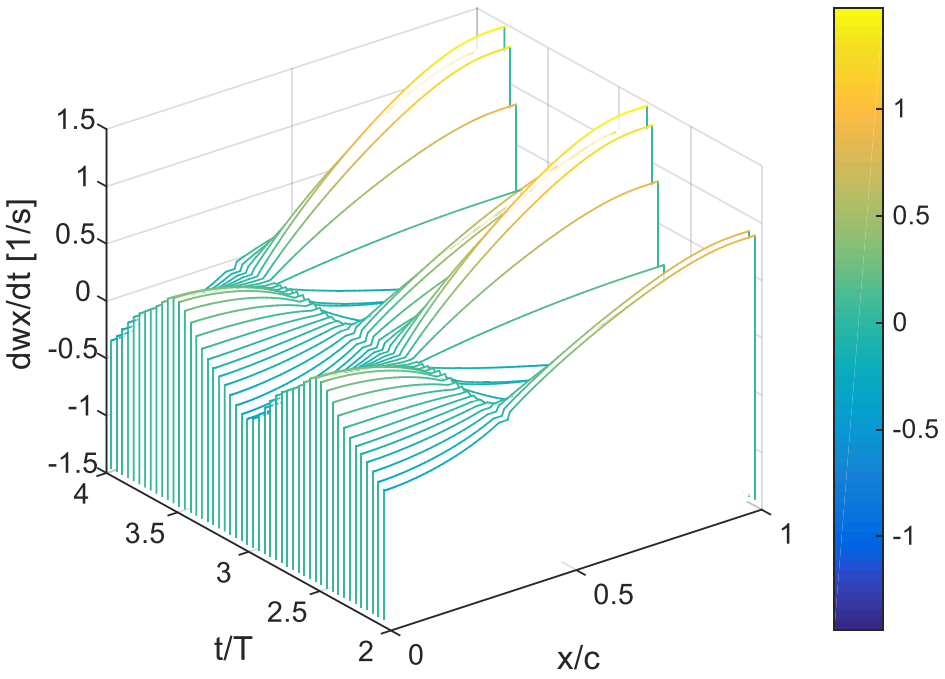

Figure 4.8 Time history of $\partial_t(\partial_x w_o^h)$ for a material density $1200\ \mathrm{kg/m^3}$, Young's modulus $E = 2\times10^5\ \mathrm{N/m^2}$ and Poisson's ratio $v = 0.5$

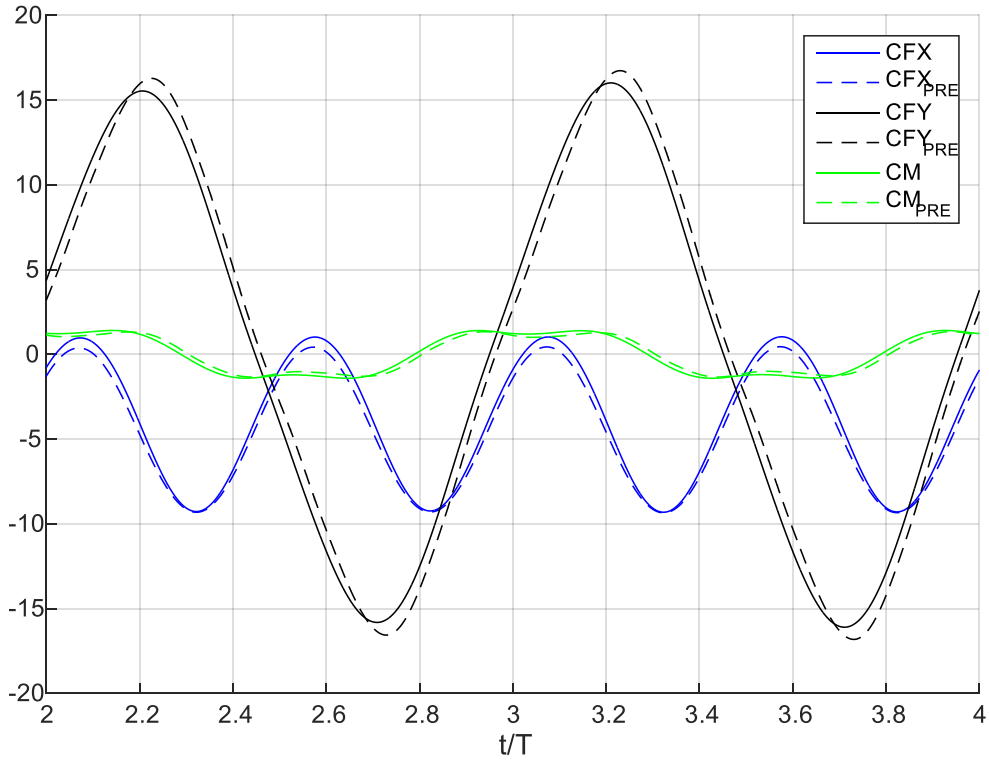

Figure 4.9 Time history of force and moment coefficients for the case of a rigid foil (solid lines) and a foil with prescribed deformations (dashed line)

4.3.2 Validation of the Coupled BEM-FEM Numerical Scheme

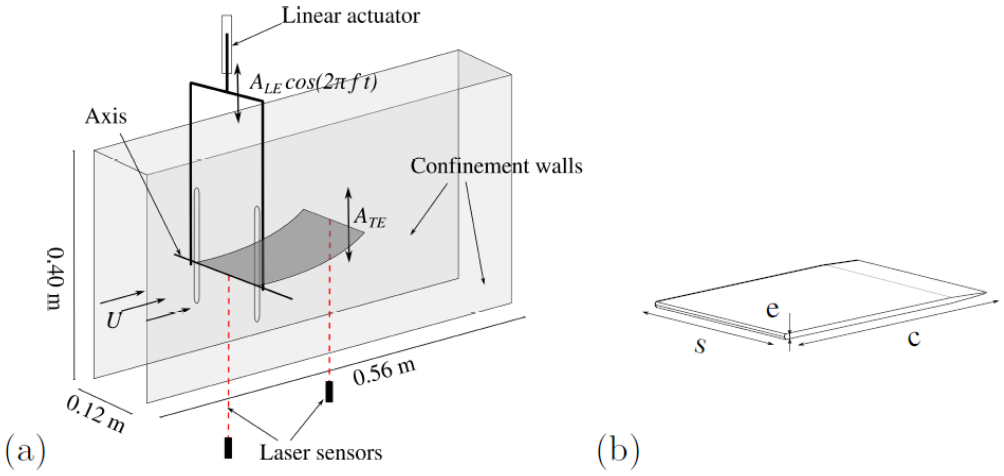

Figure 4.10 Schematic representation the experimental set up (a) and of the flexible plate (b) derived from Paraz et al. (2014)

A fundamental aspect of this work is to illustrate the ability of the proposed coupled BEM-FEM to capture the main hydro-elastic effects of chord-wise flexible flapping foils. In this section, we present numerical results simulating an experimental case studied in the work of Paraz et al (2014), for which also analytical predictions were made in the most recent work by Paraz, Schouveiler, & Eloy (2016).

The numerical method presented here is based on the second approach to the problem solution (see Section 2.3.1.2), employing the **Adams-Bashford linear multistep method** for the lifting flow problem, which is less computationally demanding when compared to the first approach (see Section 2.3.1.1).

The experiments considered flexible plates of chord length $c = 0.12\ m$ under enforced heaving motions, actuated at the leading edge (LE) for a frequency range of $0.2 - 8$ Hz. The schematic representation of the experimental set up is shown in Figure 4.3. We also performed simulations by means of the proposed BEM-FEM numerical scheme to predict the structural response of the trailing edge (TE) for:

- trailing edge heaving amplitude $A_{LE} = 0.004$ m
- constant flexural rigidity $D = 0.018$ Nm
- free stream velocity $U_\infty = 0.05$ m/s that corresponds to $\mathrm{Re} = 6000$
- fundamental frequency of the structure immersed in fluid $f_o = 0.75$ Hz

The damped structural response of the foil is modelled using proportional damping terms, which were calculated using the natural frequencies of the foil in vacuo. The results obtained are presented in Figure 4.4 against the experimental data published in Paraz et al. (2014). The numerical parameters consisted of $N_{bem}=100$ panel elements, $N_{fem}=35$ Hermite quintic finite and $dt/T=0.005$ for the time discretization with T being the period of the enforced motion. For the **unsteady lifting flow problem** the foil was modelled as a NACA 0004, whereas, considering its elastic deformations, the foil was modelled as a thin plate with constant thickness of $h=0.004$ m.

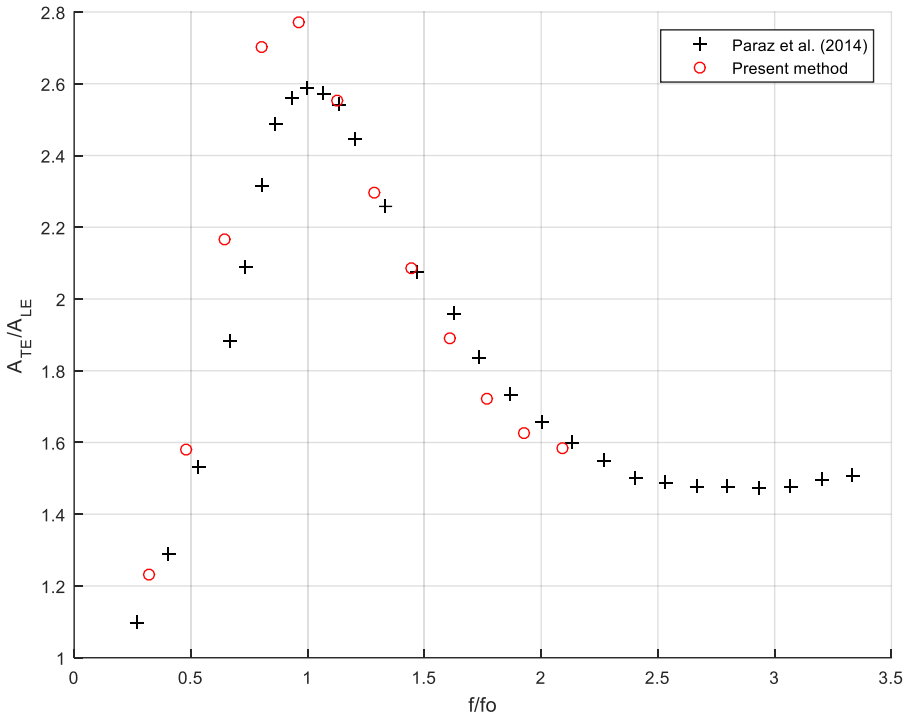

Figure 4.11 Heaving flexible plate response and comparison with Paraz et al. (2014).

As seen in Figure 4.11, satisfactory agreement is found between the experimental and numerical data, regarding the appearance of the peak at $f/f_o=1$ amplitude and the overall shape of the response curve. The small differences concerning the peak values of the structural response, that are overestimated with the present method, could be attributed to the non-linear vortex-wake dynamics or non-linear damping effects that are not modeled in the present work. It is also noted that the fictitious forces were not taken into account during the simulations and therefore it is left as a future task to examine their effect on the structural response of the foil.

It was also observed that as the forcing frequency f increased the pressure difference at the trailing edge required finer discretization in time to be minimized. Nevertheless,

even with increased values of the pressure difference at the TE the results were in good agreement with the experiment.

Also, in the work of Paraz, Schouveiler, & Eloy (2016). it is highlighted that the structural response of the heaving chord-wise flexible flat plate can be predicted using a linearized Euler-Bernoulli beam equation that includes non-linear damping terms with emphasis on the transverse drag terms. However, the proposed coupled BEM-FEM numerical scheme is able to predict reasonably well the structural response of the TE using only proportional damping terms.

In order to gain more insight into the fluid-structure interaction modelling we present results for $f / f_o = 0.3,\ 1,\ 1.5$ concerning

- the time history of the trailing edge (TE) along with time histories of the leading edge motion (LE) and the transverse displacement (Fig. 4.12-4.14)
- the time history of the chord-wise pressure distribution to verify the satisfaction of the pressure-type Kutta condition (Fig. 4.15-4.17)
- the envelope of the foil's deflection (Fig. 4.18-4.20) in the inertial reference frame

The enforced motion of the leading edge is represented with a dashed line in Figures 4.12, 4.13 & 4.14, whereas with a blue line we represent the transverse displacement time history that was obtained from the BEM-FEM coupled numerical scheme. The transverse displacement is expressed with respect to the non-inertial body-fixed reference frame fixed at the foil's leading edge with no inclination. Therefore, the overall response of the trailing edge in the inertial reference frame is given as a superposition of the leading edge motion with the transverse displacement.

We observe that increased transverse displacement amplitudes come with increased values of the forcing frequency. However, due to the modified no-entrance boundary condition in equation (4.7) and the coupling scheme that is implemented a phase lag between the leading edge motion and transverse displacement is observed. Due to this phase lag we are able to predict the peak in the structural response of the TE, see Figure 4.11.

Regarding the chord-wise pressure difference, the time history presented in Figure 4.15 for the smallest ratio between the forcing frequency and the first resonance of the systems, $f / f_o = 0.3$, shows trends similar to those found in modelling rigid flapping foils. Also, the pressure difference at the trailing edge is close to zero, indicating that the chosen mesh leads to the satisfaction of the imposed pressure-type Kutta condition. However, that is not the case for the simulations depicted in Figure 4.16 & 4.17. Particularly chord-wise pressure distribution for $f / f_o = 1.5$ is strongly

influenced by the no-entrance boundary condition containing the deflection velocity and leads to the interesting deflection envelope in Figure 4.20.

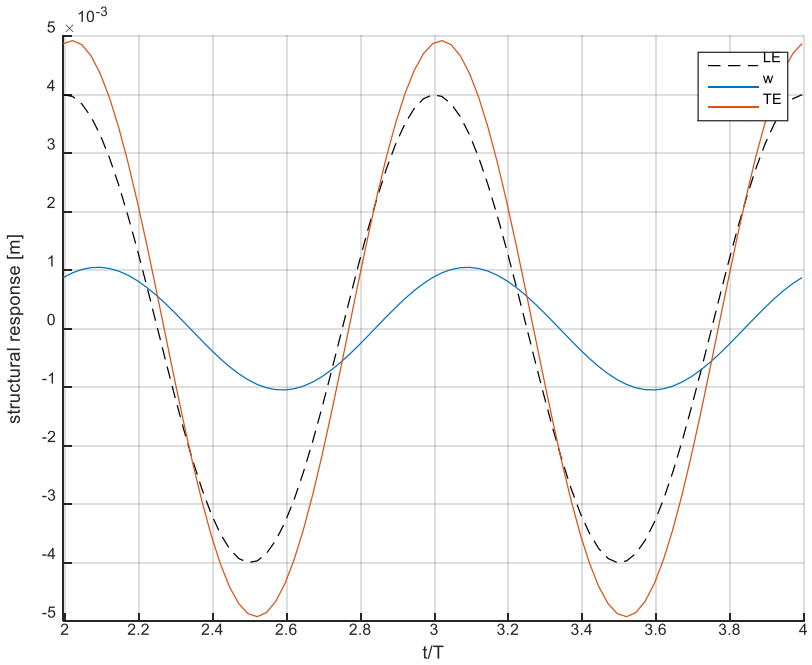

Figure 4.12 Time history of the leading edge enforced motion (dashed line), the trailing edge response (red line) and the transverse displacement of the camber line (black line) for $f / f_o = 0.3$.

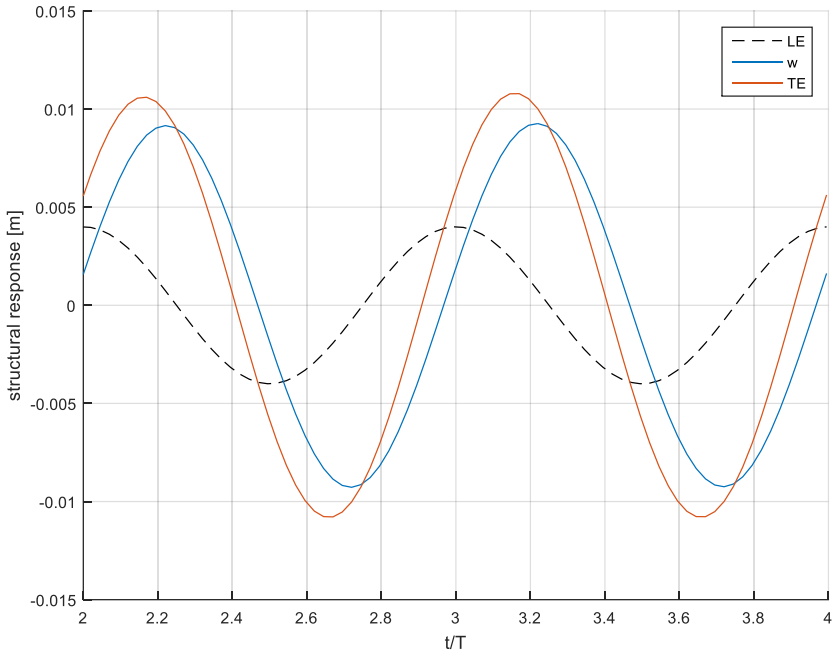

Figure 4.13 Time history of the leading edge enforced motion (dashed line), the trailing edge response (red line) and the transverse displacement of the camber line (black line) for $f / f_o = 1$.

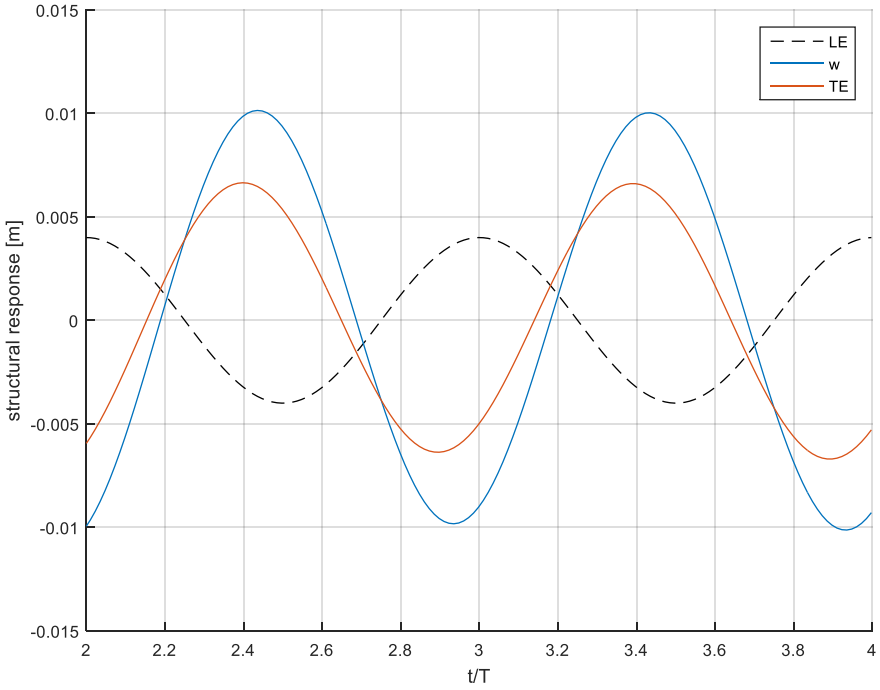

Figure 4.14 Time history of the leading edge enforced motion (dashed line), the trailing edge response (red line) and the transverse displacement of the camber line (black line) for $f / f_o = 1$

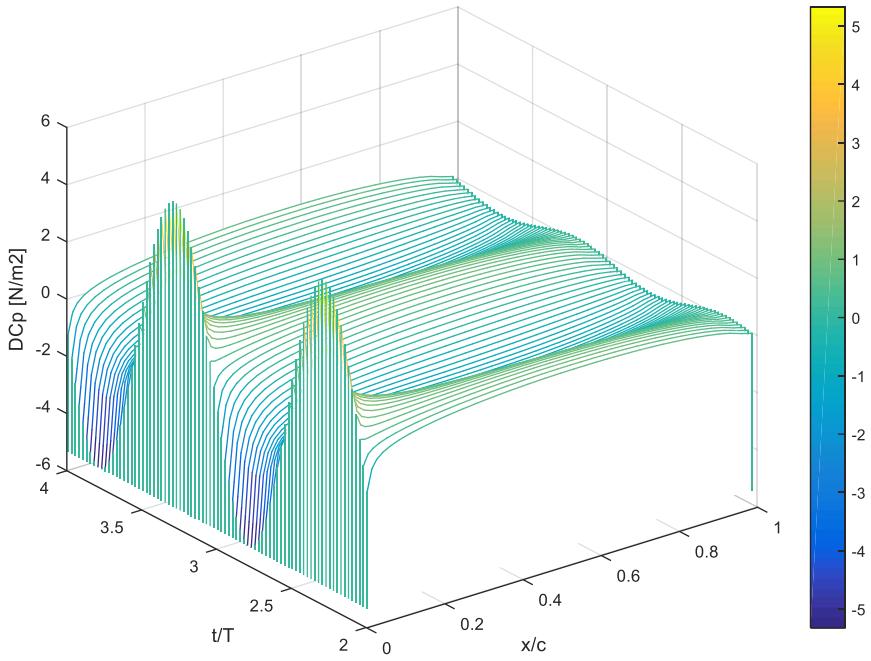

Figure 4.15 Time history of the chord-wise pressure difference for $f / f_o = 0.3$.

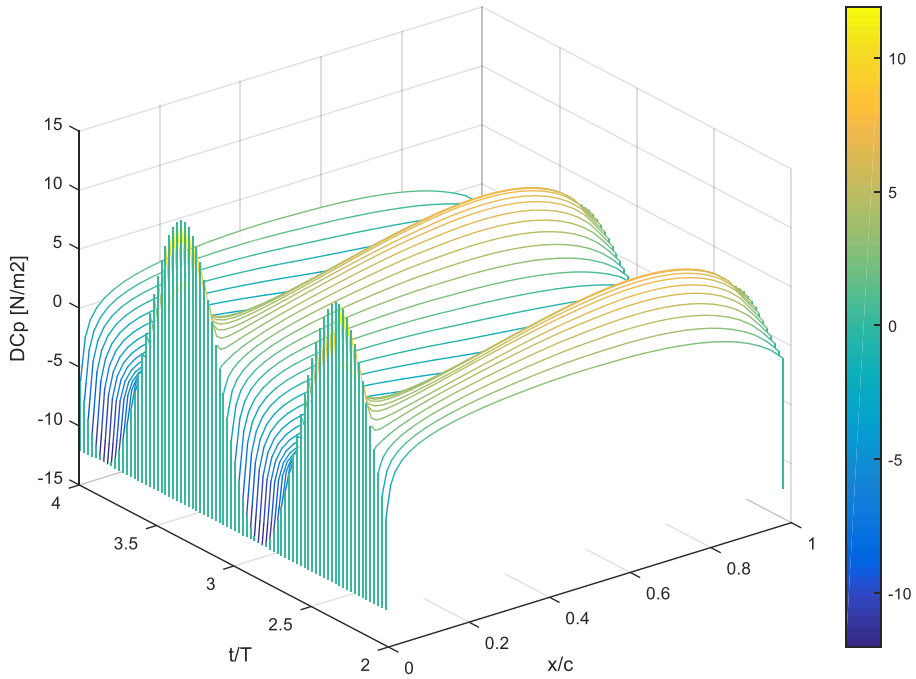

Figure 4.16 Time history of the chord-wise pressure difference for $f / f_o = 1$.

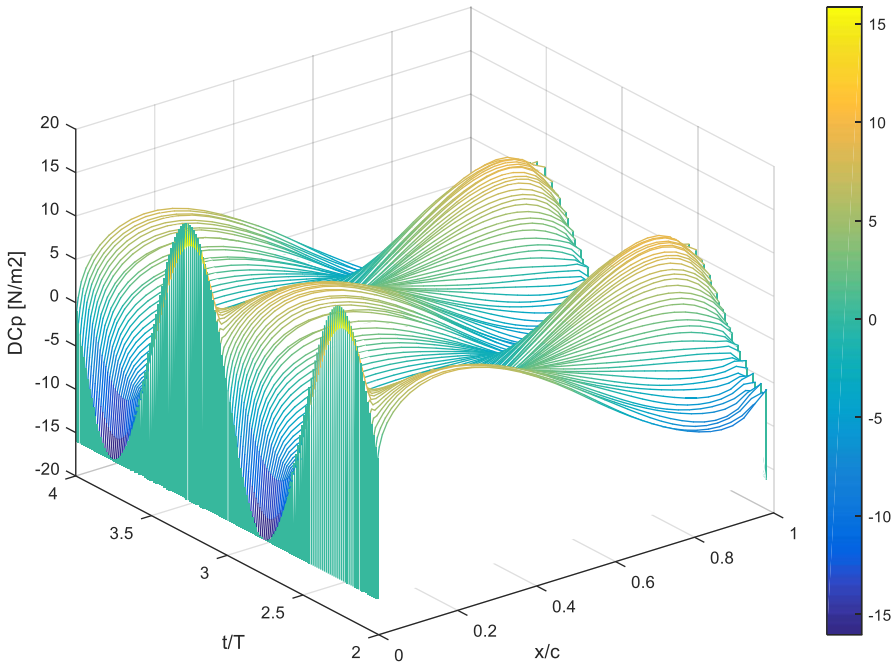

Figure 4.17 Time history of the chord-wise pressure difference for $f / f_o = 1.5$.

Additional interesting results that can be produced by the present method are the deflection envelopes of the foil in the inertial reference frame. These represent the enveloped structural responses that an observer outside the towing tank in the experiments performed by Paraz et al. would witness. In Figure 4.18 the transverse displacement of the foil's camber line is small compared to the chord length. The deflection envelopes in Figures 4.19 & 4.20 display a far more interesting behavior and are also found in good agreement with the analytical results presented in the work of Paraz et al (2016).

These deflection envelopes are slightly different from the ones observed experimentally in the work of Paraz et al. (2014). It has been suggested, that fluid-structure interaction models that account for large deformations would produce better approximations regarding the structural response of such systems. Motivated by this, extension of the current FEM for large deformation modelling is proposed for future work.

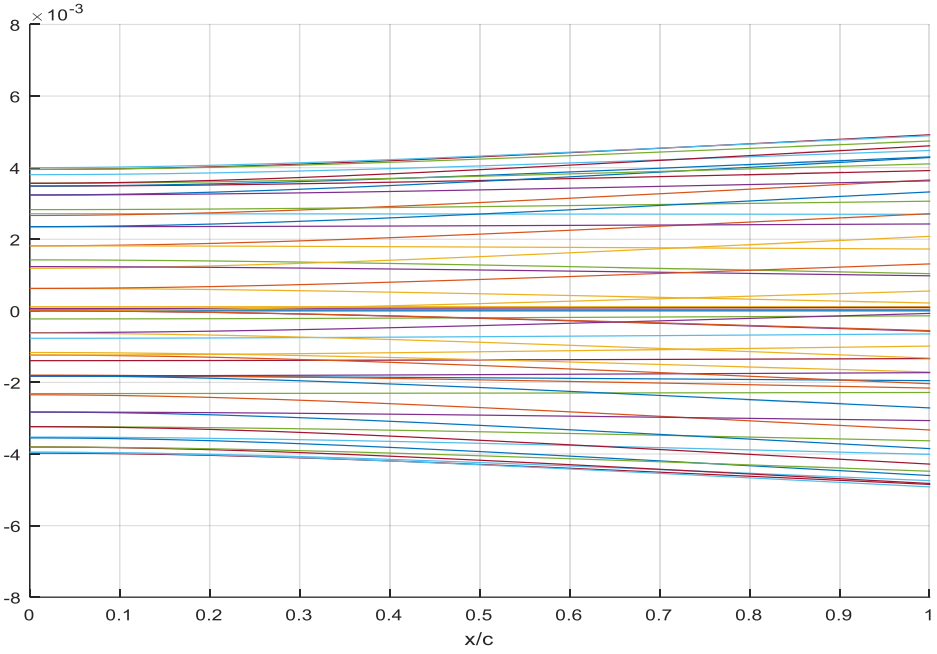

Figure 4.18 Envelope for $f / f_o = 0.3$

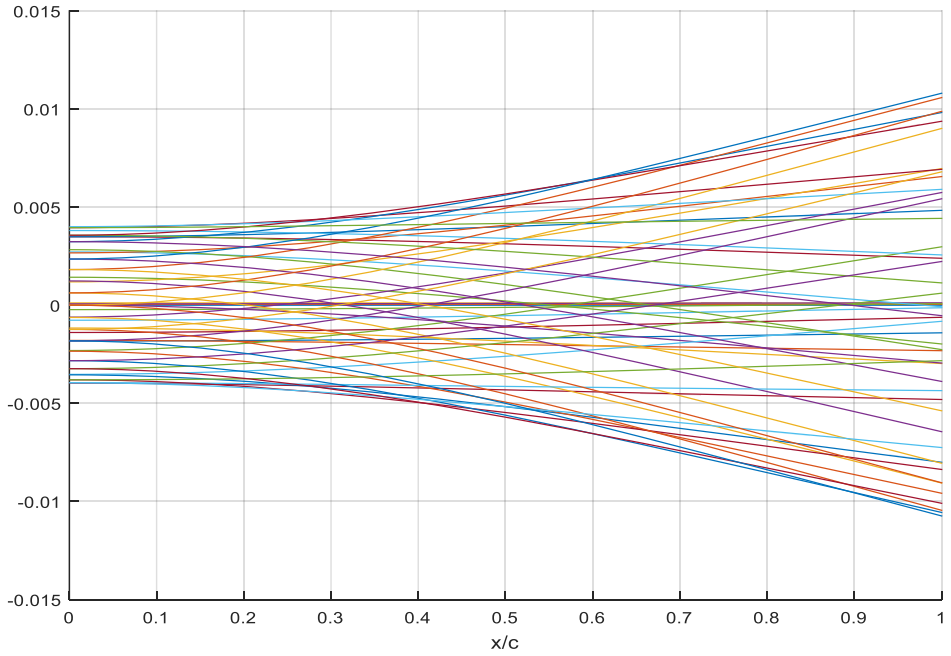

Figure 4.19 Deflection envelope during the last period of motion for $f / f_o = 1$

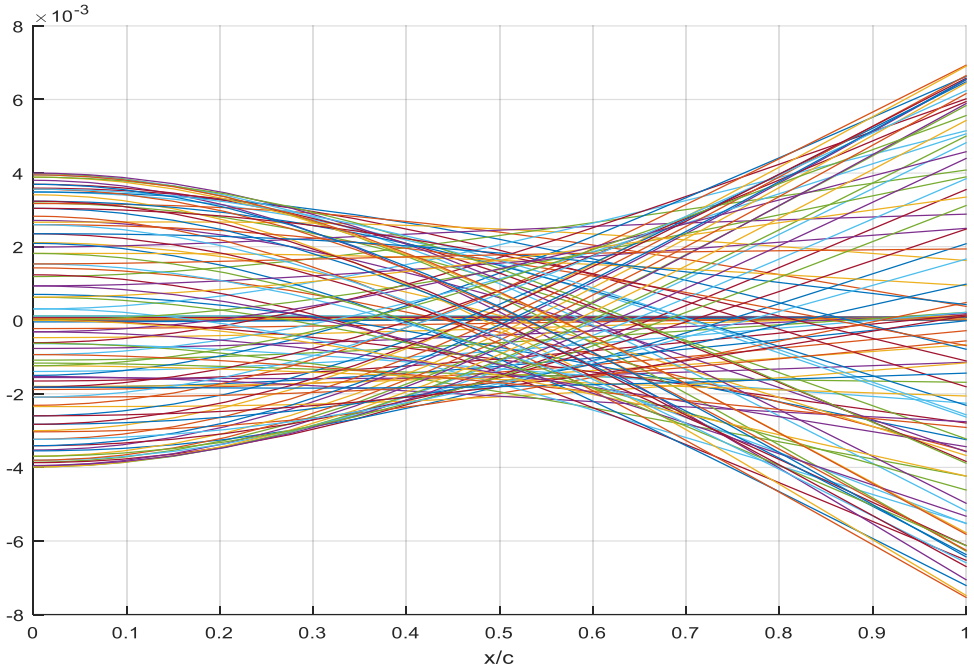

Figure 4.20 Deflection envelope during the last period of motion for $f / f_o = 1.5$

Chapter 5 - Concluding Remarks and Future Research

In this work we extended a previously developed 2-D panel method to treat the unsteady lifting flow problem of flapping foils with prescribed deformations. In this context **a non-linear pressure-type Kutta condition** is implemented along with **frozen wake modelling** for the trailing vortex sheet. The convergence and stability of the proposed numerical scheme are discussed, while numerical results concerning the overall propulsive performance of the system with prescribed deformations are presented in order to illustrate effects of chord-wise flexibility. Emphasis has also been given to the **calculation of chord-wise pressure distribution**.

A model for the dynamic structural analysis of the foil employing the Classical Plate Theory (CPT) based on the Kirchhoff-Love hypothesis has been proposed. As a structural member, the foil, is modelled as a thin plate **with a flexural rigidity variation** and subjected to **cylindrical bending** under the **plane strain** assumption. In this formulation, the 2-D elasticity problem reduces to an 1-D problem. A finite element method based on Hermite interpolation is presented for the numerical approximation of the plate response. The damped structural response of the foil is treated with the addition of **proportional damping terms.**

Finally, a coupled BEM-FEM numerical scheme for the treatment of the fluid-structure interaction problem of flapping foils with chord-wise flexibility and a flexural rigidity profile variation is presented. The proposed methodology is able to assess the overall performance of systems that operate as biomimetic inspired propulsion. Numerical results are compared against experimental data for the case of flexible flat plates, in enforced heaving motions, in order to validate the proposed numerical scheme.

Future work is planned towards the detailed investigation and systematic examination of the structural response of the chord-wise flexible foil over a range of design and operation parameters, including reduced frequency, heaving and pitching amplitudes and effective angle of attack, and various flexural rigidity profiles inspired by nature.

Direct extensions include the introduction and modelling of various nonlinearities associated with the evolution of the trailing vortex sheet as well as accounting for large deformation assumption in the structural response. In order to extent the methods applicability for **large angles of attack** we can introduce the treatment of leading edge separation and dynamic stall effects. Treatment of the 3-D deformable flapping wing, including also span-wise flexibility effects is also an interesting topic for future work.

Motivated by the work of Moored (2018), future work could also be planned towards the development of a combined unsteady 3D coupled BEM-FEM, a boundary layer solver and self-propeller equations of motion could be exploited to **explore bio-inspired self-propelled locomotion**, including flexibility effects.

Another direction for research includes the study of oscillating hydrofoils in the presence of waves and currents for the exploitation of combined renewable marine energy sources in nearshore and coastal regions. These systems operate as **semi-activated biomimetic energy device**, with imposed pitching motion and induced heaving motion in harmonic incident waves and currents. The use of aquatic inspired oscillating flexible fins in such applications confirm that such systems are able to achieve high levels of efficiency either for propulsion or for tidal energy extraction.

The implementation of high order BEM using b-splines of NURBS for the representation of the geometry and the unknown distribution of singularities on the boundary would accelerating the convergence and increase the numerical efficiency of the proposed scheme. Finally, the above problems increase significantly the computational requirements, especially when 3-D effects are included in the modelling. Parallel programming techniques and general purpose programming on graphics processing units (GPGPU) can alleviate this problem. The implementation of the computational code could be done using the CUDA C/C++ application programming interface (API).

Appendix

A. Preliminaries from Functional Analysis

Functional analysis provides some very intriguing tools to the study of partial differential equations. Instead of trying to solve a given strong formulation of a boundary value problem directly, the very structure of vector spaces can be used to yield the desirable solution. These solutions are naturally found in Sobolev spaces $W^{k,p}$ which are *normed vector spaces of functions.* Hilbert spaces, *complete* subsets of Sobolev spaces equipped with *inner product structures,* are also important in approximation theory (Brenner & Scott, 2008), (Kreyszig, 1978).

Abstractly we consider two real normed spaces U, V with *their continuous dual spaces* U^*, V^* respectively. Any vector space has a corresponding dual space consisting of all the linear functional on that space, together with structures of pointwise addition and scalar multiplication by constants. In this topological vector space, there is a subspace of the dual space that consists of continuous linear functional, called the continuous dual space.

If U is the space of the possible solutions; given some partial differential operator $\Lambda : U \to V^*$ and a specified element $f \in V^*$, the objective is to find a $u \in U$ such that

$$\Lambda u = f \tag{A.1}$$

However, in weak formulations, the above equation is only required to hold when *tested* against all other possible elements of V, which are called *test functions*.

Introducing a formal definition of the Sobolev and Hilbert spaces requires some preliminary notation. Starting with the Lebesque integral of a real-valued function f on a given domain Ω. For $1 \leq p < \infty$, let

$$\| f \|_{L^p(\Omega)} := \left(\int_{\Omega} | f(x) |^p dx \right)^{1/p} \tag{A.2}$$

and for $p = \infty$

$$\| f \|_{L^\infty(\Omega)} := ess\ \sup\{ | f(x) | \ : x \in \Omega \} \tag{A.3}$$

The Lebesgue spaces are then defined as $L^P(\Omega) := \{ f : \|f\|_{L^P(\Omega)} < \infty \}$ and are linear (or vector) spaces. Also, the functional $\|\cdot\|_{L^P(\Omega)}$ has norm properties.

Definition. *A normed linear space* $(V, \|\cdot\|)$ *is called a Banach space if it is complete with respect to the metric induced by the norm,* $\|\cdot\|$. *Therefore, for* $1 \le p < \infty$ *a Lebesgue space* $L^P(\Omega)$ *is a Banach space.*

Definition. *The support of a continuous function* u *defined on some domain in* $\mathbb{R}^n$ *is the closure of the (open) set* $\{x : u(x) \neq 0\}$. *If this is a compact set and it is a subset of the interior of a set,* Ω, *then* u *is said to have a compact support with respect to* Ω.

Definition. *Given a domain* Ω, *the set of locally integrable functions is denoted by* $L^1_{loc}(\Omega) := \{ f : f \in L^1(K) \quad \forall \text{ compact } K \subset \text{ interior } \Omega \}$

We proceed by introducing a definition of derivatives in a weak sense. For that we need to define an n-dimensional multi-index as a n-tuple $a = (a_1, a_2, ..., a_n)$ of non-negative integers. The length of which is $|a| := \sum_{i=1}^{n} a_i$. Then the point-wise partial derivative for $\varphi \in C^\infty$ is defined as $D_x^a \varphi = \left(\frac{\partial}{\partial x_1} \right)^{a_1} ... \left(\frac{\partial}{\partial x_n} \right)^{a_n} \varphi$.

Definition. *We say that a given function* $f \in L^1_{loc}$ *has a weak derivative* $D_\omega^a f$, *provided there exists a function* $g \in L^1_{loc}$ *such that for every function* φ *with a compact support in* Ω

$$\int_\Omega g(x)\varphi(x)dx = (-1)^{|a|} \int_\Omega f(x)\varphi^{(\alpha)}(x)dx \qquad \forall \varphi \in D(\Omega)$$

If such a g exists, we define $D_\omega^a f = g$.

Definition. *Let k be a non-negative integer, and let* $f \in L^1_{loc}$. *Suppose that the weak derivatives* $D_w^a f$ *exist for all* $|a| \le k$. *The Sobolev norm is defined*

$$\text{For } 1 \le p < \infty: \qquad \|f\|_{W_p^k(\Omega)} := \left(\sum_{|a| \le k} \|D_w^a f\|_{L^P(\Omega)}^p \right)^{1/p} \tag{A.4}$$

$$\text{For } p = \infty: \qquad \|f\|_{W_\infty^k(\Omega)} := \max_{|a| \le k} \|D_w^a f\|_{L^\infty(\Omega)}^p \tag{A.5}$$

Finally Sobolev spaces are defined as $W_p^k(\Omega) := \{ f \in L^1_{loc} : \quad \|f\|_{W_p^k(\Omega)} < \infty \}$. In this form index *k* refers to the vector space dimension, whereas index *p* is the order of the Lebesgue norm. Hilbert spaces are *complete inner product* vector spaces and their theory

is richer than that of the general normed and Banach spaces. Ofter these inner-product spaces are denoted by $H^k(\Omega)$.

B. Hermite shape functions

Let us assume that we have N+1 sample data points of a function f. In this section we will develop an interpolating polynomial that equals the function and its 1rst derivative at the given sample points. Therefore we require that for $i = 0,\ldots N$

$$g(x_i) = f(x_i) \tag{B.1}$$
$$g'(x_i) = f'(x_i) \tag{B.2}$$

Each of the expressions above enforces $(N+1)$ constrains and in total we have $2(N+1)$ constrains. We need to set up a general polynomial, of degree $2(N+1)-1$ so that the number of unknowns is equal to the number of constraints.

Hermite interpolation function of 3rd order

Consider the interval $[0,1]$ and that the values of function f and its 1st derivative are known at the exterior nodal points, i.e. $f(0) = f_o$, $f(1) = f_1$, $f'(0) = f_0^{(1)}$ and $f'(1) = f_1^{(1)}$. Since $N = 1$ the interpolating polynomial will be of $2(N+1)-1 = 3^{rd}$ degree. So,

$$g(x) = a_o + a_1 x + a_2 x^2 + a_3 x^3 \tag{B.3}$$

$$g'(x) = a_1 + 2a_2 x + 3a_3 x^2 \tag{B.4}$$

$$\begin{cases} g(0) = f_0 \\ g(1) = f_1 \\ g'(0) = f_0^{(1)} \\ g'(1) = f_1^{(1)} \end{cases} \Rightarrow \begin{cases} a_o = f_0 \\ a_o + a_1 + a_2 + a_3 = f_1 \\ a_1 = f_0^{(1)} \\ a_1 + 2a_2 + 3a_3 = f_1^{(1)} \end{cases} \tag{B.5}$$

If we apply constrains from eq. (B.1)-(B.2) to the expressions in (B.3) and (B.4) we have:

The constraint equations can be written in matrix form:

$$\begin{bmatrix} 1 & 0 & 0 & 0 \\ 1 & 1 & 1 & 1 \\ 0 & 1 & 0 & 0 \\ 0 & 1 & 2 & 2 \end{bmatrix} \cdot \begin{bmatrix} a_o \\ a_1 \\ a_2 \\ a_3 \end{bmatrix} = \begin{bmatrix} f_0 \\ f_1 \\ f_0^{(1)} \\ f_1^{(1)} \end{bmatrix} \tag{B.6}$$

Therefore,

$$g(x) = f_o + f_0^{(1)}x + (3f_1 - 3f_o - f_1^{(1)} - 2f_0)x^2 + (-2f_1 + 2f_o + f_0^{(1)} + f_1^{(1)})x^3 \tag{B.7}$$

If we re-write eq. (B.7) so that the functional and derivative values are factored out,

$$g(x) = f_o(2x^3 - 3x^2 + 1) + f_1(-2x^3 + 3x^2) + f_0^{(1)}(x^3 - 2x^2 + x) + f_1^{(1)}(x^3 - x^2) \tag{B.8}$$

In this formulation we have derived the basis of the cubic Hermite function space:

$$\begin{aligned} H_1 &= a_0(x) = 2x^3 - 3x^2 + 1 \\ H_2 &= b_0(x) = x^3 - 2x^2 + x \\ H_3 &= a_1(x) = -2x^3 + 3x^2 \\ H_4 &= b_1(x) = x^3 - x^2 \end{aligned} \tag{B.9}$$

Therefore we can define two separate functions associated with each data point. Mathematically the constraints discussed above, which are 16 in total *{2 nodes x 2 functions per node x 4 dofs per function}* can be expressed by

$$a_i(x_j) = \delta_{ij},\ b_i(x_j) = 0 \ \text{ for } i, j = 0,1 \tag{B.10a}$$

and their 1st derivative,

$$a_i^{(1)}(x_j) = 0,\ b_i^{(1)}(x_j) = \delta_{ij} \ \text{ for } i, j = 0,1 \tag{B.10b}$$

with $\delta_{ij} = \begin{cases} 0 & \text{i} \neq \text{j} \\ 1 & \text{i} = \text{j} \end{cases}$ denoting the Kronecker delta.

<u>Hermite interpolation function of 5th order</u>

If we assume that for the same interval $[0,1]$ we are given the data at three nodal points for the function and its 1st derivative, for the two exterior nodes and the mid-point as the interior node. Since $N = 2$ the interpolating polynomial will be of $2(N+1)-1 = 5^{th}$ degree. So,

$$g(x) = a_o + a_1 x + a_2 x^2 + a_3 x^3 + a_4 x^4 + a_5 x^5 \quad \text{(B.11)}$$

$$g'(x) = a_1 + 2a_2 x + 3a_3 x^2 + 4a_4 x^3 + 5a_5 x^4 \quad \text{(B.12)}$$

After the constrains are applied to the interpolating polynomial expression and the equations are written in matrix notation, the system of linear equations can be solved with respect to the nodal unknowns. The next step is to substitute the solution to equations (B.11) and rearrange the terms so that the functional and derivative values are factored out. The basis functions of 5th order polynomials are given by the following analytic formulas:

$$\begin{aligned} H_1 &= a_0(x) = 24x^5 - 68x^4 + 66x^3 - 23x^2 + 1 \\ H_2 &= b_0(x) = 4x^5 - 12x^4 + 13x^3 - 6x^2 + x \\ H_3 &= a_{0.5}(x) = 16x^2(1-x)^2 \\ H_4 &= b_{0.5}(x) = 8x^2(2x^3 - 5x^2 + 4x - 1) \\ H_5 &= a_1(x) = x^2(-24x^3 + 52x^2 - 34x + 7) \\ H_6 &= b_1(x) = x^2(4x^3 - 8x^2 + 5x - 1) \end{aligned} \quad \text{(B.13)}$$

The shape functions also have the following characteristics:

$$a_i(x_j) = \delta_{ij},\ b_i(x_j) = 0 \ \text{ for } \ i, j = 0, 0.5, 1 \quad \text{(B.14a)}$$

and their 1st derivative,

$$a_i^{(1)}(x_j) = 0,\ b_i^{(1)}(x_j) = \delta_{ij} \ \text{ for } \ i, j = 0, 0.5, 1 \quad \text{(B.15b)}$$

with δ_{ij} as the Kronecker delta.

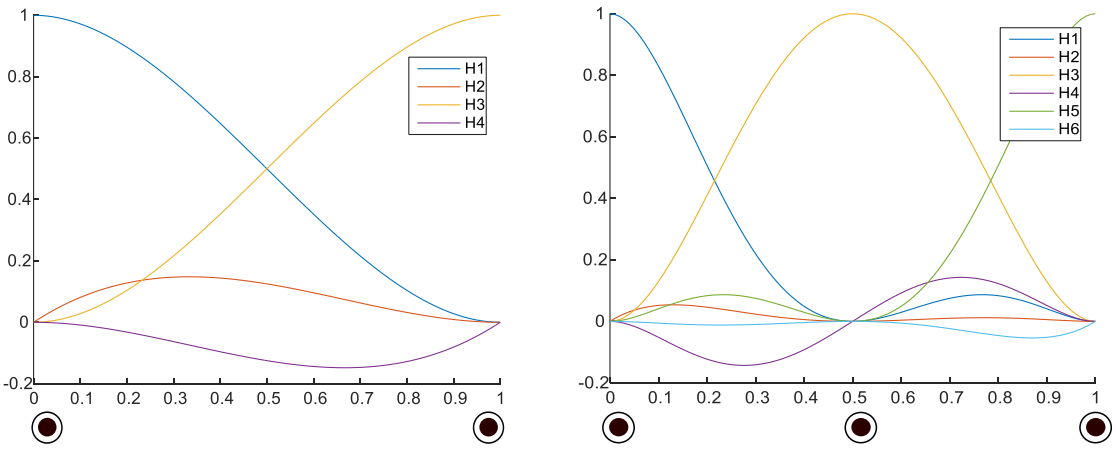

Figure B.1 Shape Functions for Hermite Finite Elements of 3rd degree (left) and 5th degree (right) polynomials.

C. Gaussian Quadrature

A quadrature rule is an approximation of the definite integral of a function, usually stated as a weighted sum of function values at specified points within the domain of integration. The $n-$point Gaussian quadrature rule, is constructed to yield an exact result for polynomials of degree $2n-1$ or less by a suitable choice of the nodes x_i and weights w_i, $i=1,...n$. The most common domain of integration for such a rule is taken as $[-1,1]$. In that interval the Gauss-Legendre quadrature rule is,

$$\int_{-1}^{1} f(x)dx \approx \sum_{i}^{n} w_i f(x_i). \tag{C.1}$$

However, this quadrature rule will only be an accurate approximation to the integral above if $f(x)$ is well-approximated by a polynomial of degree $2n-1$ or less on $[-1,1]$ in the first place. The abscissas for quadrature order n are given by the roots x_i of the Legendre polynomials $P_n(x)$, which occur symmetrically about 0. The weights are given by the following expression

$$w_i = -\frac{2}{(1-x_i^2)[P_n^{'}(x_i)]^2} \tag{C.2}$$

where $P_n^{'}(x_i)$ is the derivative of the Legendre polynomial.

An integral over $[a,b]$ must be changed into an integral over $[-1,1]$ before applying the Gaussian quadrature rule. This change of interval can be done in the following way:

$$\int_{a}^{b} f(x)dx \approx \frac{b-a}{2}\sum_{i}^{n} w_i f(\frac{b-a}{2}x_i + \frac{a+b}{2}). \tag{C.3}$$

References

Adhikari, S. (2000). *Damping Models for Structural Vibration.* Trinity College, Cambridge: Cambridge University Engineering Department.

Alben, S. (2008). Optimal flexibility of a flapping appendage in an inviscid fluid. *Journal of Fluid Mechanics*, vol 614, 355-380.

Alben, S., Witt, C., Baker, T. V., Anderson, E., & Lauder, G. V. (2012). Dynamics of freely swimming flexible foils. *Physics of Fluids*.

Babuska, I., Szano, B. A., & Katz, I. N. (1981). The p-Version of The Finite Element Analysis. *SIAM Journal on Numerical Analysis, Vol. 18, No. 3* , 515-545.

Baranyyk, O., Buckham, B. J., & Oskai, P. (2010). On the performance of oscillating plate underwater propulsion system with variable chordwise flexibility at differenet depths of submergence. *Journal of Fluids and Structures*.

Basu, B. C., & Hancock, G. J. (1977). *The unsteady motion of a two-dimensional aerofoil in incopressible inviscid flow.*

Belibassakis, K. A., & Filippas, E. S. (2016). Biomimetic marine energy devices in waves and sheared currents. *2nd International Conference on Renewable Energies Offshore (RENEW2016)*, (pp. 179-187). Lisbon, Portugal.

Belibassakis, K. A., & Politis, G. A. (2013). Hydrodynamic performance of flapping wings for augmenting ship propulsion in waves. *Ocean Engineering 72*, 227-240.

Beltempo, A., Balduzzi, G., Alfano, G., & Auricchio, F. (2015). Analytical derivation of a general 2D non-prismatic beam model based on the Hellinger-Reissner principle. *Engineering Structures, 101*, 88-98.

Bourlet, T. F., Gurugubelli, P. S., & Jaiman, R. K. (2015). The boundary layer develpment and travelling wave mechanisms during flapping of a flexible foil. *Journal of Fluids and Structures 54*, 784-801.

Brebbia, C., Telles, J., & Wrobel, L. (1984). *Boundary Element Techniques.* Springer-Verlag.

Brenner, S. C., & Scott, L. R. (2008). *The Mathematical Theory of Finite Element Methods.* Springer.

Cheng, J. Y., Pedley, T., & Altringham, J. (1998). A continuous dynamic beam model for swimming fish. *The Royal Society*.

Chowdhury, I., & Dasgupta, S. (2003). Computation of Rayleigh Damping Coefficients for Large Systems. *Electronic Journal of Geotechnical Engineering* .

Ciarlet, P. G. (1978). *The Finite Element Method for Elliptic Problem.* North-Holland, Amsterdam, New York: Oxford.

Cleaver, D. J., Gursul, I., Calderon, D. E., & Wang, Z. (2014). Thrust enhancement due to flexible trailing-edge of plunging foils. *Journal of Fluids and Structures*.

Dai, H., Luo, H., & Doyle, J. F. (2012). Dynamic pitching of an elastic rectangular wing in hovering motion. *Journal of Fluid Mechanics*.

Dai, H., Luo, H., Sousa, P. J., & Doyle, J. F. (2012). Thrust performance of a flexible low-aspect-ratio pitching plate. *Physics of Fluids*.

Daniel, T. L., & Combes, S. A. (2002). Flexible Wings and Fins: Bending by Inertial or Fluid-Dynamic Forces. *Integrative and Comparative Biology*.

Dewey, P. A., Boschitsch, B. M., Moored, K. W., Stone, H. A., & Smits, A. J. (2013). Scaling laws for the thrust production of flexible pitching panels. *Journal of Fluid Mechanics*.

Fernandez-Praz, R. (2017). Effect of chordwise flexibility on pitching foil propulsion in a uniform current. *Ocean Engineering 145*, 24-33.

Filippas, E. S. (2019). *PhD - Hydrodynamics analysis of ship and marine biomimetic systems in waves using GPGPU programming.* Athens, Greece: National Technical University of Athens, School of Naval Architecture and Marine Engineering.

Filippas, E. S., & Belibassakis, K. A. (2014). Hydrodynamic analysis of flapping-foil thrusters operating beneath the free surface and in waves. *Engineering Analysis with Boundary Elements 41*, 47-59.

Filippas, E. S., Gerostathis, T. P., & Belibassakis, K. A. (2018). Semi-activated oscillating hydrofoil as a nearshore biomimetic energy system in waves and currents. *Ocean Engineering 154*, 396-415.

Filippas, E., & Belibassakis, K. (2014). Hydrodynamic analysis of flapping-foil thrusters operating beneath the free surface and in waves. *Engineering Analysis with Boundary Elements*, 47-59.

Filippas, E., & Belibassakis, K. (2014). Hydrodynamic analysis of flapping-foil thrusters operating beneath the free surface and in waves. *Engineering Analysis with Boundary Elements*, 47-59.

Fillipas, E. (2013). *A boundary element method for the hydrodynamic analysis of flapping-foil thrusters operating beneath the free surface and in waves.* NTUA: Diploma Thesis.

Fung, Y. C., & Tong, P. (2001). *Classical and Computational Solid Mechanics.* Singapore: World Scientific.

Gelfand, I. M., & Fomin, S. V. (1963). *Calculus of Variations.* Englewood Cliffs, New Jersey: Prentice-Hall, Inc. .

Gunter, N. M. (1967). *Potential Theory and Its Applications to Basic Problems of Mathematical Physics.* New York: Frederic Ungar Publishing CO.

Heathcote, S., & Gursul, I. (2007). Flexible Flapping Airfoil Propulsion at Low Raynolds Numbers. *AIAA*.

Heathcote, S., Matrix, D., & Gursul, I. (2004). Flexible Flapping Airfoil Propulsion at Zero FreeStream Velocity . *AIAA*.

Heathcote, S., Wang, Z., & Gursul, I. (2008). Effect of spanwise flexibility on flapping wing propulsion. *Journal of Fluids and Structures*.

Hess, J., & Smith, A. (1964). Calculation of non-lifting potential flow about arbitrary 3-D bodies. *Journal of Ship Research*.

Hess, J., & Valarezo, W. (1985). Calculation of steady flow about propellers by means of a surface panel method. *23rd Aerospace Sciences Meeting.*

Hill, S. J. (1998). *Large Amplitude Fish Swimming.* The University of Leeds: PhD Thesis.

Hughes, T. J. (1987). *The Finite Element Method: Linear Static and Dynamic Finite Element Analysis.* Prentice-Hall Inc.

J.L, H., & Friedman. (1981). *An imporved higher-order panel method for 3-dimensional lifting potential flow.* Naval Air Development Center.

Jeanmond, G., & Olivier, M. (2017). Effects of chordwise flexibility on 2D flapping foils used as energy extraction devices. *Journal of Fluids and Structues 70*, 327-345.

Joseph Katz, A. P. (2001). *Low-Speed Aerodynamics.* Cambridge University Press.

Kancharala, A. K., & Philen, M. K. (2016). Optimal chordwise stiffness profiles of self-propelled flapping fins. *Bioinspiration and Biomimetics*.

Katz, J., & Plotkin, A. (1991). *Low-speed Aerodynamics - From wing theory to panel methods.* Singapore: Mc Graw Hill International Editors.

Katz, J., & Weihs, D. (1978). Hydrodynamic propulsion by large amplitude oscillation of airfoil with chordwise flexibility . *Journal of Fluid Mechanics*, vol. 88, part 3, 485-497.

Katz, J., & Weihs, D. (1979). Large amplitude unsteady motion of a flexible slender propulsor. *Journal of Fluid Mechanics*, vol 90, part 4, 713-723.

Kress, R. (1989). *Linear Integral Equations.* Springer.

Kreyszig, E. (1978). *Introductory Functional Analysis and Applications.* John Wiley & Sons. Inc.

Lauder, G. V., & Madden, P. G. (2007). Fish Locomotor: kinematics adn hydrodynamics of flexible foil-like fins. *Experimental Fluids*.

Lauder, G. V., Madden, P. G., Mittal, R., Dong, H., & Bozkurttas, M. (2006). Locomotion with flexible propulsors: I. Experimental analysis of pestoral fin swimming in sunfish. *Institute of Physics Publishing*.

Lighthill, M. J. (1969). Hydromechanics of aquatic propulsion. *Annual Review Of Fluid Mechanics*.

Lighthill, M. J. (1971). Large-Amplitude Elongated-Body Theory of Fish Locomotion. *Proceedings of Royal Society*.

Longuet-Higgins, M. S., & Cokelet, E. (1975). *The deformation of steep surface waves on water I. A numerical method of computation.* Proceedings of the Royal Society.

Luo, H., Yin, B., Dai, H., & Doyle, J. F. (2010). A 3D computational study of the flow-structure interaction flapping flight. *48th AIAA Aerospace Sciences Meeting Including the New Horizons Forum and Aerospace Exposition*.

Mabie, H. H., & Rogers, C. B. (1974). Transverse vibrations of double-tapered cantilever beams with end support and with end mass. *The Journal of the Acoustical Society of America, 55*, 986-991.

Mantia, M. L., & Dabnichki, P. (2009). Unsteady panel method for flapping foil. *Engineering Analysis with Boundary Elements vol. 33, no. 4*, pp. 572-580.

Mantia, M. L., & Dabnichki, P. (2011). Influence of the wake model on the thrust of oscillating foil. *Engineering Analysis with Boundary Elements vol. 35, no. 3*, 404-414.

Mantia, M. L., & Dabnichki, P. (2013). Structural response of oscillating foil in water. *Engineering Analysis with Boundary Elements, vol. 37, no. 6* , 957-966.

Mantia, M., & Dabnichki, P. (2008). Unsteady panel method for flapping foil. *Engineering Analysis and Boundary Elements*.

Mantia, M., & Dabnichki, P. (2011). Influence of the wake model on the thrust of oscillating foil. *Engineering Analysis and Boundary Elements*.

Miao, J. M., & Ho, M. H. (2005). Effect of flexure on aerodynamic propulsive efficiency of flapping flexible airfoil. *Journal of Fluids and Structures*.

Michelin, S., & Smith, S. G. (2009). Resonance and propulsion performance of a heaving flexible wing. *Physics of Fluids*.

Mikhlin, S. (1965). *Multidimentional singular integrals and integral equations.* Pergamon Press.

Mittal, R., Dong, H., Bozkurttas, M., Lauder, G. V., & Madden, P. (2006). Locomotion with flexible propulsors: II. Computational modeling of pectoral fin swimming in sunfish. *Bioinspiration and Biomimetics*.

Moored, K. W. (2018). Unsteady three-dimensional boundary element method for self-propelled bio-inspired locomotion. *Computers & Fluids*, 324-340.

Moran, J. (1984). *An Introduction to Theoretical ans Computational Aerodynamics.* John Wiley and Sons Inc.

Paraz, F., Eloy, C., & Schouveiler, L. (2014). Experimental study of the response of a flexible plate to a harmonic forcing in a flow. *Comptes Rendus Mecanique*, 342, 532-538.

Paraz, F., Schouveiler, L., & Eloy, C. (2016, January). Thrust generation by a heaving flexible foil: Resonance, nonlinearities and optimality. *Physics of Fluids*.

Paul Riggs, A. B. (2010). Advantages of a Biomimetic Stiffness Profile in Pitching Flexible Fin Propulsion. *Journal of Bionic Engineering 7*, 113-119.

Pederzani, J., & Haj-Hariri, H. (2006). A numerical methods for the analysis of flexible bodies in unsteady viscous flows. *International Journal for Numerical Methods in Engineering*.

Pedley, T. J., & Hill, S. J. (1999). Large amplitude undulatory fish swimming: fluid mechanics coupled to internal mechanics. *The Journal of Experimental Biology*.

Poling, D. R., & Telionis, D. P. (1986). *The Response of Airfoils to periodic Disturbances - The Unsteady Kutta Condition.*

Politis, G. (2011). *The boundary element method for 3-D fluid flow problems, Notes on the lecture: ''Mathematical formulation of lifting flows"*. School of Naval Architecture and Marine Engineering,NTUA.

Politis, G., & Politis, K. (2014). Biomimetic propulsion under random heaving conditions, using active pitch control. *Journal of Fluids and Structures 47*, 139-149.

Politis, G., & Tsarsitalides, V. (2012). Flexible Oscillating Duct: An approach to a novel propulsor. *Applied Ocean Research 36*, 36-50.

Prats, R. F. (2015). *Hydrodynamics of pitching foils: flexibility and ground effects.* PhD Thesis.

Praz, R. F. (2015). Effect of chordwise flexibility on pitching foil propulsion in a uniform current. *Ocean Engineering*.

Prempraneerach, P., Hover, F. S., & Triantafyllou, M. S. (2003). The effect of chordwise flexibility on the thrust and efficiency of a flapping foil. *Proc. 13th Int. Symp. on Unmanned Untethered Submersible Technology: special session on bioengineering research related to autonomous underwater vehicles, New Hampshire*, Vol 152, 152-170.

Priovolos, A. K., Filippas, E. S., & Belibassakis, K. A. (2018). A vortex-based method for improved flexible flapping-foil thruster performance. *Engineering Analysis with Boundary Elements 95*, 69-84.

Quinn, D. B., Lauder, G. V., & Smits, A. J. (2014). Scaling the propulsive performance of heaving flexible panels. *Journal of Fluid Mechanics*.

Quinn, D. B., Lauder, G. V., & Smits, A. J. (2015). Maximizing the efficiency of flexible propulsor using experimental optimization. *Journal of Fluid Mechanics*.

Rahul Bale, M. H. (2014). Gray's paradox: A fluid mechanical perspective. *Scientific Reports*.

Ramamurti, R., Sandberg, W. C., Löhner, R., Walker, J. A., & Westneat, M. W. (2002). Fluid dynamics of flapping aquatic flight in the bird wrasse: three-dimensional unsteady computation with fin deformation. *The Journal of Experimental Biology*.

Reddy, J. N. (2007). *Theory and Analysis of Elastic Plates and Shells.* CRC Press .

Richards, A. J., & Oskai, P. (2015). Effects of the stiffness, inertia and oscillation kinematics on the thrist generation and efficiency of an oscillating-foil propulsion system. *Journal of Fluids and Structures*.

Riggs, P., Bowyer, A., & Vincent, J. (2010). Advantages of a Biomimetic Stiffness Profile in Pitching Flexible Fin Propulsion. *Journal of Bionic Engineering 7*, 113-119.

Rozhdestvensky, K. V., & Ryzhov, V. A. (2003). Aerodynamics of flapping-wing propulsors. *Progress in Aerospace Sciences*.

Salazar, R., Fuentes, V., & Abdelkefi, A. (2018). Classification of biological and bioinspired aquatic systems: A review. *Ocean Engineering* , 75-114.

Schouveiler, L., Hover, F. S., & Triantafyllou, M. S. (2005). Performance of flapping foil propulsion. *Journal of Fluids and Structures 20*, 949-959.

Sfakiotakis, M., Lane, D. M., & Davis, J. B. (1999). Review of Fish Swimming Modes for Aquatic Locomotion. *IEEE Journal of Oceanic Engineering*.

Shyy, W., Aono, H., Chimakurthi, S. K., Trizila, P., Kang, C. K., Cesnik, C. E., & Liu, H. (2010). Recent progress in flapping wing aerodynamics and aeroelasticity. *Progress in Aerospace Sciences*.

Shyy, W., Aono, H., Kang, C.-K., & Liu, H. (2013). *An introduction to Flapping Wing Aerodynamics.* Cambridge University Press.

Sousa, P. J., & Allen, J. J. (2011). Thrust efficiency of harmonically oscillating flexible flat plates. *Journal of Fluid Mechanics*.

Stoer, J., & Burlish, R. (1991). *Introduction to Numerical Analysis.* Springer-Verlag.

Taylor, G. K., Nudds, R. L., & Thomas, A. L. (2003). *Flying and swimming animals cruise at a Strouhal number tuned for high power efficiency.* Nature.

Triantafyllou, G. S., Triantafyllou, M. S., & Grosenaugh, M. A. (1993). Optimal thrust developoment in oscillating foils with application to fish propulsion. *Journal of Fluids and Structures*.

Triantafyllou, M. S., Triantafyllou, G. S., & Yue, D. K. (2000). Hydrodynamics of fishlike swimming. *Annu. Rev. Fluid. Mech*, 32:33-53.

Warburton, G. B. (1976). *The Dynamic Behaviour of Structures.* p. 131: Pergamon Press.

Wei Shyy, H. A.-K. (2013). *An Introduction to Flapping Wing Aerodynamics.* Cambridge University Press.

Wu, T. Y.-T. (1970). Hydromecanics of swimming propulsion. Swimming and optimum movements of slender fish with side fins. *Journal of Fluid Mechanics*.

Xiao, Q., & Zhu, Q. (2014). A review on flow energy harvesters on flapping foils. *Journal of Fluids and Structures 46*, 174-191.

Yamamoto, I., Terada, Y., Nagamatu, T., & Imaizumi, Y. (1995). Propulsion System with Flexible/Rigid Oscillating Fin. *Journal of Ocean Engineering*.

Yu, Z., & Eloy, C. (2017). Extension of Lighthill's slender body theory to moderate aspect ratios. *Journal of Fluid and Structures*.

Zaglmayr, Z. (2006). *High Order Finite Element Methods for Electromagnetic Field Computation .* PhD - Johannes Kepler Universitat.

Zhu, Q. (2007). Numerical Simulation of a Flapping Foil with Chordwise or Spanwise Flexibility. *AIAA*.

Zhu, Q., & Shoele, K. (2008). Propulsion performance of a skeleton-strengthened fin . *The Journal of Experimental Biology*.

Zienkiewicz, O. C., Taylor, R. L., & Zhu, J. L. (2005). *The Finite Element Method: Its Basis and Fundamentals 6th Edition.* McGraw-Hill.